University of Alberta

**Rheological Behavior and Nano-Microstructure of Complex Fluids:
Biomedical and Bitumen-Heavy Oil Applications**

by

MD Anwarul Hasan

A thesis submitted to the Faculty of Graduate Studies and Research
in partial fulfillment of the requirements for the degree of

Doctor of Philosophy

in

Thermofluids

Department of Mechanical Engineering

©MD Anwarul Hasan

Fall 2010

Edmonton, Alberta

Examining Committee

Supervisor: Lange, Carlos F, Mechanical Engineering

Co-Supervisor: Shaw, John M, Chemical Engineering

Committee member: King, Malcolm, Medicine

External: Gehr, Peter, Histology

Committee member: Vehring, Reinhard, Mechanical Engineering

Chair: Flynn, Morris, Mechanical Engineering

Acknowledgement

Nikooyeh, Nima Saber, and others whose cooperation and friendship was an asset for the author during this research.

No words could describe the author's debt to his parents, Syed Shakil Ahmed and Syeda Raqiba Khatoon; his wife Shajia Hasan, maternal uncles Syed Iqbal Ahmed, Syed Khushnud Alam and Dr Syed Irshad Ahmad al-Bukhari, and all family for their trust and sacrifices, and for giving the author the opportunity to pursue higher education. None of this work would be possible without their encouragement and moral support.

Abstract

The main objective of this research was to exploit the interrelations between the rheological behavior and nano-microstructure of complex fluids in solving two state-of-the-art problems, one in the field of biomedical engineering: controlling the amount and characteristics of bioaerosol droplets generated during coughing, and the other in the bitumen-heavy oil industry: characterizing the nano-microstructure of asphaltene particles in bitumen and heavy oil from their rheological behavior.

For the first problem, effect of viscoelastic and surface properties of artificial mucus simulant gels on the size distribution and amount of airborne bioaerosol droplets generated during simulated coughing were investigated. The results revealed that suppressing the generation of bioaerosol droplets and/or reducing the number of emitted droplets to a minimum during coughing are practically achievable through modulation of mucus viscoelastic properties. While variation of surface tension did not show any change in the droplet size distribution, an increase in particle size was observed as the samples changed from elastic solid type to viscoelastic type to viscous fluid type samples. This knowledge will help in the development of a new class of drugs being developed at the University of Alberta, aimed at controlling the transmission of airborne epidemic diseases by modifying the viscoelastic properties of mucus.

For the second problem, studies of viscoelastic behavior of Athabasca bitumen (Alberta) and Maya crude (Mexico) oil samples, along with their Nano-filtered and chemically separated-plus-reconstituted samples were performed. The results revealed that the rheological behaviors of the bitumen-heavy oil samples are

governed by their multiphase nature. The rheological behavior of all feeds, permeates and retentate samples followed a single master curve over the entire temperature interval, consistent with that of a slurry comprising a Newtonian liquid plus a dispersed solid comprising non-interacting hard spheres. The behavior of asphaltenes in the reconstituted samples, however, was found to be significantly different from that in nanofiltered samples.

The information about the characteristics and behaviors of asphaltenes obtained in this study will help better understand the asphaltene structures, and support the effort to determine solutions for numerous asphaltene-related industrial problems. In the long run, this knowledge will help to create more efficient extraction and upgrading processes for bitumen and heavy oils.

Nomenclature

A	Pre-exponential factor in Arrhenius Equation
E	Activation energy of viscous flow for solid-free maltene
K	Crowding factor
R	Universal gas constant
T	Absolute temperature
σ	Particle interaction coefficient
σ_o	Amplitude of oscillatory stress signal
φ	Volume fraction of solid particles
φ_{max}	Maximum volume fraction
ω	Frequency of oscillation
τ	Shear stress
τ_y	Yield stress
γ_o	Amplitude of strain signal
γ	Strain
$\dot{\gamma}$	Shear rate
μ	Newtonian viscosity
F	Shear force
du	Velocity of upper plate in a parallel shear flow
dy	Separation gap between parallel plates
G	Rigidity modulus
G^*	Complex modulus

G'	Storage modulus
G''	Loss (viscous) modulus
η	Viscosity of dispersion
η^*	Complex viscosity
η'	Dynamic viscosity
η''	Imaginary part of viscosity
η_o	Zero shear viscosity
η_∞	Viscosity at infinite (very high) shear rate
η_r	Relative viscosity
$[\eta]$	Intrinsic viscosity
δ	Phase angle
K_s	Solvation constant

List of Tables

List of Figures

Fig. 6.4. Evidence of a slow or irreversible phase transition in Athabasca asphalthenes from high-temperature viscosity measurements (3 K min^{-1}, 500 μm gap, $\omega = 6.3$ s^{-1}, 5 Pa stress), successive experiments

Fig. 6.5. Time dependence of viscosity for Maya crude oil upon equilibration after reaching a stable temperature $T = 260.65$ K (double gap cylinder – Peltier assembly, $\omega = 0.63$ s^{-1}, 0.1% strain)

Fig. 6.6. Time dependence of viscosity for Maya crude oil at (a) $T = 273.15$ K and $\omega = 6.3$ s^{-1} ; (b) $T = 258.15$ K and $\omega = 0.63$ s^{-1} (double gap cylinder – Peltier assembly)

Fig. 6.7. Frequency and temperature dependence of complex viscosity (a) and phase angle (b) for Maya crude oil (strain – see text, DGC-PA is the double gap cylinder – Peltier assembly, PP-ETC is the parallel plates – extended temperature cell)

Fig. 6.8. Viscosity variation for Athabasca bitumen with temperature: solid lines, PPV, $\omega = 0.63$, 6.3, 63 and 630 s^{-1} (this work)

Fig. 6.9. Temperature dependence of viscosity for Athabasca bitumen from different locations and elevations determined by Ward and Clark[5] (measurement method – capillary viscometry; recovery method – benzene-based extraction standardized for all samples.

Fig. 7.1. Total solid (wt.%) for Athabasca bitumen and Maya crude oil.

Table of Contents

Part 2: Application 1: Bioaerosol Droplets Generation and Control

Chapter 3: Introduction

Chapter 4: Mitigation of Exhaled Bioaerosols by Modulating the Rheological and Surface Properties of Mucus

Part 3: Application 2: Structure of Asphaltene Nanoaggregates in Bitumen and Heavy oil

Chapter 5: Introduction

Chapter 8: Pentane-Asphaltene rheological behavior in reconstituted crude oils

Chapter 9: Conclusions and Recommendations

<u>Appendices:</u>

Part 1: Introduction, Background and Theory

Chapter 1: Introduction

1.1. Introduction

Rheological properties, such as complex viscosity, elastic and viscous modulus etc. play a vital role in numerous industrial products and applications from cosmetics to ceramics to pharmaceuticals and food concentrates [1]. The list continues with biological fluids such as blood, serum, and respiratory airway mucus; industrial fluids such as paints, composites, glass and polymer melts; and petrochemical fluids such as bitumen, crude oil and heavy oils.

For all complex fluids, the rheological behavior/properties are dependent on their nano-microstructure and vice versa. Therefore the rheological properties have been widely used as tools for characterizing and controlling the nano-microstructure of intermediate and final products in polymers, paints, pharmaceuticals and many other industries [2]. In biomedical and bitumen-heavy oil fields the application of rheological properties (i.e. the viscoelastic behavior) as a characterizing tool for the nano-microstructure of fluids or as a tool for controlling the nano-microstructure of fluids has been very limited. The potentials for them to be used in these two fields as characterizing tools or controlling tools for the intermediate or end products, however, are tremendously high. Here are two examples:

(i) Bioaerosol droplets exhaled by humans during breathing, sneezing and coughing are known to carry airborne pathogens, which, upon inhalation by others, can spread certain contagious infectious diseases, such as influenza, measles, swine flue, chickenpox, smallpox, SARS and so on. Recent theoretical studies [3] indicate that the number and size distribution of the bioaerosol droplets generated during coughing can be controlled by altering the rheological properties of the airway surface liquid. On the other hand, the rheological properties of airway surface liquid depend on the structures and interactions at the molecular level. However, experimental data on the rheological properties of airway mucus or on the dependence of number and size distribution of bioaerosol droplets generated during coughing sneezing etc. are absent in the literature. Proper understanding of dependence of rheological properties on molecular structure and of the interrelations between the viscoelastic properties of tracheo-bronchial mucus and the number and size distribution of bioaerosol droplets generated during coughing/sneezing etc can provide us the ability of mitigating the bioaerosol droplets generation when desirable, and/or of controlling the size distribution of the droplets generated during coughing.

(ii) It is well known that the characteristics of nano and micron-size dispersed particles (from their structure, size, and shape to their tendency to flocculate, deaggregate, and sediment) play a significant role in determining the thermo physical behavior of complex non-Newtonian fluids. The structure of such solid (i.e.. asphaltenes) particles, dispersed in crude oils and bitumen, are surprisingly difficult to measure reliably and reproducibly. Various experiments using

2

methods, such as calorimetry [4], SAXS (small angle x-ray scattering) [5], SANS (small angle neutron scattering) [6, 7], NMR (nuclear magnetic resonance) [8], HPLC-UV (high performance liquid chromatography with ultraviolet spectroscopy), and numerical simulation methods, such as Statistical Mechanics simulation [9], Monte Carlo simulation, and molecular dynamics simulation [10, 11], have been used to determine the structure of asphaltene particles, but the asphaltene structures are still not completely understood.

Proper understanding of asphaltene structures can help bitumen-heavy oil industries in two ways. First, the tendency of asphaltene particles to form aggregates is believed to be responsible for numerous problems during bitumen recovery, transportation, and processing, such as formation damage and well plugging, reactor and line coking, refinery tower plugging, and catalyst deactivation. A complete characterization of the fundamental behavior and properties of asphaltenes in bitumen will help solve many of these problems. Second, with current technology a big portion of the asphaltene particles present in the bitumen are either removed as a waste in the beginning through deasphalting process or are dumped after a partial upgrading. A better understanding of the structure of asphaltene particles can lead to the development of more efficient upgrading and refining processes. This can spur innovation in production of hydrocarbon fluids and improve the efficiency of production to a large extent.

1.2. Objectives

The primary aim of the current dissertation was to exploit the rheology as a tool for understanding the nano-micro-macro correlations of two complex fluids of particular interest, namely, a polymeric system (cross linked locust bean gum: artificial mucus simulant) and a dispersion type fluid (bitumen, heavy oils). The principal objectives were:

1. To understand the variations of rheological properties of human airway mucus with changes in their structure and interactions at the molecular scale.

2. To examine the effect of the rheological and surface properties of mucus on the volume concentration and size distribution of bioaerosol droplets generated during simulated coughs, with an aim of helping development of a new class of drugs being developed at the University of Alberta, targeted at controlling the transmission of airborne epidemic diseases by modifying the biophysical properties of human airway mucus.

3. To examine the impact of factors affecting the apparent viscosity of bitumen and heavy oils to reconcile their rheological data with the viscosity measurement data from literature, and to explain the cause of the highly viscoelastic nature of bitumen as compared to conventional oils.

4. To characterize the nano-microstructure of asphaltenes nanoaggregates in bitumen and heavy oil using their rheological behavior, and to compare the nano-microstructure of asphaltene nanoaggregates in the physically and chemically separated native fluids.

1.3. Thesis Outline

This thesis is written in three parts. The first part consists of two chapters. Chapter 1, the current chapter, outlines the introduction and objectives of the thesis, while chapter 2 describes the background theory for this thesis. The fundamentals of rheology and complex fluids, the concepts associated with the rheology of polymeric systems, the equations describing the rheology of dispersions, and the theory of droplet generation and breakup are all discussed in brief in chapter 2.

The second part and the third part of the thesis present the applications of the theory discussed in part 1. Part 2, which is consisted of chapter 3 and chapter 4, presents the application of rheology in a biomedical application, while part 3, which comprises chapters 5 to 8, presents the application of rheology in the field of bitumen and heavy oils. Chapter 3, being the first chapter of part 2, introduces some applied knowledge and theory specifically related to biomedical field. Chapter 4 presents our findings on the effect of rheological properties of mucus on the amount and size distribution of bioaerosol droplets generated during coughing. This chapter is based on the manuscript, "Effect of Artificial Mucus

Properties on the Characteristics of Airborne Bioaerosol Droplets Generated during Simulated Coughing", published in Journal of Non-Newtonian Fluid Mechanics (2010).

Chapter 5, which is the first chapter of part 3, provides an introduction on the concepts and knowledge specifically related to bitumen-heavy oil applications. The next three chapters, from chapter 6 to chapter 8, are based on the manuscripts on rheology and nano-microstructure of asphaltene nanoaggregates in bitumen and heavy oils resulted from this PhD work and published/submitted in various journals.

Finally the thesis is concluded with the final summary and recommendations presented in chapter 9.

References

[1] D.B. Braun, M.R. Rosen, Knovel, The rheology modifiers handbook Practical use & application, William Andrew Pub., Norwich, N.Y, Country, 2000.

[2] P.F. Luckham, M.A. Ukeje, Effect of particle size distribution on the rheology of dispersed systems, J. Colloid Interface Sci. 220 (1999) 347-356.

[3] M. Vasudevan, C.F. Lange, Property dependence of onset of instability in viscoelastic respiratory fluids, International Journal of Engineering Science 43 (2005) 1292-1298.

[4] Y. Maham, M.G. Chodakowski, X.H. Zhang, J.M. Shaw, Asphaltene phase behavior: Prediction at a crossroads, Fluid Phase Equilib. 227 (2005) 177-182.

[5] T.G. Savvidis, D. Fenistein, L. Barre, E. Behar, Aggregated structure of flocculated asphaltenes, AlChE J. 47 (2001) 206-211.

[6] M.H. Ese, K.L. Gawrys, P.M. Spiecker, T.X. Zhang, P.K. Kilpatrick, Asphaltene and naphthenate mechanisms of emulsion stabilization in water-in-crude oil emulsions. 2003, pp. 457-COLL.

[7] J.N. Roux, D. Broseta, B. Deme, Sans study of asphaltene aggregation: Concentration and solvent quality effects, Langmuir 17 (2001) 5085-5092.

[8] I.N. Evdokimov, N.Y. Eliseev, B.R. Akhmetov, Asphaltene dispersions in dilute oil solutions, Fuel 85 (2006) 1465-1472.

[9] V.A.M. Branco, G.A. Mansoori, L.C. De Almeida Xavier, S.J. Park, H. Manafi, Asphaltene flocculation and collapse from petroleum fluids, J. Pet. Sci. Eng. 32 (2001) 217-230.

[10] J. Murgich, O.P. Strausz, Molecular mechanics of aggregates of asphaltenes and resins of the athabasca oil, Pet. Sci. Technol. 19 (2001) 231-243.

[11] J. Murgich, Molecular simulation and the aggregation of the heavy fractions in crude oils, Molecular Simulation 29 (2003) 451-461.

Chapter 2: Theory

2.1. Introduction

The work presented in this dissertation are of multi-disciplinary nature spanning from the basic rheological theories of complex fluids to the mechanism of bioaerosol generation to the chemistry of oil sand bitumen and the physics of asphaltenes nano-aggregate formation. Brief discussions about the theories related to this research are given below.

2.2. Rheology

Let us consider a thin layer of fluid between two parallel plates separated by a distance dy as shown in Fig. 2.1. If the bottom plate is kept fixed and a shearing force F is applied to the top plate, at steady state condition the force F will be balanced by an internal force in the fluid. If the fluid is Newtonian and the flow is laminar, the shear stress will be proportional to the velocity gradient, i.e.

$$F / A = \tau \propto \frac{du}{dy} \tag{2.1}$$

This relation can also be written as

$$\tau = \mu \frac{du}{dy} = \mu \dot{\gamma} \tag{2.2}$$

or
$$\dot{\gamma} = \frac{\tau}{\mu} \tag{2.3}$$
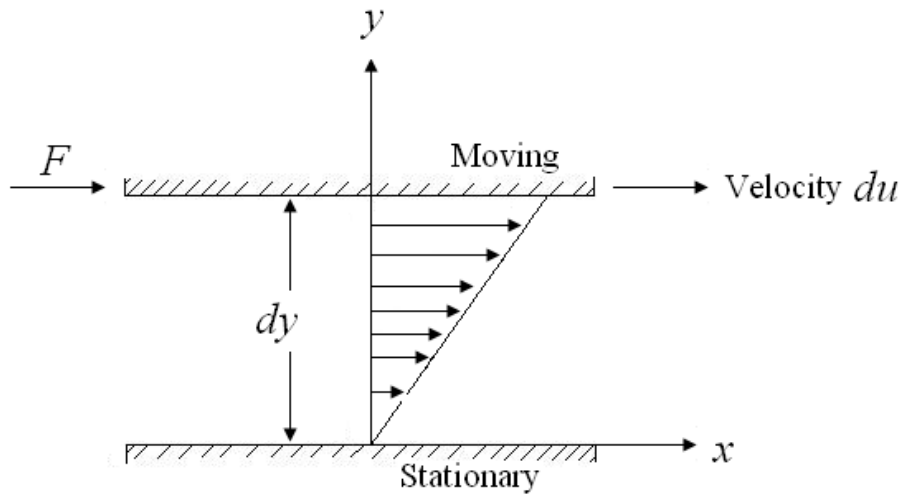
Fig. 2.1. Simple shear of a fluid between two parallel plates, the lower plate being stationary and the upper plate moving at a velocity *du* at a distance of *dy*.

where the proportionality constant, μ, is known as the Newtonian viscosity, $\dot{\gamma}$ is the shear rate, and τ is the shear stress. It should be noted that μ is the tangential force per unit area exerted on layers of fluid a unit distance apart and having a unit velocity difference between them. The Newtonian viscosity is independent of shear rate i.e. the force *F* remains the same whether the top plate is moved faster or more slowly. The shear stress versus shear rate graph, also known as the flow curve, for a Newtonian fluid is therefore a straight line of slope μ as shown in Fig. 2.2. There are numerous examples of materials for which the flow curve is not linear, i.e. the viscosity is not constant and is rather a function of other parameters such as the shear rate, previous history of shear on the fluid etc. In such cases, a new branch of natural sciences, rheology, emerged nearly half a century ago, is needed for proper characterization of the fluid properties and flow behavior.
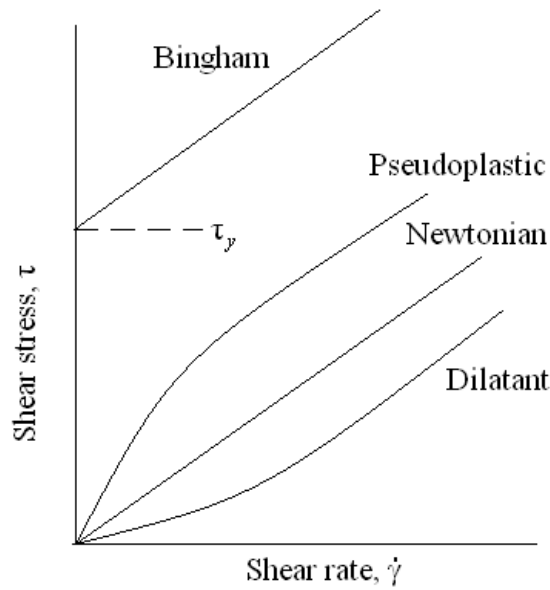
Fig. 2.2. Flow curves for various types of time-independent non-Newtonian fluids along with that of a Newtonian fluid

In essence, rheology is the science that deals with the way materials deform when forces are applied to them [1]. The term rheology is most commonly applied to the study of liquids and liquid-like materials such as paint, catsup, oil well drilling mud, bitumen, blood, and polymer solutions; although it also deals with the study of solids such as in metal forming and stretching of rubber [1]. There are two principal aspects of rheology. One aspect involves the development of constitutive behavior (i.e. force-deformation or stress-strain relationship) of a material, while the second aspect deals with the development of relationships that show how rheological behavior is influenced by the structure and composition, and vice versa. The current dissertation utilizes the second aspect of rheology in a slightly new way, i.e. to find out how rheological properties influence the behavior of

droplet generation and breakup of complex polymeric/biological fluids; and also to see what information about the molecular structure of viscoelastic dispersions, for example size shape etc of nano-micron size asphaltene aggregates in bitumen and heavy oil, can be obtained from their rheological studies. A key word that often comes forward in almost all rheological studies is "complex fluid", a brief introduction to which is given below:

2.3. Complex Fluids

Complex fluids are also known as non-Newtonian fluids. A complex or non-Newtonian fluid is one which possesses both elastic and viscous properties, i.e. although the fluid might be viscous, it exhibits elastic behavior at the same time. There is, therefore, an additional term in the expression of shear rate (Eqn. 2.3). The total rate of shear is therefore given by equation 2.4 instead of Eqn. 2.3.

$$\dot{\gamma} = \frac{\tau}{\eta_o} + \frac{\tau^{'}}{G} \tag{2.4}$$

Here G is called the rigidity modulus, η_o is known as the constant low shear rate Newtonian viscosity coefficient also called zero shear viscosity, and τ' is additional stress resulted due to the elastic properties of the material.

The rheological behavior (e.g. flow curve) of a complex fluid can be either time-independent or time-dependent. In case of time-independent behavior, the flow curve may take different shapes, as shown in Fig. 2.2, depending on whether the fluids under consideration are:

(i)   Bingham Plastic: Fluid with a straight line flow curve having an intercept, τ_y, on the shear stress axis.

(ii)   Pseudoplastic (also known as shear-thinning fluid): The flow curve is nonlinear, and follows a power law relation. The viscosity decreases with increasing shear rate.

(iii)   Dilatant fluids: Similar to pseudoplastic fluid, in the sense that it has no yield stress, except that in this case the viscosity increases with the increasing shear rate.

In case of time dependent behavior, the fluids may be classified into two types:

(i)   Thixotropic fluids: in this case viscosity decreases with increasing duration of shear.

(ii)   Rheopectic fluids: viscosity increases with increasing duration of shear.

2.4. Mechanical Analogies of Complex Fluids

In classical mechanics the mechanical analogy of a Hookean solid (purely elastic material) is a spring while that of a Newtonian liquid (purely viscous material) is a dashpot. Since viscoelastic materials exhibit both viscous resistance to deformation and elasticity, in rheology, the constitutive relation between stress and deformation for viscoelastic materials are obtained using models that are made up of series and parallel combinations of springs and dashpots. The simplest mechanical models analogous to a viscoelastic material are: (i) a single Voigt

element consisting of a parallel combination of a spring and dashpot (as shown in Fig. 2.3a), and (ii) a   single Maxwell element consisted of a spring and dash-pot in series (as shown in Fig. 2.3b). A simple Voigt element or Maxwell element is not sufficiently general to adequately describe the behavior of real viscoelastic materials. In order to generalize these models for real fluids, a number of similar Voigt elements connected in series (as in Fig. 2.4a) or a set of Maxwell elements connected in parallel (as in Fig. 2.4b) are taken as generalized models. Such models are known as generalized Voigt bodies and generalized Maxwell bodies respectively. The equation of motions and the constitutive behavior of these model systems can be found elsewhere [2].

(a)   (b)
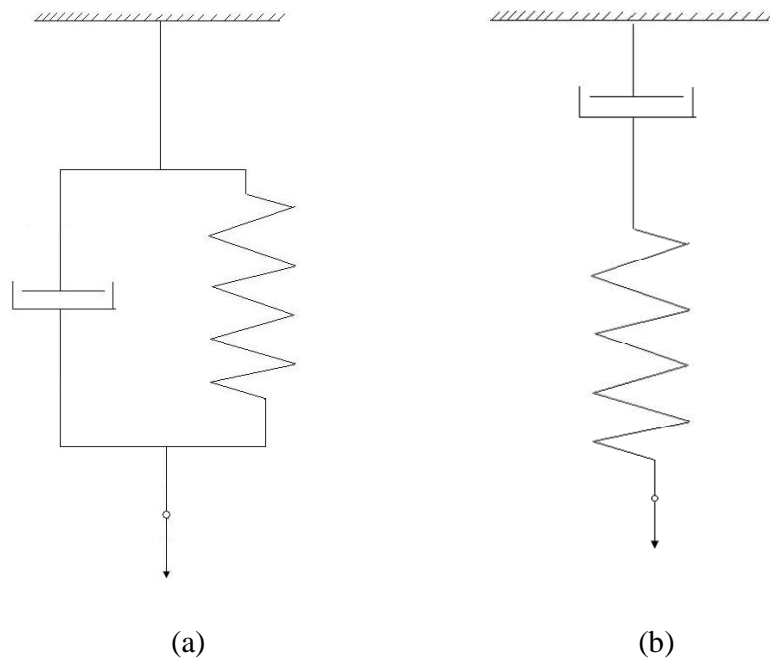
Fig. 2.3. Basic mechanical elements for modeling viscoelastic materials, (a) Voigt element, (b) Maxwell element

(a)

(b)
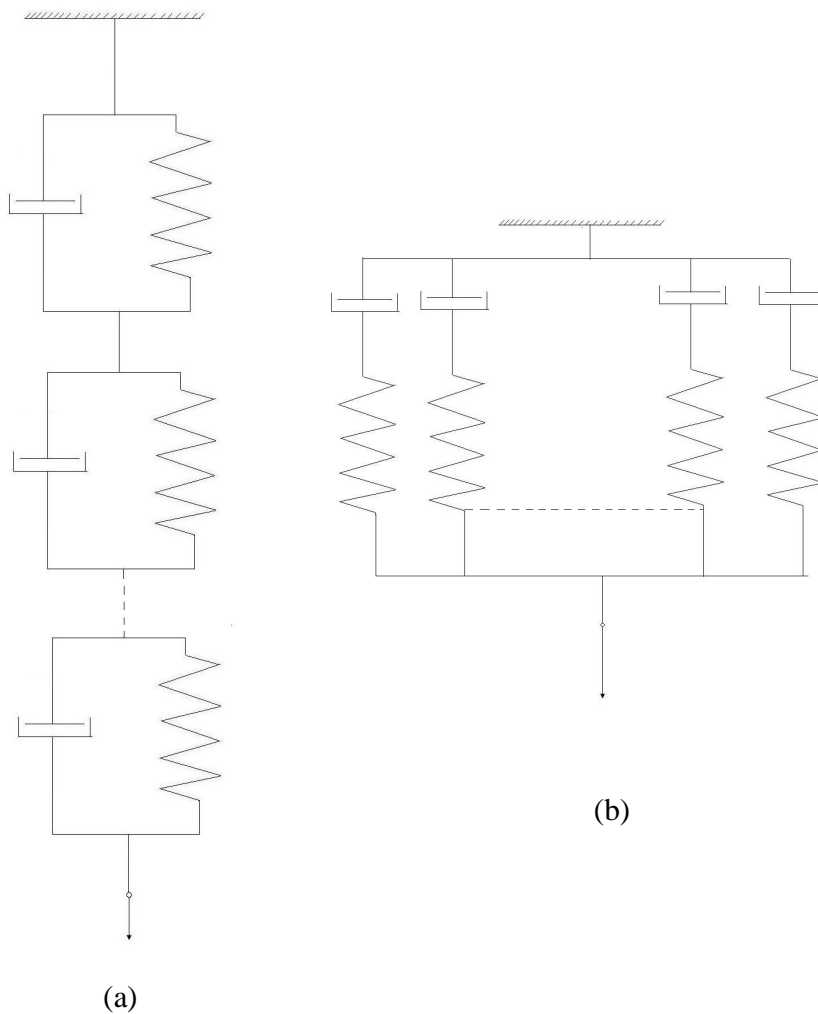
Fig. 2.4. Generalized models for representing viscoelastic materials, (a) generalized Voigt body, (b) generalized Maxwell body.

2.5. Rheological Characterization of Complex Fluids

There are numerous experimental techniques available for characterizing the behavior of complex fluids. These techniques can be broadly classified into

     (i)   steady shear experiments

     (ii)   stress relaxation experiments

(iii)   creep experiments, and

(iv)   oscillatory (dynamic) shear experiments

The theory and detail information regarding these various experimental methods can be found in literature [2]. In this dissertation, the oscillatory shear experimental method has been used for all rheological characterization, with a few exceptions where the steady shear experiments were employed. The theory of steady shear is straightforward, hence only a brief discussion about the oscillatory shear experiments is provided here. In oscillatory shear measurement, a sinusoidal stress or strain signal is applied on the sample, and the material's response in terms of strain or stress is measured respectively. If the applied sinusoidal strain signal is as given by equation 2.5, provided that the deformation is within linear viscoelastic limit, the stress will be as given by equation 2.7. The viscoelastic properties in that case are obtained using equations 2.8 to 2.14.

$$\gamma = \gamma_0 \sin(\omega t) \tag{2.5}$$

$$\frac{d\gamma}{dt} = \dot{\gamma} = t\gamma_0 \cos(\omega t) = \dot{\gamma}_0 \cos(\omega t) \tag{2.6}$$

$$\sigma = \sigma_0 \sin(\omega t + \delta) \tag{2.7}$$

$$\text{Storage modulus, } G' = \frac{\text{Stress}}{\text{Strain}} \cos(\text{Phase angle}) = \frac{\sigma}{\gamma} \cos\delta \tag{2.8}$$

$$\text{Loss (viscous) modulus, } G'' = \frac{\text{Stress}}{\text{Strain}} \sin(\text{Phase angle}) = \frac{\sigma}{\gamma} \sin\delta \tag{2.9}$$

$$\text{Complex modulus, } G^* = \frac{\text{Stress}}{\text{Strain}} = \frac{\sigma}{\gamma} = \sqrt{G'^2 + G''^2} \tag{2.10}$$

16

$$\text{Imaginary viscosity, } \eta^{''} = \frac{\text{Elastic modulus}}{\text{Frequency}} = \frac{G^{'}}{\omega} \qquad (2.11)$$

$$\text{Dynamic viscosity, } \eta^{'} = \frac{\text{Viscous modulus}}{\text{Frequency}} = \frac{G^{''}}{\omega} \qquad (2.12)$$

$$\text{Phase angle, } \delta = \tan^{-1}(\frac{G^{''}}{G^{'}}) \qquad (2.13)$$

$$\text{Complex Viscosity, } \eta^{*} = \frac{\text{Complex modulus}}{\text{Frequency}} = \frac{G^{*}}{\omega} = \sqrt{\eta^{'2} + \eta^{''2}} \qquad (2.14)$$

2.6. Rheological Behavior of Gel-type Complex Fluids

Polymeric materials including solutions, melts, and crosslinked systems, exhibit both viscous resistance to deformation and elasticity [1]. The reason for such behavior can be explained by the interrelations between the physical properties (including rheological properties) and molecular structure. A polymer molecule is a long chain with many joints that allow relative rotation of adjacent links as shown in the schematic representation in Fig. 2.5. The presence of this large number of joints makes the molecule quite flexible and allows various different configurations of the molecule. At a given condition there is a unique average value of the end-to-end distance for the molecules of a polymeric liquid that is in equilibrium state. Deforming the liquid alters this average length, but when the deformation is stopped, Brownian motion tends to return the average value of end-to-end distance to its equilibrium value. This results in elastic and relaxation phenomena in polymeric liquids. Additionally when a polymeric solution

17
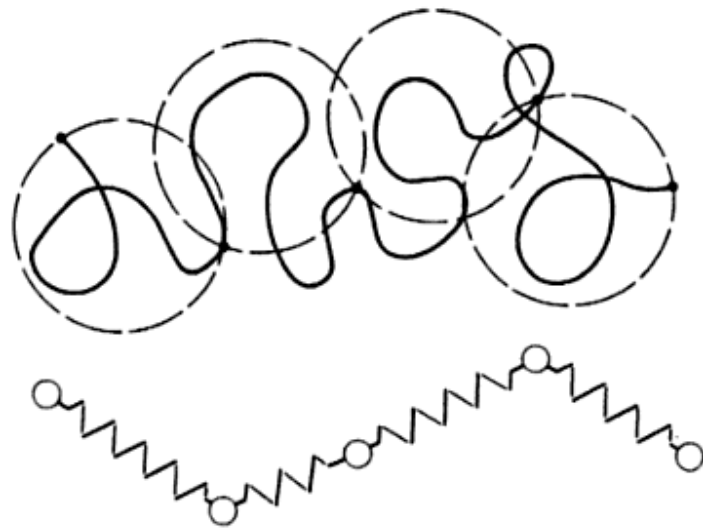
Fig.2.5. Representation of flexible randomly coiled macromolecule of a polymeric

system (bead-spring model) taken from Ferry [2].
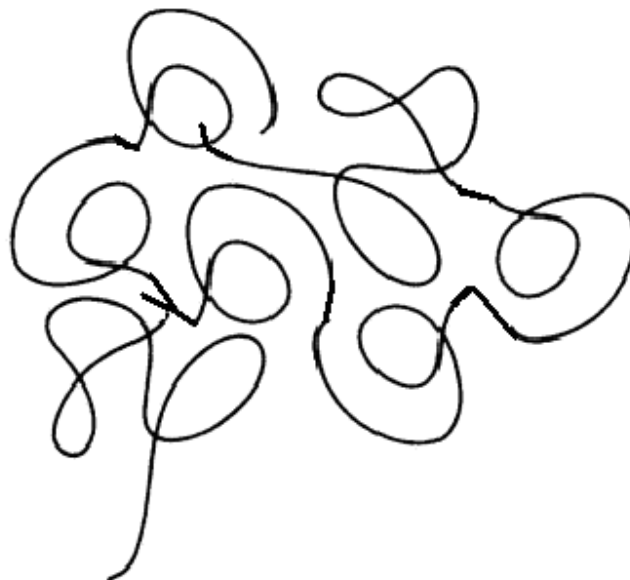
Fig. 2.6. Symbolic representation of entanglement in long chain polymeric molecules
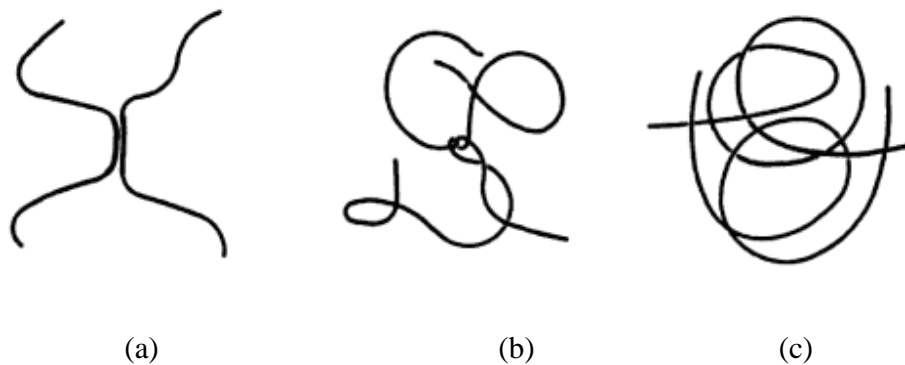
Fig. 2.7. Symbolic representation of crosslinking in polymeric molecules, (a) locus of coupling, (b) Locus of adherence or temporary crosslink, (c) long-range contour loop [2]

undergoes deformation, a dissolved molecule is dragged along with it, but the polymer molecule is so large that different parts of it are exposed to different solvent velocities. In other words, the solvent moves relative to the segments of the polymer molecule and exerts forces on these segments, which change the shape (conformation) and orientation of the molecules. Thus the deformation of a polymeric liquid can alter the configuration and orientation and, hence, the physical nature of the fluid. This in turn alters the rheological properties of the fluid. At high shear rates the shape of the polymer molecules is different from that at low shear rates, and this alters the solution's resistance to flow and thus its viscosity. This results in a shear rate dependence of viscosity [2]. Besides, each flexible threadlike molecule pervades an average volume much greater than atomic dimensions and it continually changes the shape of its contour as it wriggles and writhes with its thermal energy [2]. In doing so, the molecules get entangled within themselves as well as with other surrounding molecules as

shown in Fig. 2.6. The higher the entanglement, the higher will be the viscosity of the system. Finally, it is conceivable that specific spots of intermolecular attraction can occur which may lead to linkage formation between one part of a molecule and a different part of another molecule. Such intermolecular crosslinks enhance the elastic behavior of the material. Fig. 2.7 shows a schematic representation of such crosslinks in a hypothetical polymeric system.

2.7. Rheological Behavior of Dispersion-type Complex Fluids

Dispersions are another type of complex fluids that can show various viscoelastic behaviors. Einstein [3, 4] (1906) suggested that for a dilute dispersion of non-interacting rigid spherical particles in a Newtonian fluid, it is sufficient to analyze only the motion of the fluid around a single sphere. At very low shear rate, for dilute suspensions (very low particle volume fraction, e.g. $\varphi < 2\%$) of non-interacting hard spheres in a Newtonian fluid Einstein considered the far-field hydrodynamics and derived:

$$\eta_r = \eta \, / \, \eta_c = 1 + 2.5 \; \varphi \qquad\qquad (2.15)$$

where η_r is the relative viscosity, η_c is the viscosity of the continuous phase, η is viscosity of dispersion, and φ is volume fraction of particles. Batchelor [5] (1970) considered semi dilute suspensions. Initially, he neglected the Brownian motion

and included the near-field hydrodynamic interaction in Einstein's model, thus modifying the Einstein's equation to:

$$\eta_r = 1 + 2.5\,\varphi + 7.6\,\varphi^2 \qquad\qquad (2.16)$$

Later, Batchelor [6] (1972) included Brownian motion in his analysis and for semi dilute suspensions found;

$$\eta_r = 1 + 2.5\,\varphi + 6.2\,\varphi^2 \qquad\qquad (2.17)$$

Eqn. (2.15) (Einstein's equation) is applicable to a dispersion of only up to 2% concentration [7], and Equations (2.16 and 2.17) (Batchelor's equations) are limited for concentrations up to about 12%. For more concentrated dispersions, researchers formulated various semi-empirical equations in such a way that at very low concentration they satisfy Einstein's equation and/or at some finite concentrations viscosity becomes infinite [8]. One such equation is that of Krieger and Dougherty [9] (1959) given by

$$\eta_r = 1 / (1 - \varphi / \varphi_{max})^{[\eta]\,\varphi_{max}} \qquad\qquad (2.18)$$

where $[\eta]$ is known as intrinsic viscosity, and φ_{max} is the maximum packing fraction (at $\varphi = \varphi_{max},\ \eta \to \infty$). The value of φ_{max} might range from 0.52 for a simple cubic packing to 0.74 for face centered cubic packing [10] provided that

the particles are uniform spheres. Another similar equation used widely in literature, for example Berli & Quemada [11], and Brady [12] is that of Quemada [13] given by

$$\eta_r = 1 / (1 - \varphi / \varphi_{max})^2 \qquad\qquad (2.19)$$

Eiler [14] derived another semi-empirical Eqn. given by

$$\eta_r = 1 + ([\eta] \varphi /2)/(1 - \varphi / \varphi_{max})^2 \qquad (2.20)$$

Pal-Rhodes [15] introduced the effect of particle - solvent interaction and proposed

$$\eta_r = (1 - K_s\varphi)^{-2.5} \qquad\qquad (2.21)$$

where K_s = Solvation coefficient. Mooney [16] accounted for the polydispersity of the particles and introducing a crowding factor of $(1 - \varphi / \varphi_{max})^2$, he derived

$$\eta_r = \exp(2.5 \varphi /(1 - K_p \varphi/ \varphi_{max})^2) \qquad (2.22)$$

As the particle concentration increases, dispersions start showing non-Newtonian behavior, i.e. viscosity becomes shear rate dependent. de Kruif [17] (1986) gave two separate equations for low shear rate and high shear rate viscosity as:

$$\eta_o / \eta_c = (1- \varphi / 0.63)^{-2} \tag{2.23}$$

$$\eta_\infty / \eta_c = (1- \varphi / 0.71)^{-2} \tag{2.24}$$

where η_o is the viscosity at zero shear rate and η_∞ is the viscosity at infinite shear rate (very high shear rate). For viscosity at any intermediate value of shear rate de Kruif's equations can be used together with Krieger's [18] (1972) equation given by

$$\eta = \eta_o + (\eta_o - \eta_\infty)/ (1+2.32 \, Pe) \tag{2.25}$$

where Pe is Peclet number. Rutgers [8] presented an extensive survey of the equations developed until his time (1962) relating viscosity with volume concentration of dispersion. He identified 96 equations from the literature and showed that the very large number of equations could be reduced to only five or even two or three valuable functions. Sudduth [19] (1993) later showed that the reduced number of functions identified by Rutgers can again be represented by a single generalized form given by

$$d\eta / \eta = (1- K \varphi)^{-\sigma} d\varphi \tag{2.26}$$

Sudduth interpreted K as the crowding factor, and σ as the particle interaction coefficient, and showed that the generalized equation takes the form of Arrhenius

equation, Krieger - Dougherty equation, and Mooney equation when σ is taken to be 0, 1 and 2 respectively. Similarly other equations can also be derived from Eqn. 2.26.

As mentioned earlier, Einstein's and Batchelor's equations are valid only at very low concentrations, while the other equations described above (Eqn. 2.18 to Eqn. 2.26), that are valid at higher concentrations are mostly empirical or semi-empirical type equations. The theoretical equation valid for non-interacting hard sphere system for a concentration of up to 31% is that of Vand [20] given by

$$\eta_r = 1 + 2.5 \, \varphi + 7.349 \, \varphi^2 \qquad (2.27)$$

Vand accounted for the hydrodynamics (streaming of the liquid around the suspended particles), and the mutual interaction of the particles and their collisions, to derive this theoretical equation in the form of an infinite series, and then derived the values of the constants in the formula for the case of rigid, non-solvated, non-interacting particles as given in Eqn. 2.27

Another set of theoretical equations, claimed to be applicable at all concentrations, derived using an alternative approach are those of Roscoe [21], given by:

$$\eta_r = (1 - 1.35 \, \varphi)^{-2.5} \qquad \text{uniform spheres} \qquad (2.28)$$

$$\eta_r = (1 - \varphi)^{-2.5} \qquad \text{polydisperse spheres} \quad (2.29)$$

Thus for a dispersion of non-interacting uniform rigid spherical particles in a Newtonian fluid, relative viscosity can be predicted using various hard sphere models. [5, 6, 7] As the size, shape, size distribution, and surface texture, of particles deviate from those of an ideal hard sphere, the relative viscosity of dispersions changes accordingly. Numerous empirical and semi-empirical models have been proposed to account for specific cases. [5, 6, 7] However, Sudduth [19] showed that many of these equations can be reduced to a single generalized form:

$$\ln(\eta/\eta_0) = \left(\frac{[\eta]}{k}\right)\left(\frac{1}{\sigma-1}\right)\left[(1-k\varphi)^{1-\sigma} - 1\right] \qquad (2.30)$$

Where η is the viscosity of dispersion, η_o is the viscosity of the continuous phase, $[\eta]$ is intrinsic viscosity, φ is the volume fraction of particles, k is the crowding factor, and σ is the particle interaction coefficient. In this thesis the generalized Sudduth equation (Eqn. (2.30)) is used to interpret rheological data.

2.7.1. Colloidal Forces Active in Dispersions

There are three main types of colloidal forces that can act between particles in dispersions: (i) electrostatic forces, (ii) van der Waals forces, and (iii) steric forces. Electrostatic forces are generally operative, through pH and zeta potential, in aqueous or polar media. The van der Waals forces are attractive forces. The range of these forces is of the order of the particle size for sizes up to ~ 200 nm and increasingly smaller than the particle size for larger sizes. Steric forces, which

result from the presence of adsorbed or grafted macromolecules at the surface, are usually repulsive in nature, and are dependent on the surface layer thickness, surface density and the solubility of the stabilizing chains.

A competition between the attractive and repulsive colloidal forces governs the extent of aggregation and deaggregation of particles in dispersions. In addition to the above interparticle forces, there can be forces due to surface interaction between the particles and the surrounding fluid as well as forces due to Brownian motion.

2.7.2. Dilute, Semi-dilute and Concentrated Dispersions

Depending upon the volume concentration of dispersed solid, the dispersions can be divided into three types, namely dilute, semi-dilute, and concentrated dispersions. The flow properties of a colloidal dispersion are influenced by the type of dispersion.

2.7.2.1 Dilute dispersions

Dilute dispersions in Newtonian fluids act like Newtonian fluids. In this case volume concentration is very low ($\varphi <5\%$), and viscosity is not a function of shear rate [22]. For dilute dispersions particle size is not an important variable. However, viscosity depends upon the shape (i.e. whether spherical or non-spherical) of the dispersed particles [23]. The effect of size distribution, i.e.

polydispersity, is also negligible for dilute dispersions   [23], and this is true for both nano and micro sized particles as long as the size of the dispersed particles are large (at least ten times larger) compared to the size of the molecules of the continuous medium. The relative viscosity relation for dilute dispersions follows the well-known Einstein equation ($\mu/\mu_r = 1 + 2.5 \varphi$)

2.7.2.2. Semi-dilute and concentrated dispersions

Semi-dilute dispersions ($\varphi = 5\% \sim 18\%$) are particularly important for this study, since the asphaltene concentration of bitumen and crude oil ($\varphi = 10 \sim 18\%$) appear to fall in this range. On the other hand vacuum residues can be considered as concentrated dispersions ($\varphi > 18\%$) as their asphaltene content is very high. The effects of various parameters i.e. size, polydispersity, aggregation and shape of particles on relative viscosity for semi-dilute and concentrated dispersions are shown qualitatively in Figs. 2.8, and are discussed below.

 (a) *Effect of particle size*

The effect of particle size on the dispersion viscosity is apparently a debated issue. Parkinson et al. [24] studied monodisperse suspensions of poly methyl methacrylate (PMMA) of 0.1 μm, 0.6 μm, 1 μm, and 4 μm diameter in Nujol. They used an emphiphatic co-polymer, in which the soluble stabilizing component was the hexamer of 12-hydroxy-stearic acid, to stabilize the
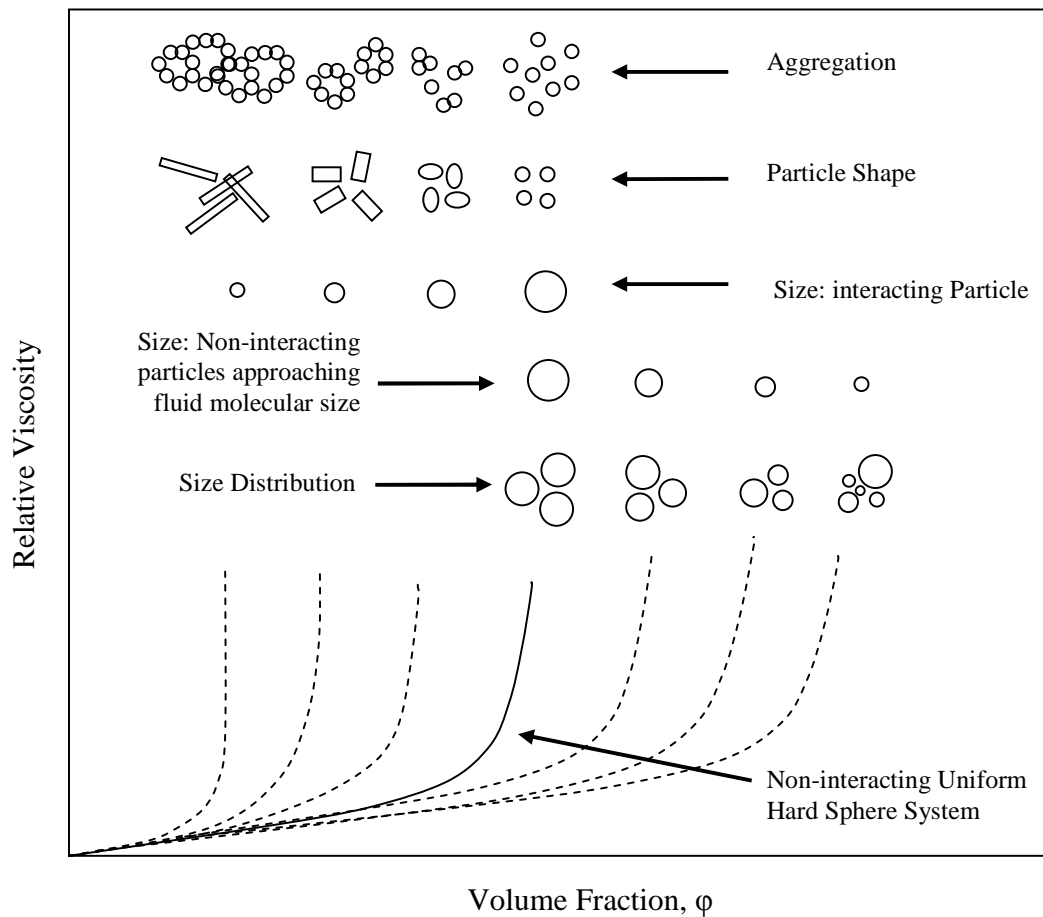
Fig. 2.8. Qualitative effect of size, shape, size distribution and aggregation of particles on the relative viscosity of colloidal dispersions

suspension. For the range of volume fraction from 0 to 12%, they found a clear correlation between particle size and suspension viscosity. Smaller particles showed higher relative viscosity for all volume fractions within the range of their study. In contrast to this, Van der Werrf et al. [25] studied suspension of sterically stabilized silica particles in cyclohexane, the particle size being in the range of 56 nm to 220 nm, with the results suggesting that viscosity was size independent for the whole range of volume concentration from 0 to 60%. Ferrini et al. [26] studied a number of spherical particles including glass beads and acrylic powder

(kallodoc), and non-spherical particles including coal in different types of suspending fluids. They also found that relative viscosity was independent of particle size. Chong et al. [27] studied a suspension of closely sized glass beads in a low molecular weight polyisobutylene (PIB) using a tube flow viscometer. The particle size ranged from 53.8 to 236 microns and the solids volume fraction ranged from 0.45 to over 0.6. The relative viscosity in this case also was found to be independent of particle size.

The experimental data in the literature on particle size effect seems to be heavily contradictory. But after carefully analyzing various literature data, we reached the conclusion that the viscosity of non-interacting hard spheres, when the particle size is larger by one order of magnitude compared to the size of molecules of the surrounding fluid, is independent of particle size. The results that show variation in viscosity with particle size, at all volume fractions do so because of the surface interaction between the particles and the fluid. Formation of an associated fluid layer around the particles, for example, in the systems where particles interact with the fluid, increases the effective volume fraction, thereby increasing the viscosity. The surface area to volume ratio is inversely proportional to particle size, while the thickness of hydration layer around the particles is expected to be the same order of magnitude for all size of particles. Therefore, in dispersions containing small particles the hydration layers will have more pronounced effects. Hence, for the same volume fraction, dispersions with smaller size particles will offer more resistance to the flow, whereby the increase of viscosity will be much

higher compared to the systems containing larger particles at the same concentration.

The presence of particle size effect at higher concentrations, in the systems where there is no size effect at lower volume fractions, is attributed to the magnified inter particle interactions. The inter-particle interaction depends on the particle size and the volume concentration. The larger the particle size, the greater the distance between the particles at any given concentration. The inter particle distance equals the particle diameter at a volume fraction of 9.3%. That is, for a suspension of 500 nm particle size, the inter particle distance at 9.3% volume fraction of solid will be 500 nm. But for the same particle size, at a 50% volume fraction the average inter-particle distance would be 70 nm. If the particle size is reduced to 100 nm, the average inter-particle distance for the suspension with 50% volume fraction would be 14 nm. At such small values of average inter particle distance there would be a significant number of particles in direct contact with their neighboring particles, and the friction at the surface between adjacent particles would play significant role, thereby influencing the viscosity.

While the absolute particle size does not affect the viscosity of non-interacting hard sphere dispersions at moderate concentrations, the relative size of the dispersed particles (in comparison to molecular size of the liquid) has a significant role on the rheological behavior. Machay et al. [28] studied viscosity of polystyrene nano-particles suspended in a polystyrene polymer. Two types of

polystyrene particles: smaller in size (6-10 nm diameter) compared to the liquid polymer molecules (15-30 nm) and larger in size (1.6 μm) compared to the polymeric molecules were used. While the addition of 1.6 μm microspheres resulted in a conventional increase of relative viscosity, a clear evidence of decrease of viscosity for semi-dilute suspension of mass fraction (0-10%) was found for the 5-10 nm particles. This infers that depending upon whether the added particles are smaller, equal or larger in size compared to the molecular size of liquid phase, the viscosity can decrease, remain unchanged or increase, respectively.

(b) *Effect of the particle size distribution*

The effect of the size distribution is almost unanimously accepted by researchers. Experiments by different researchers have shown a 2 to 20 fold reduction in viscosity due to effect of polydispersity. It is believed that for polydisperse suspensions, small particles can fit between the larger ones and act like ball-bearings to minimize the particle interactions, which result in lower viscosity. However, since the particle-particle interaction plays significant role only at high particle concentrations, for dilute and lower range of semi-dilute suspensions, polydispersity effect should be negligible.

Chong et al. [27] investigated the viscosity of bimodal suspensions of glass beads in PIB (polyisobutelene) using an orifice viscometer. The suspensions had 25% small spheres in total solid phase. The particle size was varied between 25 and

31

250 μm, the particle size ratios were D/d = 7.2, 3.2 and 2.1, and the volume concentration of smaller particle in all cases was 25%. Results showed that the relative viscosity decreases markedly as the particle size ratio decreases. The fact that the relative viscosities of bimodal suspensions decrease significantly as the number of small spheres increases indicate that the fine spheres act like ball bearings between large spheres [27].

(c) *Effect of particle aggregation*

Aggregation of the particles immobilizes the fluid between the aggregated particles. This can be seen as transferring volume from the continuous phase to the dispersed phase, which increases the effective volume concentration of the solids, thereby increasing the viscosity.

(d) *Effect of particle shape*

Non-spherical particles in dispersions result in a higher viscosity compared to that of spherical particles. The higher the aspect ratio of the non-spherical particles, the higher will be the viscosity. For the same value of aspect ratio, fiber shaped or cylindrical particles will show higher viscosity compared to that of disc-type particles.

(e) *Effect of shear rate*

Depending upon the shear rate and concentration, dispersions can show a shear thinning or a shear thickening behavior. Rheologists agree that the change of

viscosity with shear rate appears because of interactions of the dispersed particles with the surrounding medium and the neighboring particles [29]. It should be noted that for semi dilute suspensions of non-interacting colloidal spheres, the forces affecting viscosity are Brownian forces, viscous hydrodynamic forces and inter particle forces [29]. According to Probstein [30] the non-Newtonian behavior of suspension viscosity is observed when colloidal size particles are present, and the shear rate dependence is the result of a competition between the viscous forces, surface forces, and forces associated with Brownian motion.

Mewis [31] explains that, when increasing the shear rate the Brownian motion will at a certain stage become slower than the convective motion. From then on, the contribution of the Brownian motion to the viscosity will gradually decrease with increasing shear rate, whereas the hydrodynamic contribution remains relatively constant. This causes the viscosity to drop and a shear thinning region to develop. At still higher shear rates, the Brownian contribution becomes negligible, but an increase in hydrodynamic effects can either compensate the decrease, causing a pseudo-Newtonian high shear plateau, or overcompensate producing a shear-thickening zone [31]. Batchelor [7] explained the shear thinning behavior in terms of the tendency for bulk flow to align the largest diameter of the particles preferentially with the main streamlines in opposition to the (rotational) spreading effect of Brownian motion.

33

It is also generally accepted that the non-Newtonian behavior of dense suspensions results from changes in microstructure under shear [32]. For example, shearing can break down particle aggregates into smaller particles, which can cause shear thinning effect.

2.7. Droplet Formation and Breakup in Shear Flow

Even though not much work has been done on the interaction of the mucus layer with pulmonary airflow and the bioaerosol droplet generation during coughing sneezing etc., extensive research has been done on droplet generation and breakup from liquid jet, spray, atomizers etc. over the last two centuries. The first of such work done on the breakup of flat sheets that spread from two equal co-axial colliding jets is traced back to Savart (1833) [33] and that on the instability and break up of a liquid jet is traced back to Plateau (1873) [34]. Using surface energy arguments, Plateau [34] proposed that, to achieve a state of minimum surface energy, a round jet of diameter D_l must break into equal segments whose length must be about 4.5 D_l. Rayleigh (1879) [35] demonstrated that this breakup results from a hydrodynamic instability caused by surface tension and occurs at a relatively low jet Reynolds number. Weber (1931) [36] extended Rayleigh's analysis and showed that the liquid viscosity has a stabilizing effect that lowers the breakup rate and increases the size of the observed droplets. Taylor (1959, 1960) [37, 38] studied the basic linear wave motions within flat sheets. Bibliographies of the work afterwards tend to be very lengthy. Readers may consult the reviews of liquid atomization mechanisms by Reitz and Bracco [39],

Krzeckowski [40], Pilch and Erdman [41], Hsiang and Faeth [42], and Wu and Faeth [43].

Based on the results and observations from the above listed literature the droplet generation/breakup phenomena can be broadly classified into three types: 1. Gravity driven single droplet formation [44, 45], 2. Jet breakup or Jet-driven droplet formation [46, 47, 48], and 3. Spray atomization [49]. The gravity-driven droplet formation occurs in three stages namely stretching, elastic drainage, and surface recoil events.

The breakup phenomena of liquid drops in case of jet breakup and atomization could be classified roughly into two stages [50]. During the first stage of the drop breakup process, the drops experience a shape change, and subsequent droplet breakup starts from a basic flattened liquid disk shape. During the second stage of the drop breakup process, the distorted drops undergo disintegration, and depending on the Weber number of the flow, at least three breakup regimes can be identified which are termed as bag breakup regime (12<We<80), stretching/thinning breakup regime (80<We<210) and catastrophic or explosive breakup regime (We>210). A brief description of the three regimes is as follows:

2.7.1. Bag breakup regime
When a liquid jet is discharged into a stagnant gas, or a gas stream is passed over a liquid layer, a Rayleigh instability manifests provided that the jet diameter is

small and the jet Reynolds number is small too (of the order 10^2). As the perturbations grow and a sheet begins to form, spanwise perturbations at the rim of the sheet also grow. In time, the sheet's thickness and rim radius decrease until surface tension forces become of the order of the aerodynamic forces. The rim is finally disrupted by aerodynamic forces and Rayleigh instability. Behind the rim, the liquid sheet is blown out into a bag, forming a membrane, which breaks into small drops. This mechanism is characteristic of the relatively small Weber numbers where membrane breakup occurs. This breakup mechanism is termed as bag breakup and it is similar to the scenario observed in numerical simulations by Keller et al (1984) [51], Li (1996) [52], and Zaleski et al (1998) [53].

2.7.2. Stretching or thinning breakup regime

When the Weber number is increased, the breakup process is distinctly different from that in the bag breakup regime. The very thin edge sheet of the flattened disk, which has a low inertia, is deflected in the direction of the air flow stream. The edges of the saucer-shaped disks are blown out into thin sheets by drag forces, and the sheets are split into fine filaments or ligaments, which themselves break up into very small drops.

2.7.3. Catastrophic breakup regime

In the case of catastrophic break up as noted by Liu and Reitz [50], the edge of saucer-shaped flattened disks is drawn out into a thin sheet by the suction stress at the equator of flattened disks due to the high-speed gas flow. The drop is flattened

into the form of a sheet and the accelerating sheet breaks into large fragments by means of the Rayleigh-Taylor instability. Much shorter-wavelength Kelvin-Helmholtz waves are thought to originate at the edges of the fragments, and these waves are stretched to produce ligaments which breakup into micro-size droplets.

2.7.4. Secondary Breakup

As described above, the primary instability of the air/mucus interface leads to the formation of mucus sheets and ligaments that break into drops. Portions of these sheets and ligaments also may detach from the mucus wavy surface. These mucus droplets and lumps of complex shapes are subsequently convected downstream and undergo further breakup as they are subjected to the stresses of the turbulent air flow. In case of large aerodynamic Weber numbers, this secondary breakup generates a large number of smaller droplets resulting in an overall bimodal droplet size distribution.

Following the classical decomposition of the turbulent motion into a mean plus a fluctuating component, we can express the forces acting on the mucus droplets as the sum of a force resulting from the mean relative velocity between the droplet and the air, and a force due to the turbulence fluctuations of the surrounding air. To differentiate between the breakup processes resulting from these two effects, we refer to them as shear breakup and turbulent break up respectively.

The shear breakup can again be one of the three different types depending on the value of the shear Weber number namely, a bag or balloon type breakup (Merrington & Richardson 1947   [54], Kennedy & Roberts 1990   [55]), a stretching/thinning breakup (Liu & Reitz, 1997, Lee & Reitz, 2001) [50, 56], and an explosive or catastrophic breakup (hanson et al 1963   [57], Reinecke & Waldman 1970 [58]).

The droplets generated through the primary breakup and the shear breakup of the secondary breakup stage undergo further breakup due to the turbulent fluctuating stress. It should, therefore, be expected that regardless of the initial break up, the maximum droplet size of the equilibrium droplet distribution function achieved in the far-field should be determined by the final turbulent breakup process, and the overall distribution is most likely to be bimodal or multimodal distribution.

References

[1] J.M. Dealy, K.F. Wissbrun, Melt rheology and its role in plastics processing: Theory and applications, Van Nostrand Renhold, New York, Country, 1990.

[2] J.D. Ferry, Viscoelastic properties of polymers, John Wiley & Sons, New York, Country, 1970.

[3] A. Einstein, Eine neue bestimmung der molekuldimensionen, Ann. Phys 19 (1906).

[4] R. Furth, Investigations on the theory of the brownian movement. Dover, New York, 1956.

[5] G.K. Batchelor, The stress system in a suspension of force-free particles, J. Fluid Mech. 41 (1970) 21.

[6] G.K. Batchelor, J.T. Green, The determination of the bulk stress in a suspension of spherical-particles to order c^2, J. Fluid Mech. 56 (1972) 401-427.

[7] G.K. Batchelor, Effect of brownian motion on bulk stress in a suspension of spherical-particles, J. Fluid Mech. 83 (1977) 21.

[8] I.R. Rutgers, Relative viscosity and concentration, Rheol. Acta Band 2, Heft 4 (1962) 305-348.

[9] I.M. Krieger, T. Dougherty, A mechanism for non-newtonian flow in suspensions of rigid spheres, Trans. Soc. Rheol. 3 (1959) 137-152.

[10] R.E. Baltus, Characterization of asphaltenes and heavy oils using hydrodynamic property measurements. in: O. C. Mullins, and E. Y. Sheu,

(Eds.), Structures and dynamics of asphaltenes. Plenum Press, New york and London, pp. 303-335.1998.

[11] C.L.A. Berli, D. Quemada, Rheological modeling of microgel suspensions involving solid-liquid transition, pp. 7968-7974, 2000.

[12] J.F. Brady, The rheological behavior of concentrated colloidal dispersions, J. Chem. Phys. 99 (1993) 567-581.

[13] D. Quemada, Rheology of concentrated disperse systems and minimum energy-dissipation principle .1. Viscosity-concentration relationship, Rheol. Acta 16 (1977) 82-94.

[14] H. Eilers, Kolloid-Z 97 (1941) 313.

[15] R. Pal, E. Rhodes, Viscosity concentration relationships for emulsions, J. Rheol. 33 (1989) 1021-1045.

[16] M. Mooney, The viscosity of a concentrated suspension of spherical particles, Journal of Colloid Science 6 (1951) 162-170.

[17] C.G. Dekruif, E.M.F. Vanlersel, A. Vrij, W.B. Russel, Hard-sphere colloidal dispersions - viscosity as a function of shear rate and volume fraction, J. Chem. Phys. 83 (1985) 4717-4725.

[18] I.M. Krieger, Rheology of monodisperse latices, Adv. Colloid Interface Sci. 3 (1972) 111-136.

[19] R.D. Sudduth, A generalized model to predict the viscosity of solutions with suspended particles. I, J. Appl. Polym. Sci. 48 (1993) 25-36.

[20] V. Vand, Viscosity of solutions and suspensions .1. Theory, Journal of Physical and Colloid Chemistry 52 (1948) 277-299.

[21] R. Roscoe, The viscosity of suspensions of rigid spheres, British Journal of Applied Physics 3 (1952) 267-269.

[22] C.R. Wildemuth, M.C. Williams, A new interpretation of viscosity and yield stress in dense slurries - coal and other irregular particles, Rheol. Acta 24 (1985) 75-91.

[23] C.R. Wildemuth, M.C. Williams, Viscosity of suspensions modeled with a shear-dependent maximum packing fraction, Rheol. Acta 23 (1984) 627-635.

[24] Parkinso.C, Matsumot.S, P. Sherman, Influence of particle-size distribution on apparent viscosity of non-newtonian dispersed systems, J. Colloid Interface Sci. 33 (1970) 150-&.

[25] J.C. Vanderwerff, C.G. Dekruif, Hard-sphere colloidal dispersions - the scaling of rheological properties with particle-size, volume fraction, and shear rate, J. Rheol. 33 (1989) 421-454.

[26] F. Ferrini, D. Ercolani, B.D. Cindio, L. Nicodemo, L. Nicolais, S. Ranaudo, Shear viscosity of settling suspensions, Rheol. Acta 18 (1979) 289-296.

[27] J.S. Chong, Christia.Eb, A.D. Baer, Rheology of concentrated suspensions, J. Appl. Polym. Sci. 15 (1971) 2007-&.

[28] M.E. Mackay, T.T. Dao, A. Tuteja, D.L. Ho, B. Van Horn, H.C. Kim, C.J. Hawker, Nanoscale effects leading to non-einstein-like decrease in viscosity, Nature Materials 2 (2003) 762-766.

[29] J. Bergenholtz, Theory of rheology of colloidal dispersions, Current Opinion in Colloid & Interface Science 6 (2001) 5.

[30] R.F. Probstein, M.Z. Sengun, T.C. Tseng, Bimodal model of concentrated suspension viscosity for distributed particle sizes, J. Rheol. 38 (1994) 811-829.

[31] J. Mewis, J. Vermant, Rheology of sterically stabilized dispersions and latices, Prog. Org. Coat. 40 (2000) 111-117.

[32] J.J. Stickel, R.L. Powell, Fluid mechanics and rheology of dense suspensions, Annual Review of Fluid Mechanics 37 (2005) 129-149.

[33] F. Savart, Ann. Chem. Phys. 59 (1833) 113.

[34] J. Plateau, Stattique experimentale et theoretique des liquids soumie aux seules forces moleicularies. Paris: Chanthier vallars, (1873).

[35] L. Rayleigh, On the instability of jets, , London Math. Soc. 10 (1879) 361-371.

[36] C. Weber, Zum zerfall eines flussigkeitstrahles (on the disruption of liquid jets), Z. Angew. Math. Mech. 2 (1931).

[37] G.I. Taylor, The dynamics of thin sheets of fluid i. Water bells, Proc. Roy. Soc. Lon. A 253 (1959) 289-295.

[38] G.I. Taylor, Formation of thin flat sheets of water, Proc. R. Soc. Lond. A 259 (1960) 1-17.

[39] R.D. Reitz, F.V. Bracco, Mechanism of breakup of round liquid jets, Gulf Pub, Houston, TX, Country, 1986.

[40] S.A. Krzeckowski, Measurement of liquid droplet disintegration mechanism, Int. J. Multiphase Flow 6 (1980).

[41] M. Pilch, C.A. Erdman, Use of breakup time data and velocity history data to predict the maximum size of stable flagments for acceleration-induced breakup of liquid drops, Int. J. Multiphase Flow 13 (1987) 741-757.

[42] L.P. Hsiang, G.M. Faeth, Near limit drop deformation and secondary breakup, Int. J. Multiphase Flow 19 (1992) 635-652.

[43] P.K. Wu, G.M. Faeth, Aerodynamic effects on primary breakup of turbulent liquids, Atomization Sprays 3 (1993) 265-289.

[44] J.J. Cooper-White, J.E. Fagan, V. Tirtaatmadja, D.R. Lester, D.V. Boger, Drop formation dynamics of constant low viscosity, elastic fluids, J. Non-Newtonian Fluid Mech 106 (2002) 29-59.

[45] H.J. Shore, G.M. Harrison, The effects of added polymers on the formation of drops ejected from a nozzle, Phys. Fluids 17 (2005) 1-7.

[46] R.P. Mun, J.A. Byars, D.V. Boger, The effects of polymer concentration and molecular weight on the breakup of laminar capillary jets, J. Non-Newtonian Fluid Mech 74 (1998) 285-297.

[47] Y. Christani, L.M. Walker, Surface tension driven jet break up of strain-hardening polymer solutions, J. Non-Newtonian Fluid Mech 100 (2001) 9-26.

[48] Y. Christani, L.M. Walker, Effect of fluid relaxation time of dilute polymer solutions on jet breakup due to a forced distrurbance, J. Rheol. 46 (2002) 773-778.

[49] R.P. Mun, B.W. Young, D.V. Boger, Atomization of dilute polymer solutions in agricultural spray nozzles, J. Non-Newtonian Fluid Mech 83 (1999) 163-178.

[50] Z. Liu, R.D. Reitz, An analysis of the distortion and breakup mechanism of high speed liquid drips, Int. J. Multiphase Flow 23 (1997) 631-650.

[51] F.X. Keller, J. Li, A. Vallet, D. Vandromme, S. Zaleski, Direct numerical simulation of interface breakup and atomization. Sixth Int. Conf. Liquid Atomization and Spray Systems, New Youk, 1984.

[52] J. Li, Resolution numerique de l' equation de' navier-stokes avec reconnection d'interfaces: Methode de suivi de volume et application a l'atomization, (PhD), University Pierre et Marie Curie, Paris, 1996.

[53] S. Zaleski, J. Li, S. Succi, Two-demensional navier-stokes simulation of deformation and breakup of liuid patches, Phys. Rev. Lett 75 (1998) 244-247.

[54] A. Merrington, E.G. Richardson, The break up of liquid jets, Proc. Phys. Soc. 59 (1947) 1.

[55] J.B. Kennedy, J. Roberts, Rain ingestion in gas turbine engines. 4th Annual Conference on Instabilities of Liquid Atomization and Spray Systems, Hartford, CT, 1990, pp. 154-162.

[56] C.S. Lee, R.D. Reitz, Effect of liquid properties on the breakup mechanism of high-speed liquid drops, Atomization Sprays 11 (2001) 1-19.

[57] A.R. Hanson, E.G. Domich, H.S. Adam, Shock tube investigation of the break-up of drops by air blast, Phys. Fluids 6 (1963) 1070-1080.

[58] W.G. Reinecke, G.D. Waldman, A study of drop break up behind strong shocks and applications to flight, AVCO Report A VSD-0110, pp. 70 -77, 1970.

Part 2: Application 1: Airborne Bioaerosol Droplets Generation and Control

Chapter 3: Introduction

3.1. Introduction

Infectious respiratory diseases are a prime cause of morbidity, mortality and health system utilization worldwide. Spontaneous coughing is a common symptom for numerous illness and diseases including virus flu, chronic bronchitis, pneumonia, asthma, tuberculosis and many more. The alarming issue is that during coughing a person may generate and exhale hundreds of thousands of bioaerosol droplets which may contain pathogens of various infectious diseases and upon inhalation by others they may transmit the diseases from person to person. Thus, aerosolized secretions from an infected individual, released during coughing, and even during sneezing or talking, represent an important mode of transmission of infection from one person to others.

Our goal in this part of the dissertation, consisting of chapter 3 and 4, is to explore how the aerosolizability of respiratory secretions can be controlled in order to reduce the transmissibility of airborne diseases.

The overall hypothesis is that the transmission of airborne diseases can be controlled by implementing a co-adjuvant pharmacological intervention aimed at

modulating the physical and biochemical characteristics of the respiratory secretions of transmissor who carries the infection, to minimize expelled material that carries the pathogens. This unconventional idea was first conceived by Gustavo Zayas and Malcolm King in 2004 [1] at the University of Alberta. The implementation of the idea is yet to be fully realized through manipulation of mucus viscous and elastic properties using mucolytic therapies. However, the scientific and engineering basis of reducing the aerosolization of breathable particles is still unknown, and needs to be understood before achievement of the targeted goal.

The new knowledge acquired in this part of the dissertation will be useful in understanding the interrelations between the molecular structures and viscoelastic characteristics of human airways surface mucus as well as the effect of viscoelastic properties on the number and size distribution of bioaerosol droplets generated during coughing. These in turn will help improving a new class of drugs being developed at the University of Alberta, aimed at controlling the transmission of airborne epidemic diseases by modifying the viscoelastic response of mucus.

3.2. Production and Composition of Airway Surface Liquid (Periciliary liquid and Mucus)

The airway surface liquid of human respiratory tract consists of two concentric annular layers of fluids with essentially different physical properties: the
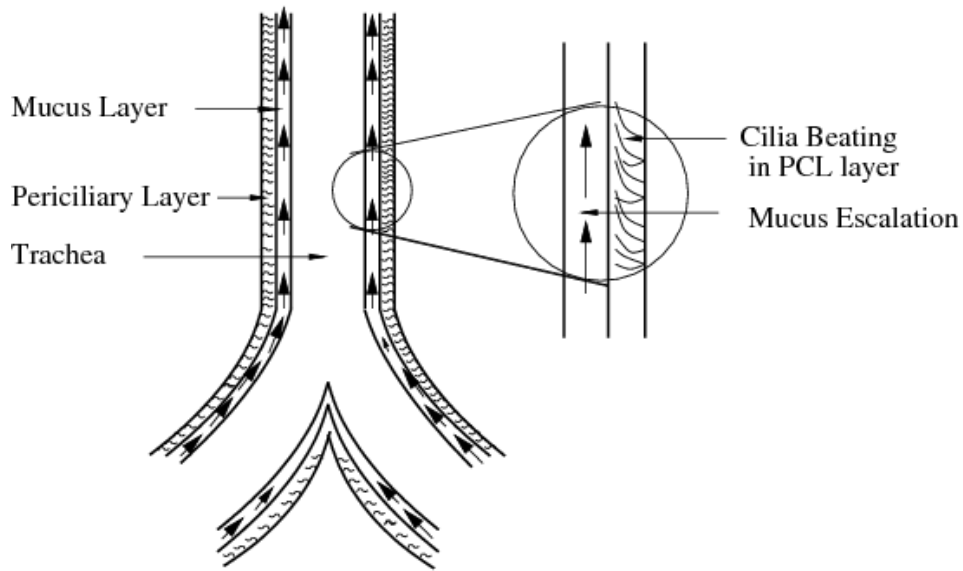
Fig. 3.1. Schematics of the mucus layer and periciliary layer in airway surface liquid in human respiratory tract

periciliary layer (PCL), a watery layer covering the airway epithelium, and the mucus layer, a viscoelastic gel that floats on top of the PCL as shown in Fig. 3.1 [2]. The mucus layer, which is formed by secretions from goblet cells located in the airway epithelium, and also from submucosal glands in the larger airways is a layer of gel-like highly viscoelastic fluid that is transported by the lung clearance mechanism (cilia beating) from the terminal bronchiole to the top of the trachea, where it is swallowed. Mucus usually consists of water and high-molecular weight glycoproteins, mixed with serum and cellular proteins (albumin, immunoglobulins, enzymes) and lipids. It may also contain variable amounts of cell debris and particulate matter. The normal daily volume of respiratory secretion arriving at the larynx is estimated to be approximately 10 ml/day. The total production throughout the airway systems would probably be much higher

47

than that [3]. Usually for total daily production a range of values (5 to 40 ml/day) is adopted by researchers. The velocity of mucus flow in the trachea in an average nonsmoking adult has been measured by marker particle clearance as typically 10-15 mm/min [4]. However, for velocity as well, a wide range of values (5 to 15 mm/min) may occur.

3.3. Molecular Structure of Mucus

The respiratory mucus gel is constituted primarily by a three-dimensional crosslinked network of mucous glycoproteins or mucins which are products of several different genes, some of which are associated with goblet cells while some
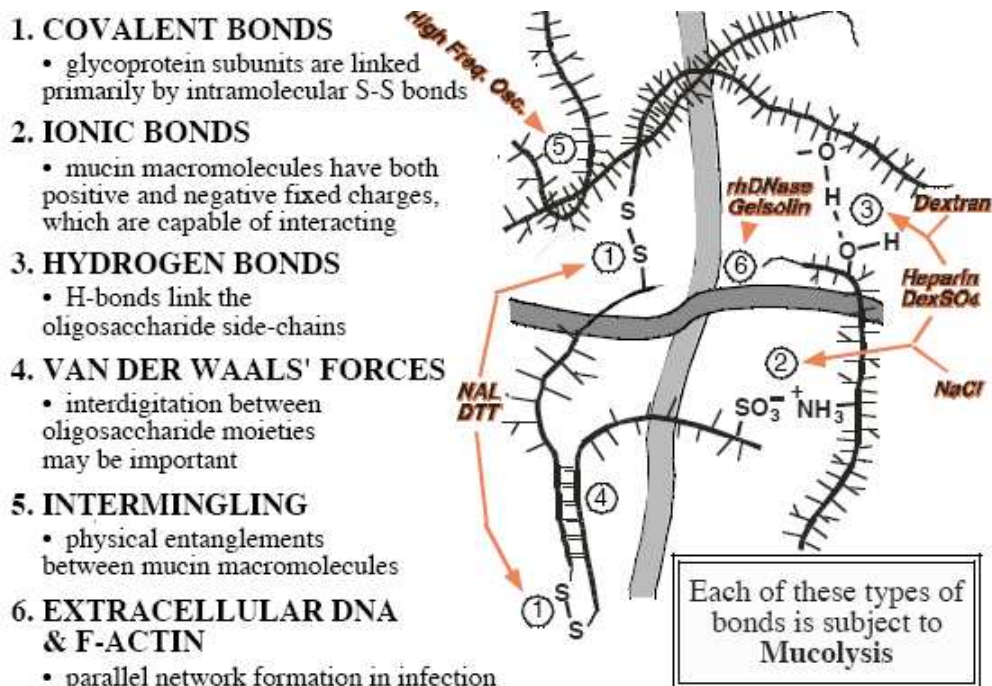
Fig. 3.2. Schematics and brief descriptions of various types of bonds [5] occurring in respiratory airways mucus gel.

may be predominantly glandular. The structure of mucins in the respiratory mucus can be represented as in Figure 3.2 [5]. As shown in Figure 3.2, the three-dimensional structure of mucus consists of a number of different types of bonds, some of which are:

(i)   Di-sulphide covalent bonds

(ii)   Mucin-mucin ionic bonds

(iii)   Hydrogen bonds

(iv)   Van der Walls forces

(v)   Entanglement, and

(vi)   Extra-cellular parallel network formation

Short descriptions of each of the bonds are given in Fig. 3.2.

3. 4. Rheological Properties of Mucus

The rheology of mucus is its capacity to undergo flow and deformation in response to the forces applied to it. The rheological properties of mucus are determined by its content of mucous glycoproteins and water. Due to cross-linking of glycoproteins, the rheological behaviour of mucus is described as viscoelastic, meaning that it has both the characteristics of a viscous liquid and elastic solid [6].

Factors that contribute to the viscoelasticity of mucus include the type of mucus glycoprotein (mucin), the hydration of the secretions, and the degree of entanglement and crosslinking in the mucus gel. Disruption of the gel network (the process known as mucolysis) causes breakage or reduction of the bonds within the mucus gel. If carried out to the right extent mucolysis can optimize the ability of ciliary and airflow mechanisms to clear mucus. Mucolysis can occur in both ways: (i) through physical intervention such as high frequency oscillation [7], and (ii) by using biochemical or pharmacological agents also known as mucotropic agents such as N-acetylcysteine or dornase alpha [8]. Mucolysis, by breaking macromolecular bonds or disrupting secondary bonding in the mucus gel structure, reduces the viscoelasticity of the mucus gel.

The elasticity of a mucus gel is a measure of the density of crosslink points within a given timeframe. At high measurement frequencies or within short times, the effective number of cross-links is greater than for longer times, when the gel network has more opportunity to rearrange in response to the applied stress. The viscosity of the mucus, on the other hand, is a measure of entanglement of the molecules. However, changes in mucus viscosity and elasticity are generally interrelated [9, 10]. Even though interventions that break or add crosslinks can alter the close interrelation between viscosity and elasticity, in most cases of normal scenarios the viscosity will increase with an increase in elasticity and vice versa.

Mucus is a shear thinning fluid meaning that its viscosity decreases with increasing shear rate. The viscosity of mucus, i.e. the resistance to flow, is the major rheological variable that affects cough clearance. Elasticity is involved in terms of the recoil effect. A high degree of elasticity i.e low viscosity to elasticity ratio affects the cough clearance negatively. Adhesivity or the surface tension inhibits cough clearance by suppressing the interaction between the mucus and the airflow. Mucus that is elastic rather than viscous is transported well by ciliary action, but not so well by coughing [11]

3.5. Surface Properties of Mucus

Surface properties of mucus are believed to be important for various mucus functions. Surface tension is caused by the cohesive attraction of molecules to like molecules. Since the molecules on the surface of a liquid are not surrounded by like molecules on all sides, they are more attracted to their neighbors on the surface. The net inward force per unit length on a surface is defined as surface tension.

A layer of surfactant is known to exist at the air-mucus layer interface. The role of this surfactant layer in cough clearance is largely unknown. Effect of surface tension on droplet generation during coughing was studied using instability analysis. Some experimental studies also discussed the surface tension effect on droplet generation during coughing.

3.6. Mucus and Cough Clearance

There are two major mechanisms for clearing mucus from the airways: (i) clearance by coughing and other forms of mucus-airflow interactions (Fig. 3.3), (ii) Clearance by ciliary action. Usually respiratory mucus is cleared by airflow and ciliary interactions. Sputum, which is mucus mixed with inflammatory cells,
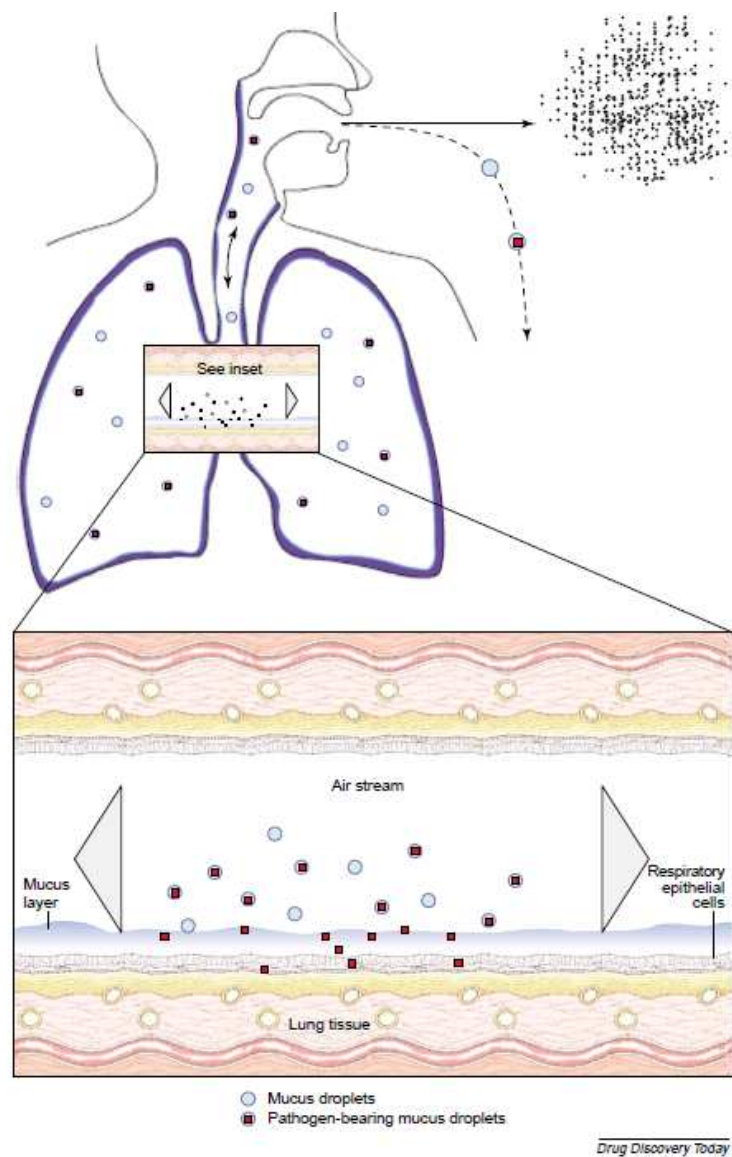
Fig. 3.3. Schematics of mucus clearance through bioaerosol droplets emission from airways during coughing. The figure is reproduced from [12].

cellular debris, and bacteria, is generally cleared by cough. The clearance of airway mucus depends on the biophysical and rheological properties of the mucus gel. These include its internal cohesive properties, viscosity and elasticity, as well as its surface and adhesive characteristics.

Mucus clearance represents the first-line defense mechanism of the respiratory tract, which prevents particles potentially harmful for human lungs such as soot, microbes, allergens and irritants from impinging upon and penetrating the airway epithelium [13]. When production rate of mucus is higher than the rate of clearance, mucus accumulates and obstructs the airways in which case the excess mucus is removed by coughing.

3.7. Mucolytic Therapy

True Mucolytic treatments involve the rupture of polymer backbone elements such as disulfide bridges linking mucin subunits or the breakdown of high-molecular-weight DNA. Having only a few ruptured linkages greatly reduces the resistance of the network to rupture at high strain, even though there is relatively little change in the crosslinks (which determines low-amplitude viscoelasticity). Indirect mucolysis, which involves rearrangements of the macromolecular configuration (e.g. swelling of the network by increasing water content of altering mucin polymer size by changes in ion content), may greatly alter the distance between crosslinks (crosslink density) and yet do little to alter the cohesiveness or rupturability of the gel.

3.8. Study of Mucolytic Therapy through Artificial Cough

The main motive behind the study in the current part of this dissertation is to reduce the human-to-human airborne disease transmission through mucomodulation, i.e. to modulate the physical characteristics of the respiratory secretions to reduce aerosolization without affecting normal mucociliary clearance function. A potential drug, currently called as "Drug Dex" is being developed at the University of Alberta, which is aimed at controlling the transmission of airborne epidemic diseases by modifying the viscoelastic response of mucus. However, in order to achieve this goal, understanding the effect of various mucus properties on the amount and size distribution of bioaerosol droplet generation during coughing is a prime requirement. As one will expect intuitively, the size distribution of droplets generated during coughing would vary from person to person, cough to cough, and even from one instance of time to another during the same cough. Thus a methodical investigation of mucomodulation through study of real human cough is very difficult. Moreover an arbitrary variation of the mucus properties in real human subjects for such investigation would not only be extremely difficult, time consuming and costly, but also it could be life threatening for the subjects under investigation. Simulated cough using mucus simulants in an artificial cough machine, on the other hand, produces size distributions of droplets very similar to those of real human cough in a highly repeatable and safe manner.

The size distributions of droplets generated during a typical human cough measured in our laboratory at different instants of time during a single cough are shown in Fig. 3.4. The figure shows that in the range of 0 to 35 micron diameter
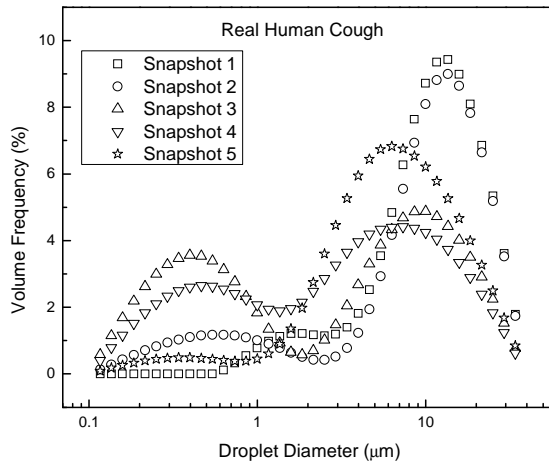
Fig. 3.4. Size distribution of droplets generated from a typical human cough: snapshots at different time instants.
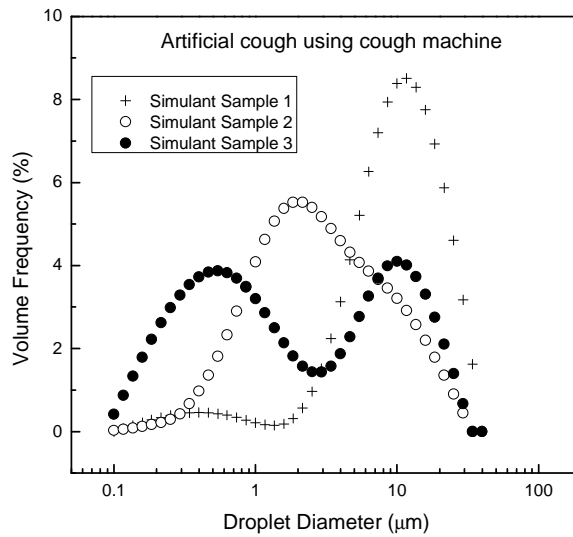
Fig. 3.5. Size distribution of droplets generated from simulated cough for three different mucus simulant samples.

a real human cough produces a bimodal distribution of aerosol droplets. The droplet size distributions presented in Fig. 3.5 obtained for different mucus simulant samples using simulated cough in a cough machine present similar trend in the size distribution as that in Fig. 3.4. In the next chapter the effects of viscoelastic and surface properties of mucus on the characteristics of airborne bioaerosol droplets generated during coughing are, therefore, studied using artificial mucus simulant samples and simulated coughs instead of real human cough. The cough machine is designed to simulate the droplet generation in the tracheal region of the respiratory airways. Because the mucus layer is thickest in this region, the trachea is the primary location of droplet generation during coughing. It is worth mentioning here that an artificial cough is not a perfect replica of the real human cough, as there are certain differences between the two. For example, while the actual human trachea is a non-rigid, ribbed pipe of circular cross section, the model trachea used in the cough machine is a rigid part with a smooth rectangular cross section. However, such simplifications should have little or no effect on the actual mechanisms of droplet generation, which are mainly governed by the fluid and flow properties. The simulated cough using the cough machine is, therefore, a good representative of a real human cough.

References

[1] M. King, Use of charged dextran as a mucoactive agent and methods and pharmaceutical compositions relating thereto. In: U. S. Patents, (Ed., 2004.

[2] M.A. Hasan, C.F. Lange, Estimating in vivo airway surface liquid concentration in trials of inhaled antibiotics, Journal of Aerosol Medicine 20 (2007) 282-293.

[3] W.H. Finlay, Lange, C.F., King, M., and Speert D.P., Lung delivery of aerosolized dextran. , American Journal of Respiratory Critical Care Medicine 161 (2000) 91-97.

[4] A. Wanner, M. Salathe, T.G. O'riorda, Mucociliary clearance in the airways, Am. J. Resp. Crit. Care Med. 154 (1996) 1868-1902.

[5] M. King, Mucolytics and mucus clearance. in: B. K. Rubin, and C. Van Der Schans, (Eds.), Therapy of mucus-clearance disorders. Marcel Dekker, New York, pp. 201-224.2004.

[6] M. King, Experimental models for studying mucociliary clearance, Eur Respir J 11 (1998) 222-228.

[7] B. Dasgupta, M. King, Molecular basis of mucolytic therapy, Canadian Respiratory Journal 2 (1995) 223-230.

[8] B.K. Rubin, R.P. Tomkiewicz, M. King, Mucoactive agents: Old and new. in: R. W. Wilmott, (Ed., The pediatric lung. Birkhäuser Publishing, Basel pp. 155–179.1997.

[9] R.J. Lutz, M. Litt, L.W. Chakrin, Physical-chemical factors in mucus rheology in: H. L. Gabelnick, and M. Litt, (Eds.), Rheology of biological systems. Springfield, IL: Charles C Thomas, , Illinois, pp. 158–194.1973.

[10] M. King, P.T. Macklem, Rheological properties of microliter quantities of normal mucus J Appl Physiol 42 (1977) 797-802.

[11] M. King, Role of mucus viscoelasticity in cough clearance, Biorheology 24 (1987) 589-597.

[12] J. Fiegel, D.A. Edwards, Airborne infectious disease and the suppression of pulmonary bioaerosols, Drug Delivery Today 11 (2006) 51-57.

[13] D.F. Rogers, Overview of airway mucus clearance. in: V. D. S. Rubin B.K, C. P., (Ed., Therapy for mucus-clearance disorders. Mercel Dekker Inc., New York.2004.

<div align="center">**Chapter 4**</div>

<div align="center">**Effect of Artificial Mucus Properties on the Characteristics of Airborne**</div>

<div align="center">**Bioaerosol Droplets Generated During Simulated Coughing**</div>

<div align="center">MD. Anwarul Hasan, Carlos F. Lange, Malcolm L. King</div>

ABSTRACT

The effect of viscoelastic properties and surface tension of artificial mucus simulant samples on the size distribution and volume concentration of bioaerosol droplets generated during simulated coughing was investigated through *in-vitro* experiments. The mucus simulant samples had viscoelastic properties in a similar range as those of real human airway mucus. The mucus simulant gels were prepared by mixing various proportions of 0.5% ~ 1.7% locust bean gum solution and 0.1 M sodium tetraborate (XLB) solution. Surface tension of one set of samples was varied by adding different amounts of SDS (Sodium Dodecyl Sulfate) surfactant while the measurement of surface tension was performed using ADSA (Axi-symmetric Drop Shape Analysis) method. The viscoelastic properties of the samples were measured using a Bohlin Gemini 200 HR (Malvern, UK) nano rheometer with peltier plate assembly. An artificial cough machine was used to simulate human cough, generating aerosol droplets in a model trachea attached to the front of the cough machine. The size distribution and volume concentration of the droplets generated through simulated cough were measured using a laser

diffraction particle sizer (SprayTec, Malvern, USA). The surface tension was found to have negligible effect on the characteristic of generated droplets within the range of this investigation. The experimental results showed a decrease in particle size as the samples changed from a viscous fluid type to a viscoelastic to an elastic solid type sample. The volume concentration also changed significantly as the viscoelasticity of the samples was varied.

Keywords: Bioaerosol droplets, Mucus, Viscoelasticity, Surface Tension, Cough machine.

4.1. Introduction

Bioaerosol droplets exhaled by humans during breathing, sneezing and coughing may carry airborne pathogens, which upon inhalation by others spread various infectious diseases, such as influenza, measles, swine flu, chickenpox, smallpox, SARS and so on. Such airborne transmission of respiratory infections through bioaerosol droplets poses a major public health threat and it is a subject about which surprisingly very little is known. Recent theoretical studies [1] support the hypothesis that the number and size distribution of the bioaerosol droplets generated during coughing can be controlled by altering the viscoelastic and surface properties of the airway surface liquid. The unconventional idea of controlling the transmission of airborne diseases by modulating the physical and

biochemical characteristics of the respiratory secretions of a transmissor who carries the infection was first conceived by Malcolm King and Gustavo Zayas in 2004 [2] at the University of Alberta. However, since the details about the correlations between the viscoelastic and surface properties of mucus and the characteristics of the generated bioaerosol droplets are largely unknown, the implementation of the idea is yet to be fully realized. In order to mitigate the airborne transmission and to control the generation of bioaerosol droplets during coughing, sneezing etc., it is important to understand the correlations between the relevant viscoelastic and surface properties of mucus with the volume concentration and size distribution of the generated droplets. In this work we have studied the effect of surface tension and viscoelastic properties of artificial mucus simulants on the size distribution of bioaerosol droplets generated during simulated coughing.

4.1.1. State of the art knowledge about coughing and bioaerosols

A cough can generate several thousand [3] to about a tenth of a million droplets [4], while a sneeze can generate as many as forty thousand [5] to close to two million droplets [4] at a velocity of up to 100 m/s. Many of the generated droplets may be large enough to contain thousands of microorganisms [6]. During the expulsion, the diameters of the droplets vary between fractions of a micron and 2,000 μm, the majority of which are in the order less than 100 μm. Moreover, the droplets dry very rapidly. The drying times for 100 and 50 μm droplets in air at

50% relative humidity are 1.3 and 0.3 seconds, respectively [7]. On complete evaporation, the particles may be small enough to remain airborne in the indoor air flow.

The sizes of pathogenic microorganisms, on the other hand, span wide ranges e.g. from 0.3 to 15 μm for bacterial cells and spores, 2.0 to 5.0 μm for fungal spores, 0.02 to 0.30 μm for viruses, and 1 to 50 μm for the majority of molds and yeasts [6,8-12].

Depending on aerosolized droplet size, airborne pathogens can quickly deposit on nearby external surfaces or the expired bioaerosols can travel great distances and remain airborne for an extended time, particularly when droplets are too large for diffusive deposition (>200 nm) or too small for gravitational deposition (<2 μm) [13,14]. Bioaerosols consisting of solid or liquid particles smaller than 10 μm can remain suspended in the air for a few hours and are likely to be inhaled [6,12,15]. Table 4.1 lists the time required for a droplet to deposit by sedimentation from a height of three meters [12].

Table 4.1 Behavior of bioaerosols in the air [12]

Diameter in micron	Time required for deposition from a height of 3 meters
100	10 sec
40	1 min
20	4 min
10	17 min
6 to 10	A few hours
0.06 to 6	Several hours

4.1.2. Historical perspective on bioaerosol research

To date, few studies have carefully examined the nature of the bioaerosols that humans exhale on a daily basis. Early researchers assumed the upper respiratory tract (nose, mouth and throat) to be the primary location of droplet formation [16,17,18]. In these early studies, the mouths and throats of volunteers were coated with a dye and breathing, talking, sneezing and coughing maneuvers were monitored and any resulting droplets were collected directly onto a slide. Only droplets >1 μm were measured by microscopic observation. Duguid [16] found that droplets (>1 μm) produced by speaking, coughing and sneezing were sufficiently small to remain airborne. Normal breathing, however, produced no measurable droplets (>1 μm). In a second series of experiments [17], Duguid determined that coughing produced an average droplet size of geometric mean (GM) = 14 μm and geometric standard deviation (GSD) = 2.6 and for sneezing GM = 8.1 μm and GSD = 2.3. On the other hand, Loudon and Roberts [18] showed that the estimated log-normal parameters were GM = 12 μm and GSD = 8.4 for cough. More recently, Papineni and Rosenthal [19] measured expired bioaerosol droplets (in nose and mouth breathing, coughing and talking) to be <2 μm in size, with no droplets >8 μm. An interesting common finding from these studies was the high variability in the levels of bioaerosol production from different individuals.

More recent experiments have utilized optical particle counting (OPC) to determine the size and concentration of droplets exhaled from all parts of the

respiratory tract [19-21]. In a similar experiment to that of Papineni and Rosenthal, Edwards et al. [20] observed 11 healthy human subjects. Results from this study confirmed Papineni and Rosenthal's findings as they suggested that the exhaled particles during normal mouth breathing are predominantly <1 μm in diameter. Edwards' results also showed that expired particle numbers vary substantially from subject to subject, with two distinct populations: low producers (those exhaling an average of <500 droplets per liter over a six hour measurement period) and super producers (those exhaling an average of >500 droplets per liter over a six hour measurement period) of expired bioaerosols. Remarkably, the super producers (six people from the test group of eleven) expired 99% of the total amount of bioaerosols that were expired by the entire group.

In their study, Edwards *et al*. [20] further found that delivering ~1 g of isotonic saline (orally via nebulized aerosols, 5.6 μm in diameter) reduces the total amount of expired aerosols (among the super-producing individuals) by ~72% over a six hour period and markedly diminishes total expired bioaerosol production for the entire group. *In vitro* results, obtained using a simulated cough machine, also indicated that a mucus mimetic nebulized with saline produces a larger droplet size after the forced convection of air over its surface than when air is forced over the mucus mimetic alone (i.e. without saline nebulization). These results led Edwards and co-workers to speculate that saline delivered onto lung surfactant increases its surface tension, and potentially other dynamic physical properties of the lung surfactant, thereby changing the droplet breakup dynamics. In a

subsequent study, Clarke *et al.* [22] report that delivering isotonic saline aerosols (in 5.6 μm droplets) into the endotracheal tube of anesthetized bull calves showed a dose-responsive effect on exhaled bioaerosols; six minutes of treatment resulted in a decrease ≤50% of exhaled bioaerosols for at least 120 minutes, compared with pre-treatment.

The idea of inhaling saline for medical benefit has existed since the time of Hippocrates. However, the mechanism of this phenomenon remains unclear, as does the reason for the dramatic exhaled aerosol differences among human individuals. In explaining why certain individuals in Edward's study breathe out many more bioaerosol particles than do others, Watanabe et al. [23] suggested that possibly transient and/or durable inter-subject variations in the ionic composition of airways surface liquid produce the inter-subject variations in the number of expired bioaerosol particles, and potentially in airborne disease infectiousness. They speculated that the gelation of the free surface of airways surface liquid mimetic owing to deposition of salt-based solutions should diminish the propensity of the airways surface liquid to break up into droplets in the cough machine.

4.1.3. Pulmonary bioaerosol droplet generation and breakup

The interaction of the mucus layer with the pulmonary airflow plays a major role in lung clearance. Several studies have focused on the effects of wave formation

on shearing of the mucus blanket [24] but the interaction of the mucus layer with pulmonary airflow is not yet fully understood. Clarke et al. [25], King et al. [26], Evrensel et al. [27] and others have reported that when a critical flow velocity is reached, either propagating or standing waves suddenly appear on the compliant layer surface in simulated airways. Experiments [26,28-31] also revealed that these well organized surface waves suddenly appear when a critical velocity is reached, indicating that the instability mechanism is responsible for the generations of these waves rather than the random turbulent fluctuations [32,33]. Linear wave instability theory applied to the coupled air-mucus system predicted that the onset flow speed at which the waves initiate is sensitive to the ratio of mucus viscosity to elasticity [24]. The model of Evrensel et al. [34, 35] predicts that instability initiates in the form of fast propagating waves for mucus with negligible viscosity, while very slow propagating waves form if the mucus is highly viscous. Vasudevan and Lange performed Rayleigh-Taylor type instability analysis on a suitably chosen model of viscoelastic fluid to investigate temporal instabilities and their relation to the fluid properties [1,41]. Their studies indicated that a decrease in modulus of elasticity and surface tension and increase in viscosity are expected to result in droplet size enlargement, while lowering the viscosity and increasing elasticity and surface tension may help in suppression of droplet generation during coughing. They further commented, if full suppression is not achieved, in the latter case, the generated droplets may be smaller and more dangerous.

The current study investigates the effects of mucus properties on the bioaerosol droplets formation over a large range of values of viscoelastic properties and surface tension.

4.2. Experimental

4.2.1 Materials and sample preparation

Mucus simulant gels having similar viscoelastic properties to real human airway mucus [26] over a wide range were used. The gels were prepared by mixing various proportions of 0.5% to 1.7% locust bean gum (LBG) solution and 0.1 M sodium tetraborate (XLB) solution. For preparation of locust bean gum solution, 100 ml of saline (Na_2NO_3) solution was heated to 80 ^{0}C. The required amount of LBG powder was added to the saline solution little by little while the solution continuously being stirred using a magnetic stirrer. The weight of the beaker with the saline solution was measured both before and after heating and mixing LBG powder. Mass balance was ensured by adding additional saline solution to compensate the losses due to evaporation whenever necessary. Compositions of locust bean gum solution used in the experiments ranged from 0.5% to 1.7%. Volumes of 0, 10, 15, 20, 30, 45, 60 and 90 µl of 0.1 M tetraborate solution were added to 1.5 ml of locust bean gum solution, the resulting concentrations of tetraborate in the locust bean gum being 0, 6.67, 10, 13.33, 20,

30, 40 and 60 µl/ml. The mixture was then vortexed for 2 minutes on a vortex mixer.

Surface Tension of the samples was varied by mixing different amounts, 2mM, 4mM and 6mM, of SDS (Sodium Dodecyl Sulfate) surfactant in the saline solution before adding the LBG powder.

4.2.2. Measurement of viscoelastic properties

Viscoelastic properties of the samples were measured using a Bohlin Gemini HR 200 Nano-Rheometer (Malvern, UK) with a peltier plate assembly and parallel plate geometry. The frequency of the oscillation was varied between 0.01 Hz and 10 Hz. All measurements were performed at constant strain within the linear viscoelastic region, i.e. within the limit of shear stress where viscosity is independent of applied shear stress. This region was obtained for each sample by performing an amplitude sweep test before the actual measurement of viscoelastic properties. The temperature was kept constant at 25 ^{o}C. A solvent trap was used to avoid drying out of the samples during measurement.

4.2.3. Measurement of surface tension

Surface tension was measured using a custom built apparatus based on the pendant drop analysis method. The machine is composed of an inverted 250 μl 'Gastight' syringe (Hamilton Co.) with a stainless steel blunted needle attached to the end and mounted to a syringe pump. The syringe is filled with the liquid/solution to be tested, and the pump drives the liquid out until it hangs from

the end of the needle but is deformed by gravity (as a tear-drop instead of a spherical shape). The drop is held in this position and imaged by a CCD camera (the drop is back-lit). The drop images are edge fitted and each resulting edge is used to solve the Laplace equation using the technique of Axisymmetric Drop Shape Analysis (ADSA) with the assumption that the drop is axisymmetric about the vertical. Each drop was held for about 30 s, with ~30 images taken of the drop at 1 second intervals. The process was repeated, to give 3 separate drops with ~30 data points taken for each. Results from the three measurements were averaged to obtain the final surface tension values.

4.2.4. Cough machine experiment

The artificial cough machine comprised of an 8-liter Plexiglas tank equipped with a Wilmot Castle pressure gauge. The gas release was controlled by an Asco solenoid valve located at the start of the outflow line. A model trachea 35 cm long with an interior width of 2.0 cm and an interior height of 1.0 cm was attached to the outlet after the solenoid valve. A small rectangular slot 3 cm long by 1.76 cm wide and 1 mm deep was engraved on the upper surface of the bottom plate of the model trachea to hold the mucus simulant sample in place. The slot size was sufficiently large to hold a 1.5 ml sample. The model trachea had a simplified (90° bent) model throat of 8.5 mm diameter attached at its other end based on the prototype by Zhang el al. [37]. The purpose of the model throat was to filter out larger droplets. The Spraytec device has a measurement range from 0.1 µm to 900 µm. It was observed that if any droplet larger than 900 µm were to

pass through the laser beam during a measurement, the instrument could generate unrealistic size distribution data. Use of the model throat was to ensure that very large droplets would hit the wall of the throat and be prevented from passing through the laser beam, while the smaller droplets could follow the flow and proceed through the laser beam where their size could be measured.

Cough machine experiments were performed to mimic bioaerosol generation during a human cough. Mucus simulant samples were placed inside the trachea at the sample slot and a normal adult cough was simulated by suddenly releasing the air from the tank stored at a pre-selected pressure.

Usually a pressure of 8.5 psi is considered as the effective pressure relevant to a typical standard human cough; however, in reality the air pressure may vary depending on whether a cough is a strong cough or a weak cough. The simulated cough data was, therefore, obtained over a range of pressures, namely 4 psi, 6 psi, 8.5 psi and 11.5 psi.

4.2.5. Measurement of droplet size distribution

The size distribution of the droplets was measured using a laser diffraction based particle sizer: Spraytec (Malvern, UK). In our case, the droplets generated from the cough machine were passed through the laser beam which was a 632.8 nm, 5 mW helium-neon laser of about 1 cm diameter. The droplets scatter the light, smaller droplets scattering the light at larger angles than bigger droplets.

The scattered light is measured by a series of photodetectors placed at different angles (36 element log-spaced silicon diode detector array). This is known as the diffraction pattern for the sample. The diffraction pattern is used in the software for calculating the size of the droplets using the Mie theory of light scattering. The Spraytec is capable of measuring a size range of 0.1 – 2000 µm using two lenses, which is a uniquely wide range for this type of particle sizer. In the current study, all measurements were performed using a 300 mm lens, which covers a measurement range of 0.1 - 900 µm. The laser diffraction signal is sensitive to the volume of the droplets. For this reason, droplet diameters are calculated from the measured volume of the droplets, assuming a sphere of equivalent volume.

All measurements were preformed using a rapid data acquisition rate of 2.5 KHz over a time period of 500 ms (100 ms before the triggering and 400 ms after the triggering). The time of 500 ms was chosen because a real human cough is typically biphasic with an initial high-flow rate phase of ≈12 l/s and a duration of ≈ 30-50 ms followed by a second phase of diminishing flow rate lasting ≈ 200-500 ms. The simulated cough also has a similar biphasic profile over ≈ 500 ms [20]. Measurement triggering was set based on signal transmission drop to a level of 99%. The scattering signals recorded by the detectors over 500 ms time span were averaged. Even though the measurements covered a range of 0.1 to 900 µm, our focus was only on smaller droplets. The reason for this focus on the smaller droplets is they are considered more dangerous, since they can remain airborne for up to several hours depending on their size, as shown in Table 4.1, and pose

71

greater risk in terms of disease transmission. Table 4.1 shows that droplets larger than 40 µm diameter, in general, land on nearby surfaces due to gravitational sedimentation in a less than a minute, posing minimal risk to disease transmission. To focus on the small size droplets only, the detectors range was set from 25th to 36th, chopping off the larger droplets data recorded by detectors 1 to 24. This allowed us to narrow down the analysis to the 0.1 to 35 µm size range.

4.3. Results and Discussion

4.3.1. Viscoelastic properties of mucus simulant samples
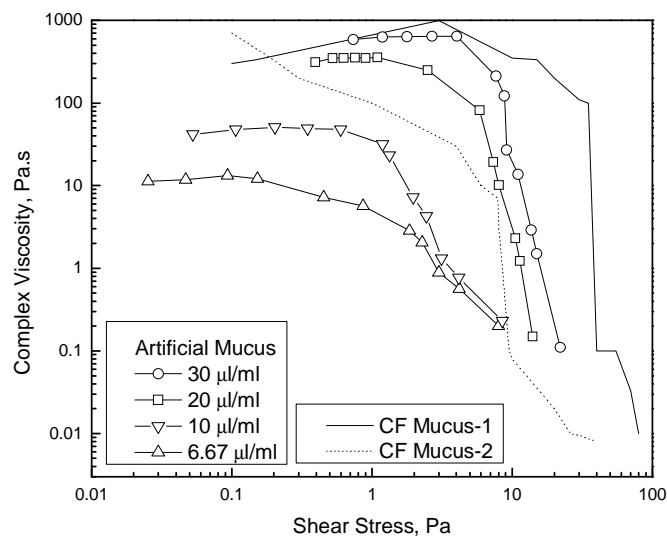
Fig. 4.1. Comparison of rheological properties of some artificial mucus simulant samples (LBG concentration = 1%) with the literature data [38] for real human respiratory airways mucus.

The complex viscosity versus shear stress data for real human mucus of two cystic fibrosis patients obtained from the reference Shah et al. [38] are plotted in Fig. 4.1. The complex viscosities of some representative mucus simulant samples used in this study (1% LBG) are also plotted in Fig. 4.1. The stress values in Fig. 4.1 represent the amplitudes of the oscillatory stress signals. It is evident from Fig. 4.1 that the mucus simulant samples used in this study were reasonably good representatives of real human mucus samples. The viscous modulus versus frequency graphs for different amounts of cross linking in 0.5% LBG mucus simulant samples are shown in Fig. 4.2, while the elastic modulus versus frequency graphs for different amount of cross linking for 0.5% LBG mucus
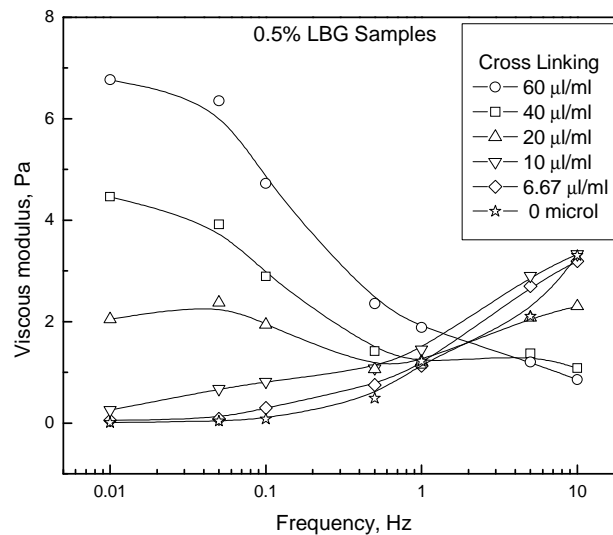
Fig. 4.2. Variation of viscous modulus of 0.5% (LBG) concentration mucus simulant samples with frequency of oscillation.

73
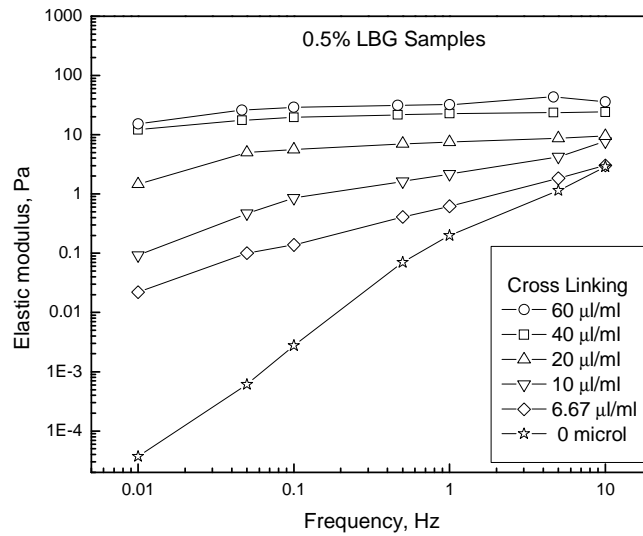
Fig. 4.3. Variation of elastic modulus of 0.5% (LBG) concentration mucus simulant samples with frequency of oscillation.

simulant samples are shown in Fig. 4.3. The figures reveal that, while the change in elastic modulus with the amount of cross linking follows a consistent trend for all samples at all frequencies, the change in viscous modulus with increase in cross linking shows different trend at different frequencies (i.e. at different shear rate). Even though at low frequencies (≤ 0.1 Hz) the change in viscous modulus with increase in cross linking is considerably high, at moderate to high frequencies (≥ 0.5 Hz), which are more likely relevant to coughing, changes in viscous modulus with increase in cross linking are not significant. The elastic modulus of the samples, on the other hand increases continuously by up to several orders of magnitude at low frequencies and up to one order of magnitude at high

74
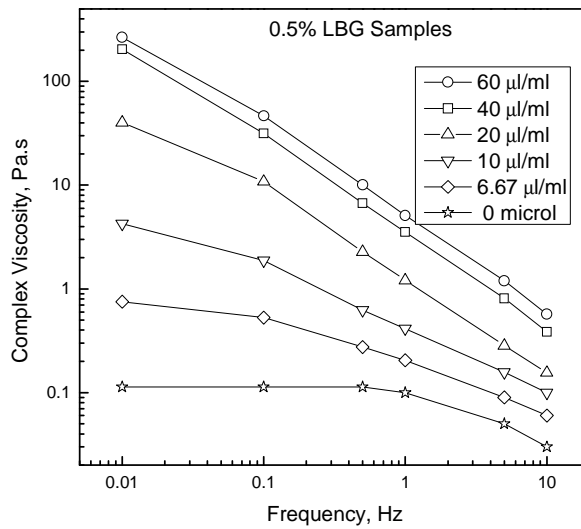
Fig. 4.4. Variation of complex viscosity of 0.5% (LBG) concentration mucus simulant samples with frequency of oscillation.

frequencies as shown in Fig. 4.3. Thus characterizing the rheological behavior of these samples in terms of viscous and elastic modulus separately will not be very helpful for the purpose of this analysis.

Fig. 4.4 presents the complex viscosity of the samples against frequency. The shear thinning behavior is evident in Fig. 4.4, in addition to the fact that the complex viscosity increases with increase in cross linking at all frequencies. Fig. 4.5 reports the phase angle of the samples against frequency. As expected due to the non-Newtonian behavior, the phase angle values are different at different shear rates for the same samples. Since the variations of both complex viscosity

75
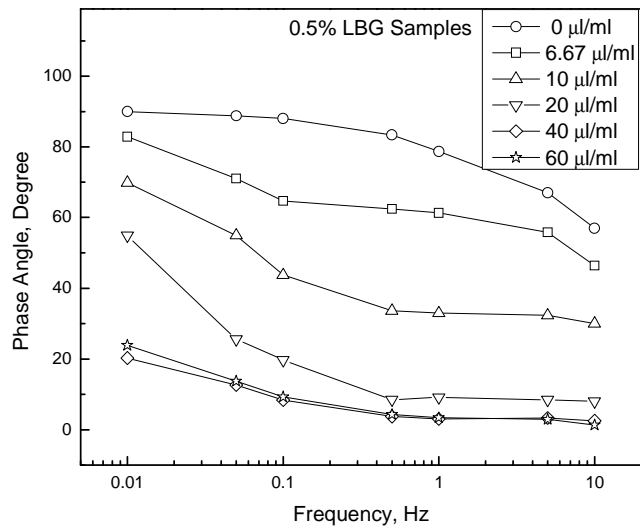
Fig. 4.5. Variation of phase angle of 0.5% (LBG) concentration mucus simulant samples with frequency of oscillation.

and phase angle are consistent with frequency for all cross linking and are also consistent with the increase of cross linking at all frequencies, the complex viscosity and phase angle will be used as characterizing parameters for the viscoelastic behavior of the samples throughout this work.

It is worth mentioning here that a zero degree phase angle indicates a pure elastic (solid) material, a ninety degree value of phase angle indicates a purely viscous (Newtonian fluid) material, while the values between zero and ninety indicate that the sample has both viscous and elastic properties. For the sake of convenience, based on the phase angle at a particular shear rate, we can thus classify all

Table 4.2 Surface Tension of 0.5% LBG samples with 0 to 6 mM SDS (Sodium

Dodecyle Sulfate)

SDS (Surfactant) (mM)	Surface Tension (dyne/cm)
0	54.85
2	34.29
4	31.00
6	30.22

samples into (i) elastic solid-like samples (0 to <30 degree), (ii) strongly viscoelastic samples (30 to 60 degree), and (iii) viscous liquid-like samples (60 to 90 degree). The thresholds of 30 and 60 are broad and meant only to help organize and interpret the results of this study. A simulated cough is considered to be a high shear rate phenomenon as is considered a real human cough. However, since the actual value of the shear rate that governs the droplet generation is unknown, we will subsequently report the properties at three different frequencies, namely 0.01 Hz, 1 Hz and 10 Hz.

4.3.2. Surface tension and its effects on the size distribution and volume concentration

The surface tension of 0.5% LBG samples with 0 mM, 2 mM, 4 mM and 6 mM sodium dodecyl sulfate (SDS) are shown in Table 4.2, while the size distribution of the generated droplets are plotted in Fig. 4.6. As is evident from Fig. 4.6, variation of surface tension in the range 30 to 55 dyne/cm did not show any change in the droplet size distribution and/or volume concentration of droplets. While some may find this result surprising, there are other works in the literature
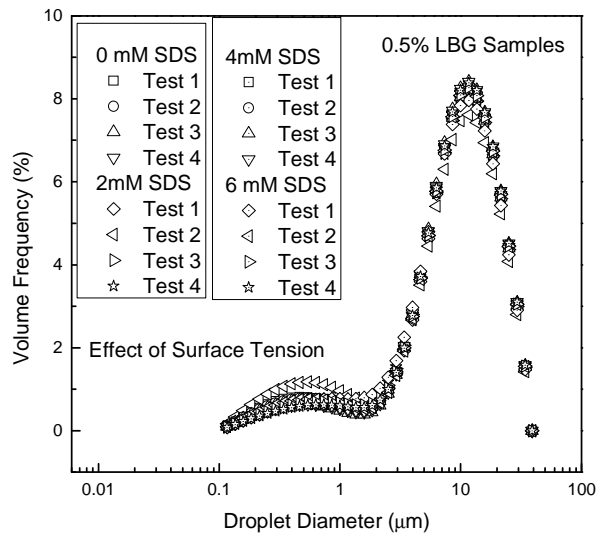
Fig. 4.6. Effect of surface tension during simulated coughing on the size distribution of generated droplets.
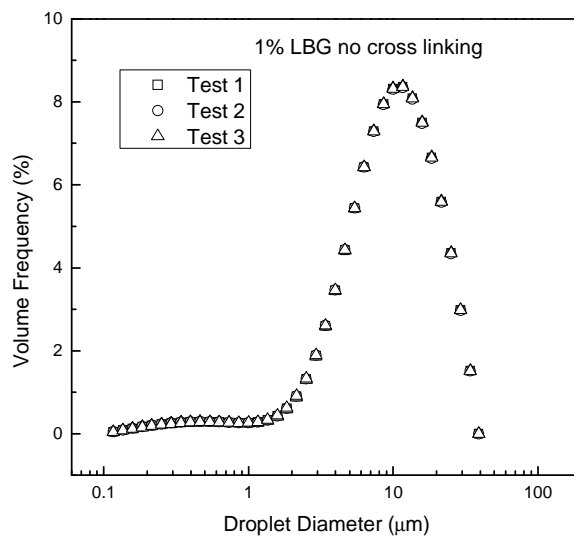
(a)
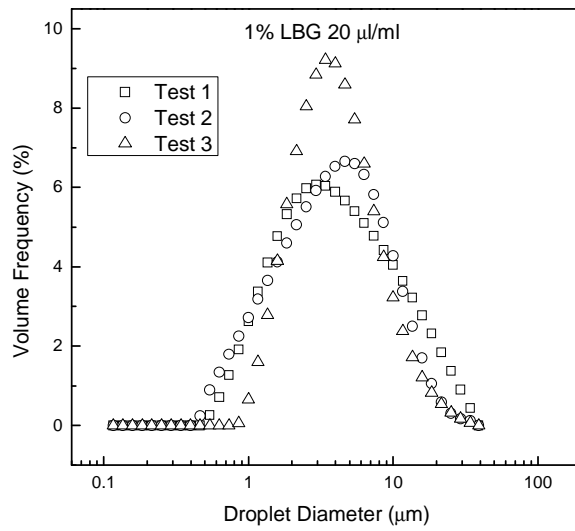
(b)
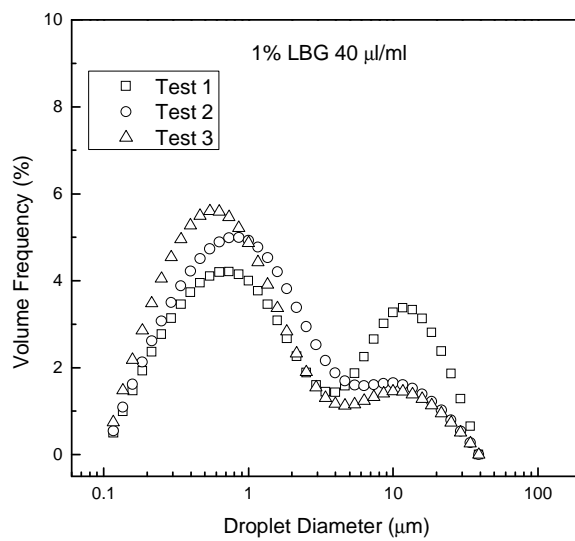
(c)

Fig. 4.7. Volume frequency versus droplets diameter of 1.0% (LBG) concentration mucus simulant samples with cross linking: (a) 0 µl/ml, (b) 20 µl/ml, (c) 40 µl/ml.

that also report zero surface tension effect on droplet size distribution. Lasheras et al. [39], e.g., suggested that surface tension does not have any effect on the interfacial instability of a jet when the Weber number is large. If we assume an air velocity, $v = 22$ m/s (50 mph), air density, $\rho = 1.2$ kg/m^3, the characteristic length, $l = 2$ cm, and a surface tension value of, $\sigma = 30$ mN/m, the Weber Number ($We=\rho v^2 l/\sigma$) for coughing becomes 387. This value is too large for the Weber number to have an effect on droplet breakup, as mentioned by Lasheras et al. [39,40]. Our result, thus, shows that surface tension has negligible effect on the size distribution of droplets generated during coughing. It is worth mentioning though that the surface tension values reported in the current study were all static surface tension. Whether or not the effect of dynamic surface tension on the droplet size distribution and number concentration would be similar has not been addressed in the current work.

4.3.3. Effect of viscoelastic properties on the size distribution

The volumetric size distributions of the droplets in the range 0.1 to 35 µm generated during simulated cough experiments for addition of tetraborate solution at ratios of 0, 20, and 40 µl/ml in 1.0% concentration LBG samples are presented in Figs. 4.7 (a), (b), and (c), respectively. Each figure presents results for three repeated test runs for one sample. Other samples showed even less variation between samples. As mentioned earlier, our focus in this study has been on the small size droplets. Therefore, all size distribution data presented subsequently are in the range 0.1 to 35 µm. Figs. 4.7 (a) to (c) confirm that the viscoelastic
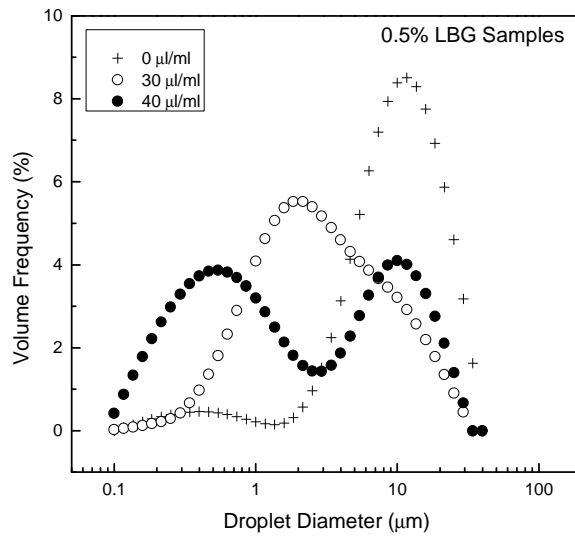
(a)
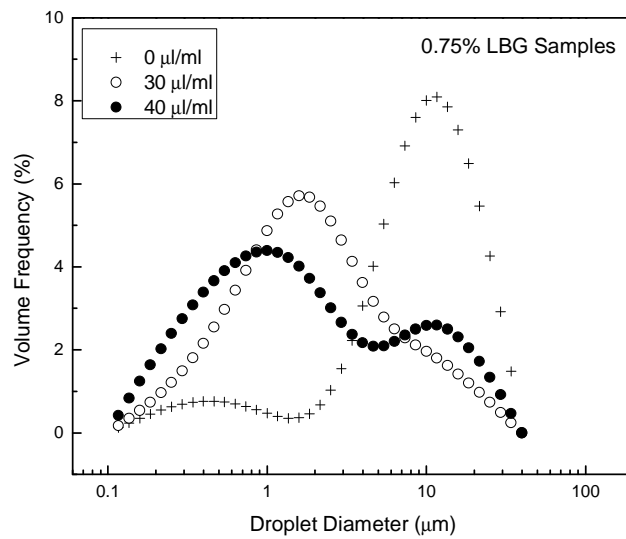
(b)

properties of mucus have a substantial effect on the size distribution of droplets generated during coughing. Three distinct types of droplet size distribution are

81
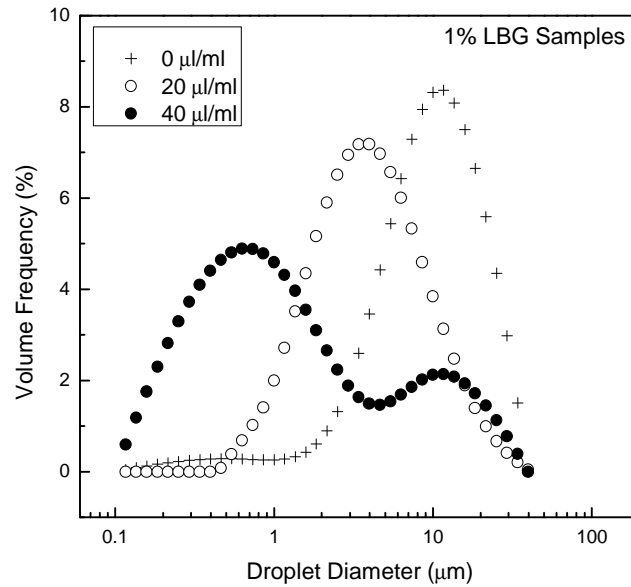
(c)

Fig. 4.8. Average volume frequency versus droplets size distribution graphs for concentrations (a) 0.5% (b) 0.75%, and (c) 1% (LBG) mucus simulant samples.

apparent within this range in Figs. 4.7 (a) to (c). While the viscous fluid-like samples, Fig. 4.6 and Fig. 4.7(a), show a bimodal droplet size distribution with a smaller peak at around 0.4 micron and a larger peak at around 10 µm, the viscoelastic-type samples, Fig. 4.7(b), show a single mode of size distribution. The smaller peak in the submicron size range apparent for the viscous liquid-like sample is no longer apparent for strongly viscoelastic samples. For elastic solid-type samples, Fig. 4.7(c), the size distributions are again a bimodal distribution, with a much stronger peak at a relatively smaller size.
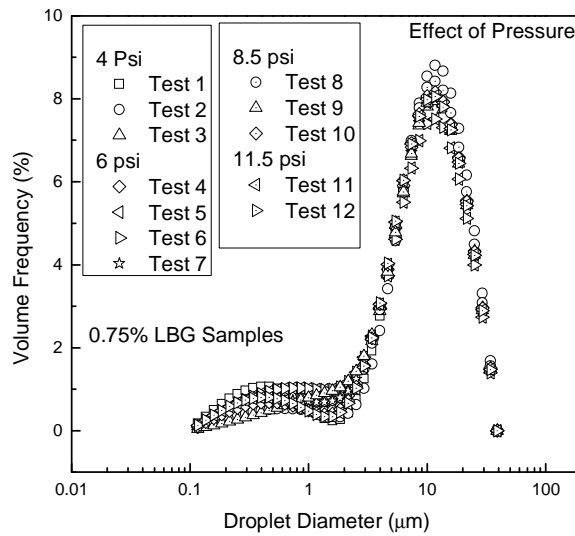
Fig. 4.9. Effect of air pressure during simulated coughing on the size distribution of generated droplets.

The variation of average size distribution with cross linking for 0.5%, 0.75% and 1% concentration samples are summarized in Figs. 4.8 (a), (b) and (c), respectively. It is evident from Figs. 4.8 (a) to (c) that the dominant peak in the size distribution of the droplets apparently shifts toward smaller size as the sample changes from a viscous fluid-like sample to a viscoelastic sample to an elastic solid-like sample (large amount of cross linking). This result is in agreement with the prediction of Vasudevan and Lange [41] based on instability analysis. The size distribution data presented in Figs. 4.7 and 8 were all obtained at an air pressure of 8.5 psi in the simulated coughing experiments. Fig. 4.9 presents the size distribution of 0.75% LBG sample with no additional cross linking, at different
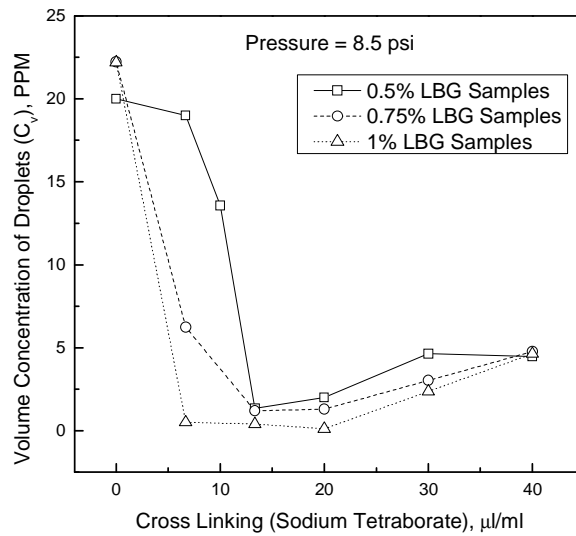
Fig. 4.10. Variation of the volume concentration of droplets generated during simulated coughing with the variation of cross linking at 8.5 psi pressure.

pressures. The size distribution at all physiologically relevant pressures was similar, i.e. the pressure seemed to have negligible effect on the size distribution of droplets generated during coughing.

4.3.4. Effect of viscoelastic properties on the volume concentration/number of droplets

Fig. 4.10 reports the volume concentration of droplets versus the cross linking for 0.5%, 0.75% and 1% LBG samples at 8.5 psi pressure. The figure clearly shows that the volume concentration of emitted droplets for samples at all LBG concentrations follow a consistent trend, i.e. as the cross linking increases the

84

volume concentration decreases until it reaches a minimum of zero, where there is

no measurable amount of droplets. If the cross linking continues to increase the

volume concentration of droplets increases again and approaches an asymptotic

value much smaller compared to the high volume concentrations at zero cross

linking. As mentioned earlier, an increase in cross linking increases the elasticity.

However, the viscous properties are affected at the same time causing the results

to follow different apparent curves. The complex viscosity accounts for both

elastic and viscous properties, and it increases consistently with an increase in the

amount of cross linking. The increase in complex viscosity of samples with

different concentrations for the same amount of cross linking is not the same. For

example at 0.01 Hz, 0.5% LBG sample with a cross linking of 10 µl/ml has a

complex viscosity of 4.26 Pa.s as shown in Fig. 4.4, while that for 0.75% LBG
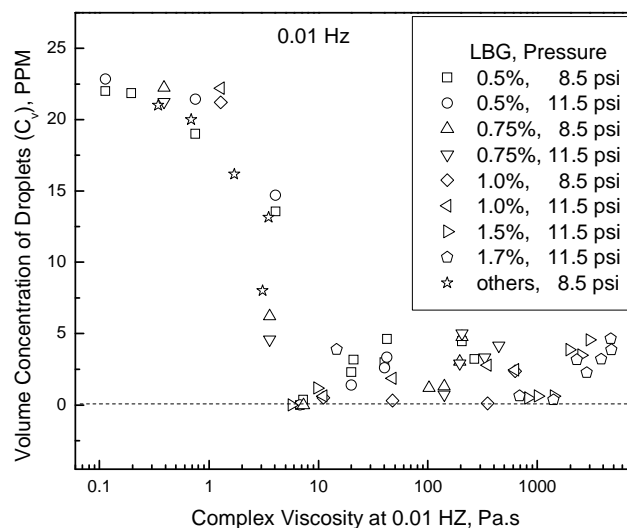
(a)
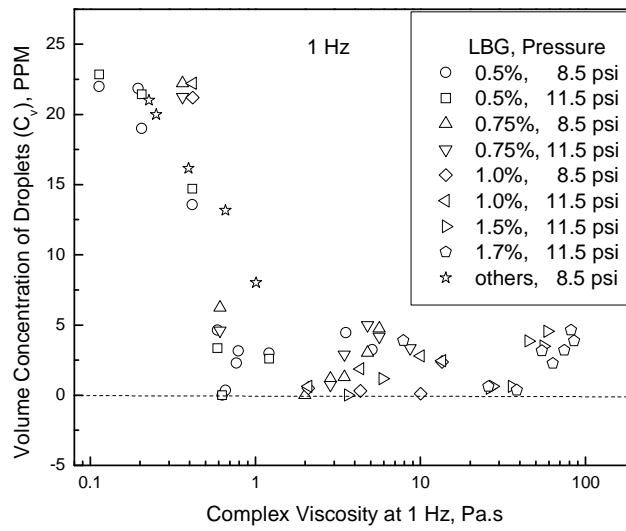
(b)
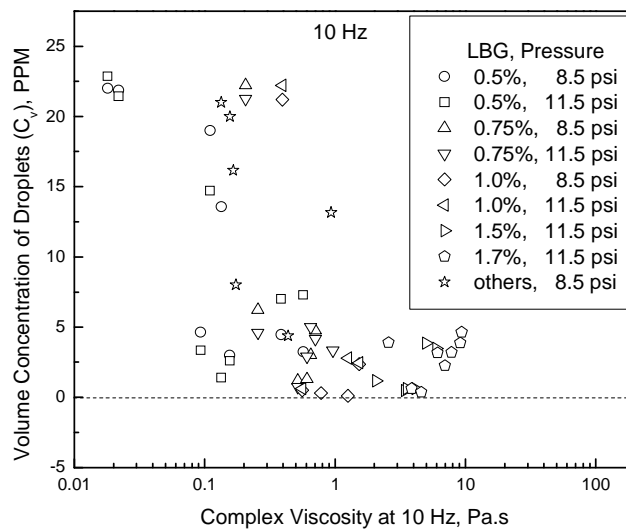
(c)

Fig. 4.11. Volume concentration versus complex viscosity graphs of all samples presented at (a) 0.01 Hz, (b) 1 Hz and (c) 10 Hz frequencies.

sample with 10 µl/ml cross linking is 102.78 Pa.s. If the emitted volume

concentrations of the samples are plotted against complex viscosity as shown in

(a)

(b)
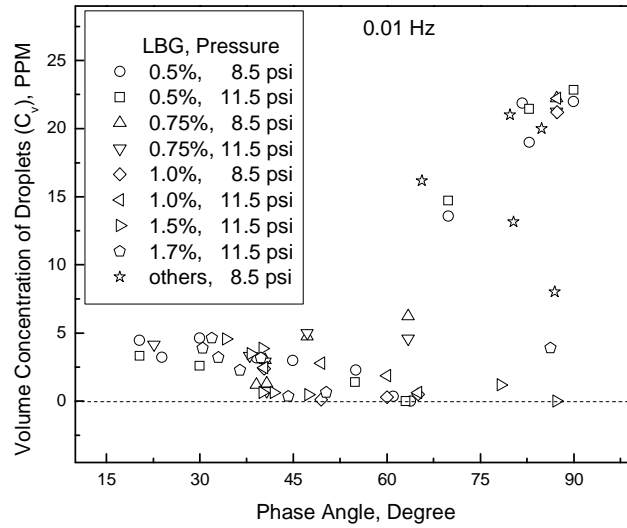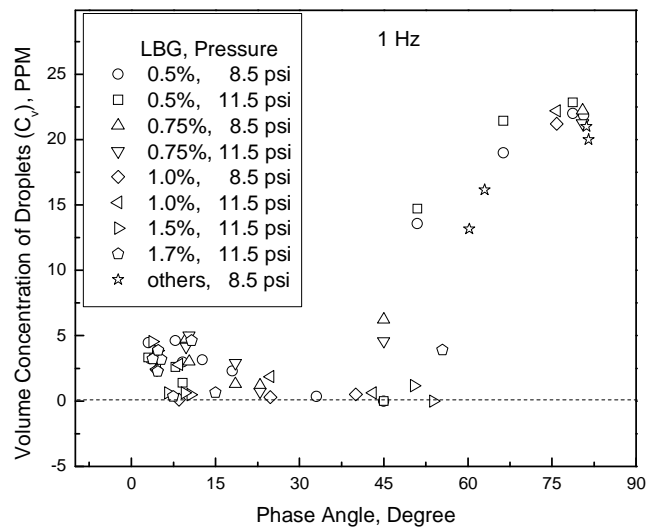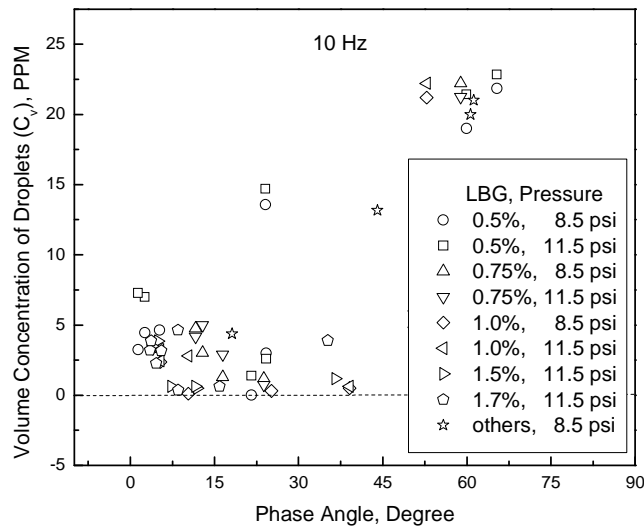
Fig. 4.12. Volume concentration versus phase angle graphs of all samples presented at (a) 0.01 Hz, (b) 1 Hz and (c) 10 Hz frequencies.

Figs. 4.11 (a), (b) and (c), the data obtained at different pressures and different amount of cross linking at all concentrations fall mostly on a single curve. Figs. 4.11 (a), (b) and (c) present the volume concentration of emitted droplets versus complex viscosity at 0.01 Hz, 1 Hz and 10 Hz frequencies, respectively. Figs. 4.12 (a), (b) and (c) report the same volume concentration data against the phase angle of the samples. It is interesting to note that the volume concentration versus complex viscosity data fall on a single curve at lower frequencies, Figs. 4.11 (a) and (b). As the frequency increases the data points become more and more scattered, Fig. 4.11 (c). On the other hand, the emitted volume concentration

versus phase angle data are scattered at both high and low frequencies, Figs. 4.12 (a) and (c). The most appropriate frequency would be the one in which volume concentration data would fall on a single line, irrespective of whether it is expressed in terms of complex viscosity or phase angle, providing a single valued function for the amount of emitted aerosol. Such a frequency seems to exist somewhere between 1 Hz and 10 Hz. Therefore, Figs. 4.11 and 12 indicate that the effective shear rate associated with simulated cough in the cough machine lies somewhere between 6.3 rad/s (1 Hz) and 63 rad/s (10 Hz) or between 6.3 1/s and 63 1/s in the straight trachea. Since the cough generated through the cough machine is an approximation of an actual human cough, this finding thus suggests that the effective shear rate in the tracheobronchial mucus layer for the analysis of a human cough probably also lies in the same range, i.e. between 6.3 1/s and 63 1/s. As shown in Figs. 4.11(b) and 12(b), the volume concentration of emitted droplets are highest for low viscosity (viscous fluid-like) samples, for which viscosity at 1 Hz is less than 0.3 Pa.s and phase angle at 1 Hz is close to 90 degree. There is a range of viscosity around 1 Pa.s at 1 Hz and phase angle around 45 degree (also at 1 Hz) where the volume concentration of emitted droplets is minimum, i.e. zero or close to zero. This optimum sub-range seems to exist near a phase angle value of 45 degree at 1 Hz, Fig. 4.12(b), where both the viscous and elastic behavior of mucus are equally dominant, i.e. the sample is neither viscous fluid-like nor elastic solid-like, and is rather strongly viscoelastic. The edge of this range is sharp toward lower complex viscosity (transition from viscous fluid-like to strongly viscoelastic type), but much smoother toward higher complex

viscosity values (transition between strongly viscoelastic type and elastic solid-like samples). Because of this, a co-adjuvant pharmacological intervention that modulates the properties of respiratory airways mucus to minimize emission should target a complex viscosity value somewhat higher than the minimum range, to avoid falling into the high emission range at low complex viscosity.

It is interesting to note that in Figs. 4.9 (a), (b), and (c) the size distributions of strongly viscous samples is mono-modal. The peak in the sub-micron size range, which is dominant for elastic solid-like samples, and even if not dominant is still present for viscous fluid-like samples, is absent in the size distribution of the strongly viscoelastic samples. Thus the range of complex viscosity, where complete suppression of droplets can be expected, is also the range where emitted droplets (if any) are less dangerous for disease transmission.

To determine whether or not this range of minimum emission is within physiologically relevant values we looked into the existing literature data on complex viscosity of human mucus. Rubin et al. [42] studied the rheological properties of respiratory mucus from 27 human subjects without lung disease. They reported the rigidity modulus, G^*, at 1 rad/s (0.16 Hz) and 100 rad/s (15.92 Hz) to be 2.04 ± 0.34 and 2.43 ± 0.37, respectively. These values when converted to complex viscosity ($\eta^* = G^*/\omega$, where ω is shear rate in rad/s) result in $\eta^* = 5$ to 24 Pa.s at 1 rad/s and 0.11 to 0.63 Pa.s at 100 rad/s. The complex viscosity (x-axis scale) range in Fig. 4.12(b), 0.1 to 100 Pa.s at 1 Hz (6.3 rad/s), covers the entire range of Rubin et al.'s [42] data and beyond. It is thus evident from Fig. 4.12(b)

that within the physiological range of viscoelastic properties of disease-free human mucus, there lies an optimum sub-range where generation of bioaerosol droplets during coughing would be minimum.

Figs. 4.11 and 12 also explain why certain individuals could act as super emitters, while others emit relatively less numbers of droplets, and why inhalation of saline solution reduces the emission of droplets [20] during coughing. Since normal human mucus covers a large range of viscosity and phase angle, those individuals with very low or very high viscosity and phase angle mucus are likely to emit more droplets, as per Figs. 4.11 and 12, while those with strongly viscoelastic mucus would emit a lesser number of droplets. Regarding the effect of inhalation of saline solution on the droplet generation, even though some studies [20] attributed the reduced emission of droplets to a change of surface tension, others [23] argued based on *in vitro* and *in vivo* studies that the change in exhaled droplets after inhalation of saline solution is due to a change in surface viscoelasticity and not due to surface tension. The current study supports the latter argument. The current study thus suggests that altering the viscoelastic properties, rather than the surface tension, can help achieve the goal of suppression of bioaerosol droplets generation during coughing as well as controlling the size distribution of the droplets. Finally, it should be noted that the current study has investigated the effect of rheological properties measured under oscillatory shear conditions. In the case of elongational properties, spinnability is known to increase with addition of Sodium Tetraborate (XLB) [43], i.e with an increase in

the amount of cross linking, indicating that there may be a similar relationship between elongational rheological properties and the emitted bioaerosol droplets.

4.4. Conclusion

This study confirms that the viscoelastic properties of mucus have a substantial effect on the size distribution and amount of droplets generated during coughing. Variation of surface tension in the range 30 to 55 dyne/cm did not show any change in the droplet size distribution. Viscoelastic properties vary substantially with shear rate. The complex viscosity increases with increase in the amount of cross linking, and decreases with increasing shear rate. The exact shear rate relevant to cough analysis is not known; however, the current study indicates that the effective shear rate relevant to the analysis of cough probably lies somewhere in between 6.3 1/s and 63 1/s (1 Hz and 10 Hz). The experimental results showed a decrease in particle size as the samples changed from viscous fluid type samples to viscoelastic type to an elastic solid type within the range of this study (0.1 to 35 µm). The study confirms that suppressing the generation of bioaerosol droplets and/or reducing the number to a minimum during coughing is practically achievable through careful modulation of viscoelastic properties of the respiratory airways mucus. The results further suggest that a co-adjuvant pharmacological intervention aimed at reducing the transmission of airborne diseases by modulating the viscoelastic properties of the respiratory secretions should target a complex viscosity value somewhere higher than the minimum range, to avoid falling into the high emission range at low complex viscosity.

References

[1] M. Vasudevan, C.F. Lange, Surface tension effects on instability in viscoelastic respiratory fluids, Math. Biosciences 205 (2007) 180-194.

[2] King M, Zayas J.G. Compositions and methods for improved respiratory tract mucus clearance. U.S. provisional patent 10/599,578, March 2004.

[3] R. Des Prez, C. Heim, Mycobacterium tuberculosis, in: G. Mandell, J.R. Douglas, J. Bennett, (Eds.), Principles and practices of infectious diseases, Churchill Livingstone, New York, 1990, pp. 1877-1906,.

[4] J. Lavoie, Y. Cloutier, J. Lara, G. Marchand, Guide on respiratory protection against bioaerosols - recommendations on its selection and use, Studies and Research Projects/Technical Guide RG-501 IRSST, Montréal, 2007.

[5] C.S. Cox, The aerobiological pathway of microorganisms, John Wiley and Sons Ltd, Chichester, 1987.

[6] ACGIH, American conference of governmental industrial hygienists (ACGIH), Bioaerosols: Assessment and control, Cincinnati, OH, 1999.

[7] S.W. Lenhart, T. Seitz, D. Trout, N. Bollinger, Issues affecting respirator selection for workers exposed to infectious aerosols: Emphasis on healthcare settings, Applied Biosafety 9 (2004) 2-36.

[8] E.C. Cole, C.E. Cook, Characterization of infectious aerosols in health care facilities: An aid to effective engineering controls and preventive strategies, Am. J. Infection Control 26 (1998) 453-464.

[9] Biosafety reference manual, Second edition, American Industrial Hygiene Association publications (AIHA), Fairfax, VA, 2000.

[10] N. Goyer, J. Lavoie, L. Lazure, G. Marchand, Les bioaérosols en milieu de travail : Guide d'évaluation, de contrôle et de prévention. Études et recherches, guide technique T-23,. Institut de recherche Robert-Sauvé en santé et en sécurité du travail, 2001.

[11] S.A. Lee, A. Adhikari, S.A. Grinshpun, R. Mckay, R. Shukla, H.L. Zeigler, T. Reponen, Respiratory protection provided by N95 filtering face piece respirators against airborne dust and microorganisms in agricultural farms, J. Occupational Environ. Hygiene 2 (2005) 577-583.

[12] A. Yassi, E. Bryce, Protecting the faces of health care workers: Knowledge gaps and research priorities for effective protection against occupationally-acquired respiratory infectious diseases. The Change Foundation, Ontario Hospital Association and Occupational Health and Safety Agency for Healthcare in BC, 2004.

[13]   W. Stahlhofen, J. Gebhart, J. Heyder, K. Philipson, P. Camner, Intercomparison of experimental regional aerosol deposition data, J. Aerosol Med. 2 (1989) 285–308.

[14] T.R. Gerrity, Calculated deposition of inhaled particles in the airway generations of normal subjects, J. Appl. Physiol. 47 (1979) 867–873.

[15] W.C. Hinds, Aerosol technology: properties, behavior, and measurement of airborne particles, John Wiley and Sons, Toronto, 1982.

[16] J.P. Duguid, The numbers and sites of origin of the droplets expelled during expiratory activities, Edinburgh Med. J. 52 (1945) 385-401.

[17]   J.P. Duguid, The size and the duration of air-carriage of respiratory droplets and droplet-nuclei, J. Hygiene 4 (1946) 471–480.

[18]   R.G. Loudon, R.M. Roberts, Droplet expulsion from the respiratory tract, Am. Rev. Res. Dis. 95 (1967) 433–442.

[19]   R.S. Papineni, F.S. Rosenthal, The size distribution of droplets in the exhaled breath of healthy human subjects J. Aerosol Med. 10 (1997) 105–116.

[20]   D.A. Edwards, J.C. Man, P. Brand, J.P. Katstra, K. Sommerer, H.A. Stone, E. Nardell, G. Scheuch, Inhaling to mitigate exhaled bioaerosols, Proc. Natl. Acad. Sci. pp. 17383–17388, 2004.

[21]   C.I. Fairfield, J.F. Stampfer, Particle concentration in exhaled breath, Am. Ind. Hygiene Assoc. J. 48 (1987) 948–949.

[22]   R. Clarke, J. Katstra, J. Man, W. Dehaan, D.A. Edwards, L.C. Griel, Pulmonary delivery of anti-contagion aerosol to diminish exhaled bioaerosols and airborne infectious disease, Am. J. Infect. Control 33 (2005) e85.

[23]   W. Watanabe, M. Thomas, R. Clarke, A.M. Klibanov, R. Langer, J. Katstra, G.G. Fuller, L.C. Griel, J. Fiegel, D. Edwards, Why inhaling salt water changes what we exhale, Journal of Colloid and Interface Science 307 (2007) 71-78.

[24]   C.A. Evrensel, Md.R.U. Khan, P.E. Krumpe, Response of a viscoelastic layer (mucus) to turbulent airflow in a rigid tube, Tech. Health Care 16 (2008) 355-366.

[25] S.W. Clarke, J.G. Jones, D.R. Oliver, Resistance to two-phase gas-liquid flow in airways, J. Appl. Physiol. 29 (1970) 464-471.

[26] M. King, G. Brock, C.C. Lundell, Clearance of mucus by simulated cough, J. Appl. Physiol. 58 (1985) 1776-1982.

[27] C.A. Evrensel, A.A. Hassan, P.E. Krumpe, An experimental investigation of interaction of airflow with a viscoelastic layer, Advances in Bioengineering, A.P. Yoganathan, (Ed.), ASME BED 39 (1998) 93-94.

[28] M. King, H.K. Chang, M.E. Weber, Resistance of mucus-lined tubes to steady and oscillatory airflow, J. Appl. Physiol. 52 (1982) 1172-1776.

[29] A.A. Hassan, C.A. Evrensel, P.E. Krumpe, Clearance of viscoelastic mucus simulant with airflow in a rectangular channel, an experimental study, Tech. Health Care 14 (2006) 1-11.

[30] M. Gad-El-Hak, The response of elastic and viscoelastic surfaces to a turbulent boundary layer, J. Fluid Mech. 53 (1986) 206-212.

[31] M. Gad-El-Hak, R.F. Blackwelder, J.J. Riley, J. James, On the interaction of a compliant coatings with boundary layer flows, J. Fluid. Mech. 140 (1984) 257-280.

[32] C.A. Evrensel, A.A. Hassan, K.F. Korver, P.E. Krumpe, High-speed visualization of the airflow-viscoelastic-layer interface, in: A.E. Engin, (Ed.), Proc. of the third Biannual Conf. on Engineering Systems Design and Analysis, 77 (1996) 183-188.

[33] C.A. Evrensel, A. Kalnins, Response of a viscoelastic slab to a viscous fluid flow, J. Appl. Mech. 55 (1988) 660-666.

[34] C.A. Evrensel, A. Kalnins, Response of a compliant slab to inviscid incompressible fluid flow, J. Acoust. Soc. Am. 78 (1985) 2034-2041.

[35] C.A. Evrensel, Md.R.U. Khan, S. Elli, P.E. Krumpe, Viscous airflow through a rigid tube with compliant lining: A simple model for the air-mucus interaction in pulmonary airways, Trans. ASME J. Biomech. Eng. 115 (1993) 262-269.

[36] C.A. Evrensel, Md.R.U. Khan, Interaction of laminar airflow with viscoelastic airway mucus, Tech. Health Care 11 (2003) 149-159.

[37] Y. Zhang, W.H. Finlay, E.A. Matida, Particle deposition measurements and numerical simulation in a highly idealized mouth-throat, J. Aerosol Sci. 35 (2004) 789–803.

[38] S. Shah, K. Fung, S. Brim, B.K. Rubin, An in vitro evaluation of the effectiveness of endotracheal suction catheters, Chest, 128 (2005) 3699-3704.

[39] J.C. Lasheras, E. Villermaux, E.J. Hopfinger, Break-up and atomization of a round water jet by a high speed annular air jet, J. Fluid Mech. 357 (1998) 351-379.

[40] J.C. Lasheras, E.J. Hopfinger, Liquid jet instability and atomization in a coaxial gas stream, Annual Rev. Fluid Mech. 32 (2000) 275-308.

[41] M. Vasudevan, C.F. Lange, Property dependence of onset of instability in viscoelastic respiratory fluids, Int. J. Eng. Sci. 43 (2005) 1292-1298.

[42] B.K. Rubin, O. Ramirez, J.G. Zayas, B. Finegan, M. King, Collection and analysis of respiratory mucus from subjects without lung disease, Am. Rev. Resp. Dis. 141 (1990) 1040-1043.

[43] G. Zayas, J. C. Valle, M. Allonso, H. Alfaro, D. Vega, G. Bonilla, M. Reyes, M. King, A new paradigm in respiratory hygiene: modulating respiratory secretions to contain cough bioaerosol without affecting mucus clearance, BMC Pulmonary Medicine 7 (2007) doi:10.1186/1471-2466-7-11.

Part 3: Application 2: Structure of Asphaltene Nanoaggregates in Bitumen and Heavy oil

Chapter 5: Introduction

5.1. Introduction

The continuous increase of demand for petroleum-fuel in the world market, the gradual depletion of world's resources of light and sweet crude oil, and the advancement of technology lowering the cost for extraction of bitumen from oil sands, have altogether turned the bitumen and heavy oil into an important source of world's energy supply chain. Particularly in Alberta, as of 2007, more than one million barrels per day (bpd) of bitumen from the oil sands were being produced. This number may reach as high as 3.5 million bpd by 2020. It is estimated that Alberta has a reserve of about 1.7 trillion barrels of bitumen which could meet Canada's energy needs for the next two hundred years. The province's upgrading capacity is currently about 800,000 bpd, and it is expected to increase to over 2.5 million bpd by 2020. As the production and the amount of upgrading of bitumen are continuously increasing, the need for more efficient upgrading processes has become more important. The upgrading of the denser fractions of bitumen and heavy oils to distillable products is achieved by either thermal coking or catalytic hydro conversion. To improve the operability and efficiency of both processes, as well as for discovery of more innovative upgrading processes, a complete

understanding of the structure and behavior of asphaltene nanoaggregates is required. Knowledge about the structure and behavior of asphaltenes will be helpful not only for the operability and efficiency of processes, but also for the design of equipment and mitigation of fouling. Fouling of process vessels and heat transfer equipment is a major concern in processing the bitumen and heavy oils. Asphaltenes play an important role in fouling of equipment through mechanisms that include liquid-phase instability and coke formation [1].

In this part of the dissertation i.e. from chapter 5 to chapter 8, the rheological behavior of bitumen and heavy oils will be exploited for obtaining information regarding the structure and behavior of asphaltene nanoaggregates present in bitumen and heavy oils.

5.2. Composition of Bitumen and Heavy Oils

Bitumen and heavy oils are complex mixtures of thousands or millions of different molecules without repeating molecular unit [2], which can be chemically defined as a complex crude consisting of polycyclic, napthenic and aromatic hydrocarbon species, and heterocyclic chemical compounds [3]. Since it is extremely difficult to do a component-by-component analysis of hundreds of thousands of chemical compounds present in bitumen and heavy oils, the components are analyzed or described in terms of solubility classes. For example, the components which are soluble in aromatic solvents, such as benzene or toluene, but are insoluble in n-heptane or n-pentane are known as asphaltene,

while those soluble in n-heptane or n-pentane are defined as maltene. Maltenes can again be separated into three fractions: (i) saturates (ii) aromatics and (iii) resins. Saturates are distinguishable from the rest of the compounds by the absence of π-bonds. The resins are higher in heteroatoms and have a higher concentration of aromatic carbon, while the asphaltenes are the highest molar mass fractions and contain most of the polar compounds [4]. The compositions of Athabasca bitumen (Alberta) and Maya crude oil (Mexico), used throughout chapters 6 to 8, in terms of saturates, aromatics, resins and asphaltenes, are presented in Table 5.1. The characteristics of bitumen and heavy oils are quite different from those of conventional crude oils. The generally a high specific gravity (>0.95), a low hydrogen-to-carbon ratio (~1.5), and contain large amounts of asphaltenes (>5 wt %), heavy metals (e.g. vanadium and nickel), heteroatoms (e.g. sulfur, nitrogen and oxygen) and inorganic fine solids [4].

Table 5.1. SARA analysis for Athabasca bitumen and Maya crude samples

Sample	Saturates	aromatics	resins	C5 asphaltenes
	wt. %			
Athabasca bitumen	16.1	48.5	16.8	18.6
Maya crude	31.6	42.5	10.2	15.7

5.3. Asphaltenes Chemistry and Structure

Asphaltenes are defined as the pentane or heptane-insoluble and toluene-soluble fractions. They are mixtures of poly-dispersed condensed polyaromatic units,

containing heteroatoms and aliphatic side chains [2], whose exact composition is not well defined [1]. They are characterized by fused ring aromaticity, small aliphatic side chains and polar heteroatoms-containing functional groups (e.g. carboxylic acids, carbonyl, phenol, pyrroles, and pyridines) capable of donating or accepting protons inter and intra-molecularly [5]. They are known to form aggregates through self-association, and are assumed to be a continuum of aggregates of increasing effective molar mass [6].

The colloidal model of bitumen, which describes bitumen as a colloidal system containing particles formed by its heavier fractions, was first proposed by Nellensteyn in 1924 [7] and was extended to crude oil by Sachenen in 1927 [8]. At that point, little or no molecular structural information was available for these colloidal particles which today are known as asphaltenes. In 1931 Marcusson [9] proposed that the heavy fractions of crude oil (asphaltenes) are formed by polycyclic aromatic molecules.

The fact that asphaltenes have a chain structure of saturated and aromatic rings connected by short alkyl chains was proposed by Hillman and Barnett in 1937 [10], which was based on simple chemical reasoning of relative solubility. Pfiffer and Saal, in 1940 [11], provided simplified 2D diagrams of asphaltenes as chaotic clusters of resin and aromatic molecules located around an asphaltene core. In 1961, Yen [12] and coworkers found some degree of short range ordering through x-ray diffraction on solid asphaltene, which was explained in terms of stacking of aromatic regions in the asphaltene molecules. Frankman et al. (1990)

[13], Strausz et al. (1999) [14, 15], and Peng et al. (1997) [16] studied the number of aromatic rings extension and type of the alkyl side chains and of the bridging groups using selective Ru catalyzed oxidation. During the last two decades, computer simulation techniques were widely employed for molecular simulation of asphaltene and resin aggregates. Murgich and Strausz (1996, 2001), Murgich 2003, and Priyanto et al. (2001) are a few such examples. As a result of the advancements in experimental and numerical techniques, researchers are now able to predict asphaltene structures using experimentally obtained average molecular weight and energy minimization technique in molecular simulation. One such model asphaltene structure is shown in Fig. 5.1 [17]. Molecular structure remains hotly debated.

5.4 Phase Behavior of Bitumen and Heavy Oil

The phase behaviors of bitumen and heavy oil are complex. This subject is addressed in detail elsewhere [18, 19]. The phase behavior data are critical inputs for process development, process design, and process operation activities related to the production, transport and refining of bitumen and heavy oils. These materials, like many other fluids of industrial interest, are opaque to visible light, and their phase behaviour is not amenable to investigation using conventional view cell technologies or even X-ray transmission tomography. A combination of techniques is required to elucidate their phase behaviour. Differential scanning calorimetry (DSC) is a sensitive technique for the detection and evaluation of phase transitions. Rheological analysis, and phase angle measurements in
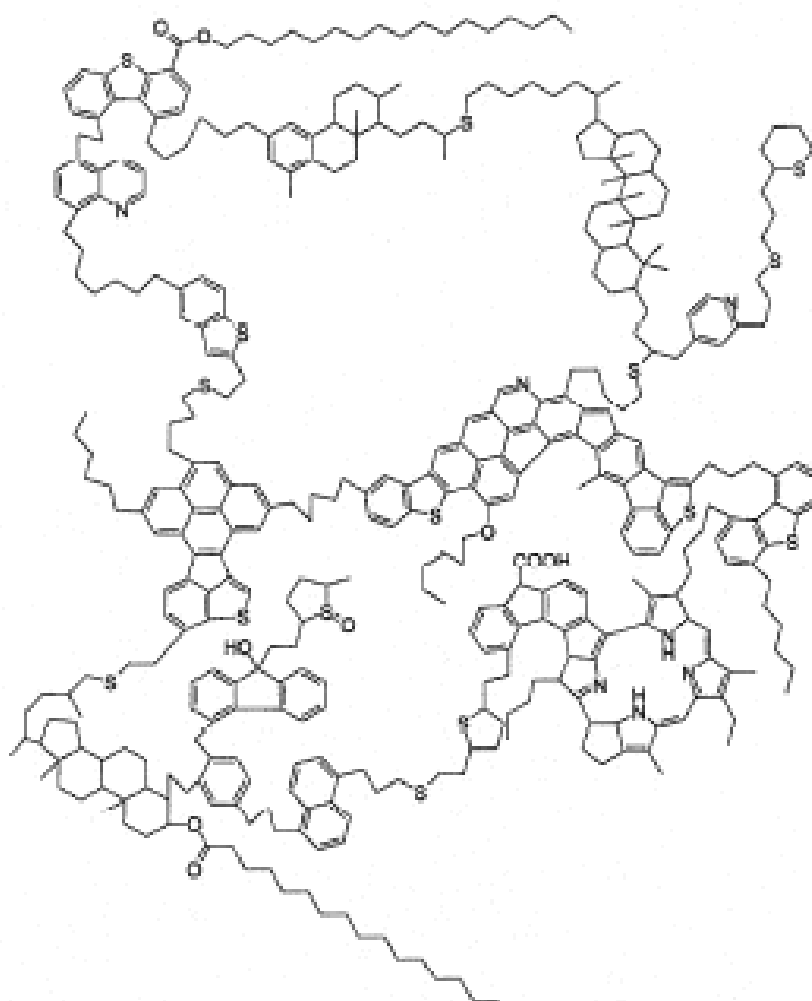
Fig . 5.1 A model structure for asphaltene molecule

particular, can be used to identify the nature of phase transitions as it sheds light on phase states. The phase behavior knowledge is also important for proper understanding of rheological data. Key attributes relevant to the interpretation of rheological data include:

1.   the maltene fractions of these feeds solidify, in part, at temperatures of industrial interest.

2.   the asphaltene fraction can be filtered selectively from the balance of the feed at 473 K.

These attributes of the two feeds are important because they guide the interpretation of rheological data. For example, Maya crude comprises 15.7 wt % pentane asphaltenes. At 283 K, ~ 32 wt % of the maltene fraction is solid, while at 325 K, the maltene fraction is liquid. Without fore knowledge of this significant change in phase behavior, the rheological behavior and changes in rheological behavior in this temperature interval are readily misattributed. That asphaltenes or asphaltenes + undifferentiated maltenes are filterable at 473 K, and that the mass fraction of asphaltenes passing through filters is a function of filter size is also important. It suggests that asphaltenes form dispersions, and that there are no specific interactions with maltene constituents, at least not at 473 K. With this background, one can notionally envisage asphaltenes in these feeds as rigid particles or as particles with poorly defined boundaries with the surrounding fluid. These two cases are illustrated in Figure 5.2, and they can be discriminated at high concentration if the rigid particles do not interact strongly with one another where the particles in Figure 5.2 a are expected to have a measurable yield stress.

(a)   (b)
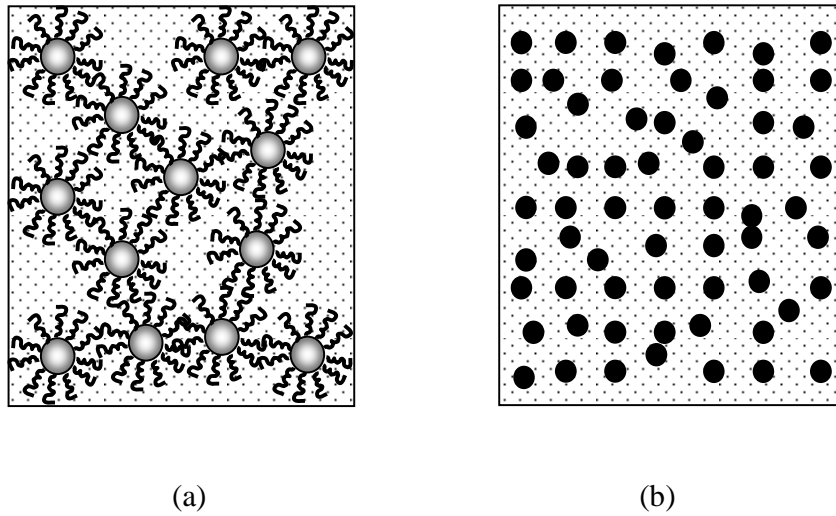
Figure 5.2: Notional particulate structures for asphaltenes (a) particles with poorly

defined boundaries with the surrounding fluid, and (b) rigid particles.

(a)   (b)   (c)
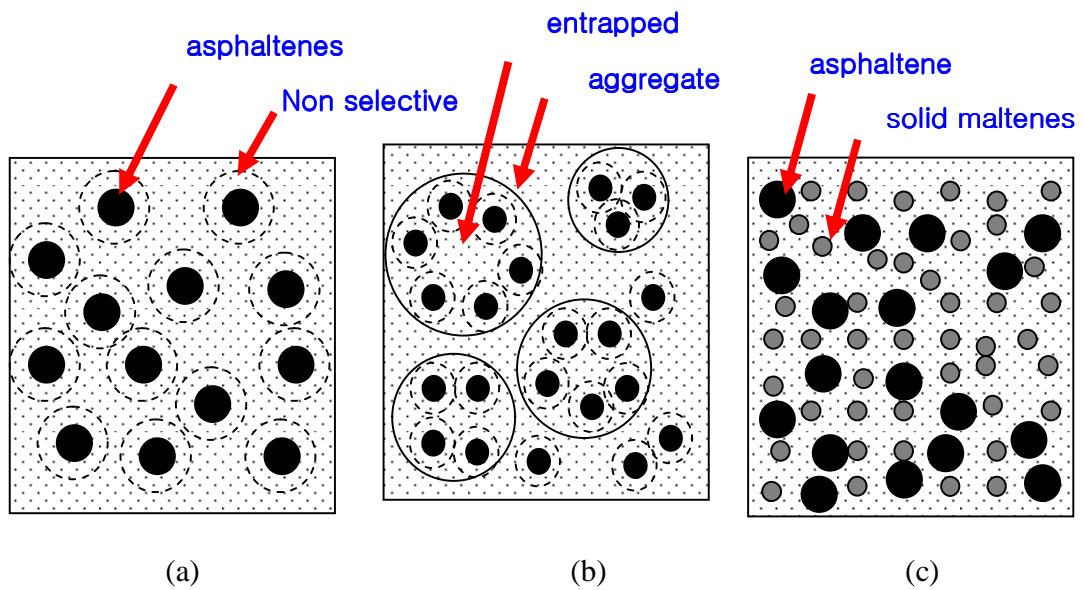
Figure 5.3 Possible structures arising in bitumen and heavy oil: (a) dispersion with

a non selective solvation layer, (b) maltene entrapment in asphaltene aggregates,

and (c) asphaltenes and asphaltene aggregates in a dispersion of solid maltenes in

liquid maltenes.

By extension, one can envision the feed stocks as comprising unsolvated or non-selectively solvated, Figure 5.3 a, asphaltene nano particles that may entrap maltenes as they aggregate, Figure 5.3 b. However, the simplest model for these feed stocks is primary asphaltene particles and asphaltene nano aggregates, dispersed particles in a liquid or liquid + solid maltene dispersion Figure 5.3 c.

References

1. O.J. Asprino Brinez, 2005. Fluid Properties of Asphaltenes at 310--530°C, (M.Sc.), University of Alberta (Canada), Canada.

2. S. Rahmani, 2002. Kinetics and Phase Behavior in Asphaltene Cracking, (Ph.D.), University of Alberta (Canada), Canada.

3. A.G. Mazza, 1987. Modelling of the Liquid-Phase Thermal Cracking Kinetics of Athabasca Bitumen and Its Major Chemical Fractions, (Ph.D.), University of Toronto (Canada), Canada.

4. X. Zou, 2003. Selective Removal of Inorganic Fine Solids, Heavy Metals and Sulfur from Bitumen/Heavy Oils, University of Toronto, Toronto.

5. K.L. Gawrys, and P.K. Kilpatrick, 2004, "Asphaltene Aggregation: Techniques for Analysis", Instrumentation Science and Technology, 32**:** 247-253.

6. H. Alboudwarej, K. Akbarzadeh, J. Beck, W.Y. Svrcek, and H.W. Yarranton, 2003, "Regular Solution Model for Asphaltene Precipitation from Bitumens and Solvents", Aiche Journal, 49**:** 2948-2956.

7. F.J. Nellensteyn, 1923. The Colloidal Structure of Bitumen, Delft Technical Universtiy.

8. A.N. Sachanen, 1925, "Uber Den Zustand Der Asphaltene Und Erdolharze in Erdolen Und Erdol-Produkten", Petroleum Zeit, 21.

9. J. Marcusson, 1931, "Die Naturlichten and Kunstlichen Asphalte", Leipzig.

10. A.B.B. Hillman E.S. , Proc. 4th annual Meeting, ASTM, 1937, pp. 558.

11. A.P.N.S. J.P. Pfeiffer, 1940, "Asphaltic Bitumen as Colloid System", J. Phys. Chem, 44.

12. J.G.E. T.F. Yen, and S.S. Pollack, 1961, "Invenstigation of the Structure of Petroleum Asphaltenes by X-Ray Diffraction", Annalyt. Chem., 33.

13. T.M.I. Z. Frankman, E.M. Lown, and O.P. Strausz, 1990, "Oxygen Compounds in Athabasca Asphaltene", Energy & Fuels, 13.

14. T.W.M. O.P. Strausz, and E.M. Lown, 1999, "Structural Features of Boscan and Duri Asphaltenes", Energy & Fuels, 13.

15. T.W.M. O.P. Strausz, F. Faraji, E.M. Lown, and P. Peng, 1999, "Additional Structural Details on Athabasca Asphaltene and Their Ramifications
", Energy & Fuels, 13.

16. A.M.-I. P. Peng, A. Hogg, and O.P. Strausz, 1997, "Molecular Structure of Athabasca Asphaltene: Sulfide, Ether, and Ester Linkages", Energy & Fuels, 11.

17. J. Murgich, J.A. Abanero, and O.P. Strausz, 1999, "Molecular Recognition in Aggregates Formed by Asphaltene and Resin Molecules from the Athabasca Oil Sand", Energy & Fuels, 13**:** 278-286.

18. B. Zhao, and J.M. Shaw, 2007, "Composition and Size Distribution of Coherent Nanostructures in Athabasca Bitumen and Maya Crude Oil", Energy & Fuels, 21**:** 2795-2804.

19. M. Fulem, M. Becerra, M.A. Hasan, B. Zhao, and J.M. Shaw, 2008, "Phase Behaviour of Maya Crude Oil Based on Calorimetry and Rheometry", Fluid Phase Equilibria, 272**:** 32-41.

Chapter 6

Bitumen and Heavy Oil Rheological Properties – Reconciliation with Viscosity Measurements

Ala B. Bazyleva , MD. Anwarul Hasan , Michal Fulem , Mildred Becerra ,

John M. Shaw

ABSTRACT

Complex viscosity and phase angle measurements for Athabasca bitumen and Maya crude oil were performed with a rotation rheometer using parallel plates and a double gap cylinder in the oscillatory mode over the temperature range (200 to 360) K. A large range of shearing conditions were applied (frequency of oscillations, shear stain or stress) and up to three orders of magnitude variation in measured viscosity values for individual samples at fixed temperature were obtained. Athabasca bitumen and Maya crude were found to be solid-like materials up to (260 to 280) K and (230 to 240) K, respectively. Athabasca bitumen is a non-Newtonian shear-thinning fluid up to (310 to 315) K, whereas Maya crude is a shear-thinning fluid up to (280 to 285) K. Both are Newtonian at higher temperatures. Maya crude oil was also found to possess thixotropic behavior. Athabasca bitumen reveals thermal irreversibility of complex viscosity, if it is heated above 360 K. These rheological behaviors are attributed to the multi phase behavior of these materials over the temperature range of interest and these results can be used to reconcile the large differences in reported viscosity values for bitumen and heavy oil obtained with diverse viscometers where shear rate and

other variables are not controlled. Additional artifacts introduced during measurements are also addressed. Sample variation due to geographical location, depth of formation, production and post-production processing can also result in up to three orders of magnitude differences between measured "viscosity" of bitumen when the measurement method and temperature are fixed. The flow properties of bitumen and heavy oil are expected to be strong functions of sample source and the hydrodynamics prevailing in situ or in processes at temperatures where non-Newtonian behaviors prevail.

KEYWORDS: Athabasca bitumen; Maya crude; viscosity; phase angle; non-Newtonian fluid; thixotropy.

6.1. Introduction

Bitumen and heavy oil have become main stream energy resources.[1] Accurate thermochemical and transport properties for these materials are key inputs for the oil industry. For example, viscosity is of crucial importance for production, transport, and refining operations. Since bitumen as well as heavy oils are complex multi-component fluids and multiphase over a broad range of temperatures,[2] three main issues must be taken into account when reporting, interpreting, and using viscosity data: (1) sample identity (origin or geographical location, elevation or depth of formation, sample pre-treatment history); (2) experimental conditions (measurement method, temperature, shear conditions, sample history during measurements); (3) applicability, restrictions, and errors of

111

certain experimental methods and techniques when applied to such complex fluids.

Chemical and phase composition, degree of dispersion, strength of intermolecular and interparticle interactions are the main characteristics, from an internal point of view, that are responsible for rheological behavior of heavy oils and bitumen. Without insight into the structure of these fluids, observed rheological behavior can be misinterpreted or attributed to experimental error or other extraneous factors. The large deviation in reported viscosity values for Athabasca bitumen in the literature is well known.[3,4] More than 20 sets of viscosity data for bitumen from the Athabasca area have been reported.[5-29] The unusual properties of bitumen are typically attributed to asphaltene association.[30,31] However, the various sets of viscosity values were obtained using diverse measurement techniques, many of which presume Newtonian sample behavior as a basis for measurement. The variation of the values reaches two to three orders of magnitude at fixed temperature but, generally, the slope of the temperature dependence of viscosity, $\eta = \eta\ (T)$ is the same in most cases. This level of apparent measurement uncertainty is significant and is reflected in prediction errors for heavy oil viscosity commonly exceeding one to two orders of magnitude even for specialized correlations (ASTM D341-03, API procedure 11A4.2). Such uncertainties present challenges to producers targeting pipeline specifications for fluids. For example, Enbridge Pipelines Inc., having one of the largest crude oil and petroleum products pipeline systems, limits kinematic viscosities to 350 cSt at 285 K.[32] For an oil with a density of 1000 kg·m^{-3}, this

112

corresponds to a maximum dynamic viscosity of 0.350 Pa s. Hence, reliable viscosity data and predictions are required.

In this contribution, factors affecting the apparent viscosity of Athabasca bitumen and Maya heavy oil, are examined experimentally in the (200 to 410) K temperature range. Resource and sample preparation variability and the impact of measurement methods themselves are key lines of inquiry.

6.2. Experimental

6.2.1. Materials. Athabasca bitumen (Alberta, Canada) was obtained from Syncrude Canada Ltd. The sample was characterized as a coker feed obtained from mined bitumen subject to stream warm-water extraction, naphtha dilution, and naphtha recovery by distillation between (523 and 623) K. Some volatile constituents present initially are lost during sample preparation. Maya crude oil (a commercial-blend heavy-oil from Mexico) was supplied by the Mexican Petroleum Institute. Both samples were stored in closed vessels in a refrigerator prior to use. The SARA analysis results for both samples (Table 5.1) were obtained according to ASTM D2007 for saturates, aromatics, and resins and ASTM D3279 for pentane (C5) asphaltenes. These analyses were performed at the National Centre for Upgrading Technology (NCUT), Devon, Canada.

6.2.2. Thermogravimetric analysis. Thermogravimetric analysis of bitumen and heavy oil samples was performed using a TG-DSC 111 thermoanalyzer (Setaram, France). The initial masses of the aliquots were from (20 to 30) mg. Isothermal TGA curves of the samples at 293 K and 323 K and scanning TGA

curves up to 500 K were obtained in a dry helium stream. The mass loss of the samples due to evaporation of light components as a function of the time was recorded.

6.2.3. Rheological measurements. Rheological experiments were carried out in the oscillatory mode using a controlled stress/strain Bohlin Gemini HR Nano rheometer (Malvern Instruments Limited, UK). The following measuring configurations were used:

(1) a double gap 24/27 mm concentric cylinder with a Peltier assembly using the principle of the Peltier heat pump, allowing measurements from (258 to 453) K with stability of ±0.2 K;

(2) parallel plates (25 mm and 40 mm diameter) with an extended temperature cell (ETC) using a forced gas system to heat and cool the sample. The ETC can also be fitted with a low temperature extension (LTE) – cooling with cold vapors from liquid nitrogen, if measurements below ambient temperatures are required. The ETC in these two complementary configurations (with and without LTE) cover the temperature range from (123 to 823) K with stability better than ±0.2 K.

Sample temperature in the ETC is measured with a thermocouple (calibrated to ITS 90 using a PT100 resistance thermometer) inserted into the middle of the lower plate. A thermocouple was also used in the Peltier cylinder and calibrated in the same way. The uncertainty in temperature measurements in both cases is estimated to be less than 0.2 K.

All experiments were conducted under nitrogen atmosphere to avoid sample oxidation. The gap between the parallel plates was between (500 and 1000) µm

depending on the range of viscosity values studied. For measurements obtained with the double gap cylinder, the gap was fixed at the default value of 150 µm. The experimental conditions and the operating parameter values for the rheological experiments were validated by measuring the viscosity of the Canon certified viscosity standard N2700000SP and PRA standard oil #12. The agreement with the recommended data in the certified temperature range (293 to 349) K was within 5 %.

Two measuring techniques were applied: (1) temperature sweep measurements with the cooling and heating rates of 3 K·min^{-1} at constant frequency and constant shear stress or constant shear strain; (2) isothermal measurements at constant frequency and constant shear stress or constant shear strain (see details in the Section 3.2). The frequency of the oscillation was varied between 0.1 Hz and 10 Hz (or between 0.63 s^{-1} and 63 s^{-1} in terms of angular frequency, ω). The largest scatter for complex viscosity and phase angle values was realized at high frequency.

6.3. Results and discussion

6.3.1. Experimental artifacts in rheological measurements. Significant effort was expended to avoid introducing artifacts into the rheological measurements. These can arise from two sources. Samples can degrade or vaporize over the course of an experiment, impacting the evaluation of thermal history effects, or the rheometer itself may introduce artifacts due to local cooling or heating.

Local cooling effects. Operation of the extended thermal cell (ETC) with the low temperature extension (LTE) required a special procedure to avoid local cooling effects introduced by the cold nitrogen vapor. In a Bohlin Gemini HR nano rheometer, cold nitrogen enters the chamber containing parallel plates and a sample from only one side leading to a temperature gradient in a sample when the rheometer is operated in the oscillation mode. The temperature of the sample is recorded at the center of the lower plate, whereas viscosity is measured as an average value throughout the plate. Thus, the actual value of viscosity at the recorded temperature might be significantly lower than the measured one due to
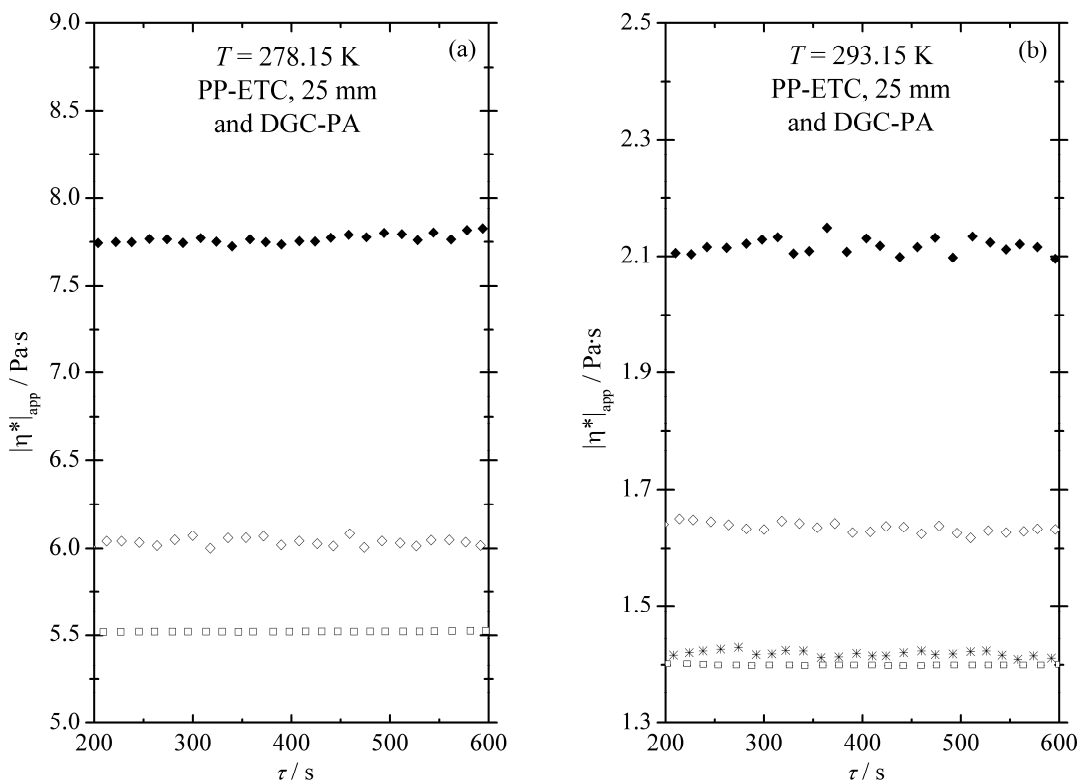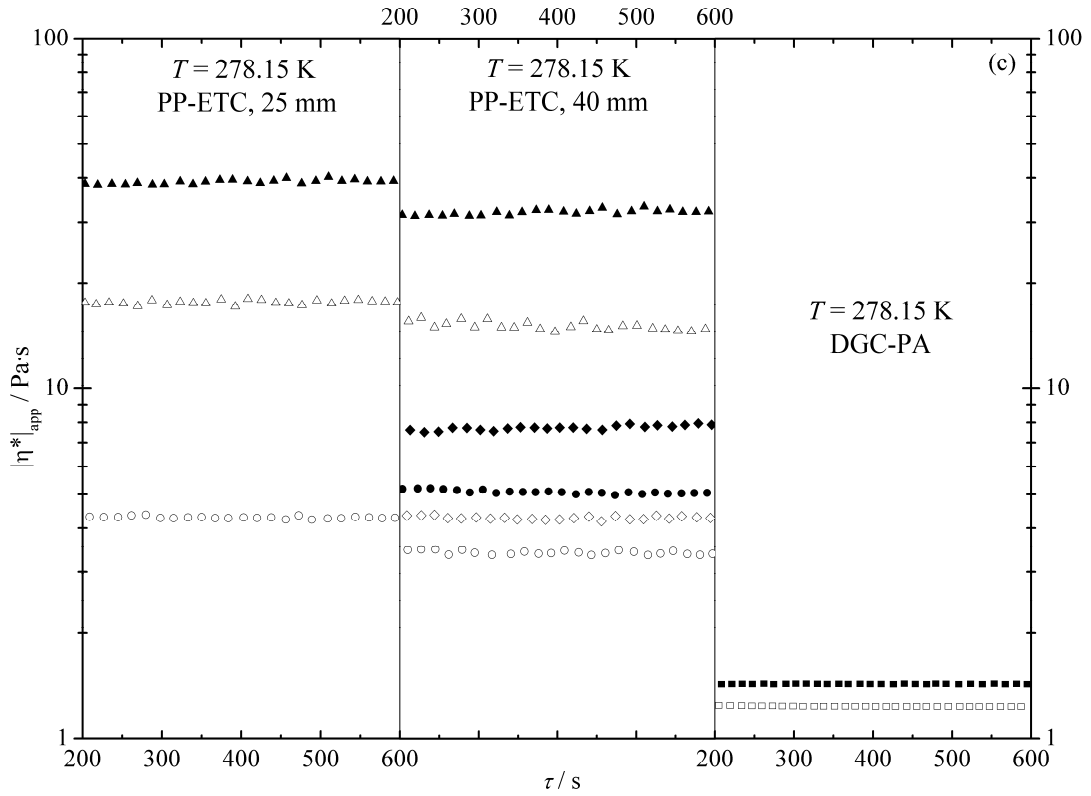
Figure 6.1. Variation of complex viscosity for PRA standard oil #12 at $T = 278.15$ K (a) and at $T = 293.15$ K (b) and for Maya crude oil at $T = 278.15$ K (c) depending on experimental technique ($\omega = 6.3$ s^{-1}). DGC-PA is the double gap cylinder – Peltier assembly: ■, from 0.1 % to 5% strain; □, 100 % strain. PP-ETC is the parallel plates – extended temperature cell (750 μm): ▲, 0.20 bar of N$_2$, 0.3 % strain; △, 0.15 bar of N$_2$, 0.3% strain; ◆, 0.20 bar of N$_2$, 30 % strain; ◇, 0.15 bar of N$_2$, 30 % strain; ●, 0.20 bar of N$_2$, 100 % strain; ○, 0.15 bar of N$_2$, 100 % strain; ✳, without cooling, 30 % strain.

the impact of local cooling as reported in Figure 6.1 for experiments with PRA standard oil #12, a Newtonian fluid, and Maya crude oil. The Peltier cylinder and

the ETC without LTE (i.e. without nitrogen cooling) provide viscosity values for PRA standard oil #12 at 293.15 K (Figure 6.1b), that are in good agreement within (2 – 3) % with the certified value – 1.449 Pa·s at 293.15 K. Below this temperature, the ETC requires the LTE with nitrogen cooling. According to the manufacturer, cold nitrogen at a gauge pressure of 0.20 bar from a Dewar should be used for rheological measurements in the ETC/LTE at isothermal conditions. From Figure 6.1, the resulting viscosity values are higher than those obtained with the Peltier cylinder, up to 50 % for PRA standard oil #12 and up to 25 times for Maya crude oil. Reduction of the nitrogen pressure to 0.15 bar gauge – the lowest pressure at which the device can operate in a steady way, allows us to reduce the temperature gradient and, hence, to obtain viscosity values closer to those obtained using the Peltier cylinder. Application of larger plates for the ETC/LTE also improves the results slightly, as shown for Maya crude oil (Figure 6.1c).

Thermal gradient effects also arose with the use of the ETC/LTE parallel plates, when examining the thixotropic behavior of Maya crude oil. At 278.15 K the viscosity dependence found using the ETC/LTE parallel plates over a range of shear strains was significant (9 times!) whereas the variation was only 15 % with the Peltier cylinder in the same shear strain range. This artifact makes it appear as if the experiments are performed outside of a linear visco-elastic region.

Sample degradation. Thermogravimetric analysis results revealed noticeable mass loss for Maya crude oil: 5.8 % during the first hour of exposure at 323 K and 1.0 % during the first hour of exposure at 293 K. The evaporation of light components at ambient and higher temperatures precludes use of the ETC for

rheological measurements under these conditions. For example, at 323 K, viscosity values increase continuously with time in the ETC, up to ten times within four hours. Hence, the Peltier system with a double gap cylinder was used for Maya crude down to 258 K (the low temperature limit for the Peltier). At lower temperatures the ETC/LTE was employed with as low pressure of cold nitrogen vapors as possible to maintain temperatures under study. Athabasca bitumen shows no mass loss during TGA measurements even at 500 K and the ETC was used for the whole temperature interval from (233 to 363) K.

6.3.2. Variation of viscosity with experimental conditions. Athabasca bitumen. Viscosity and phase angle measurements for Athabasca bitumen (Figure 6.2) were obtained on heating and cooling between (233 and 363) K at different
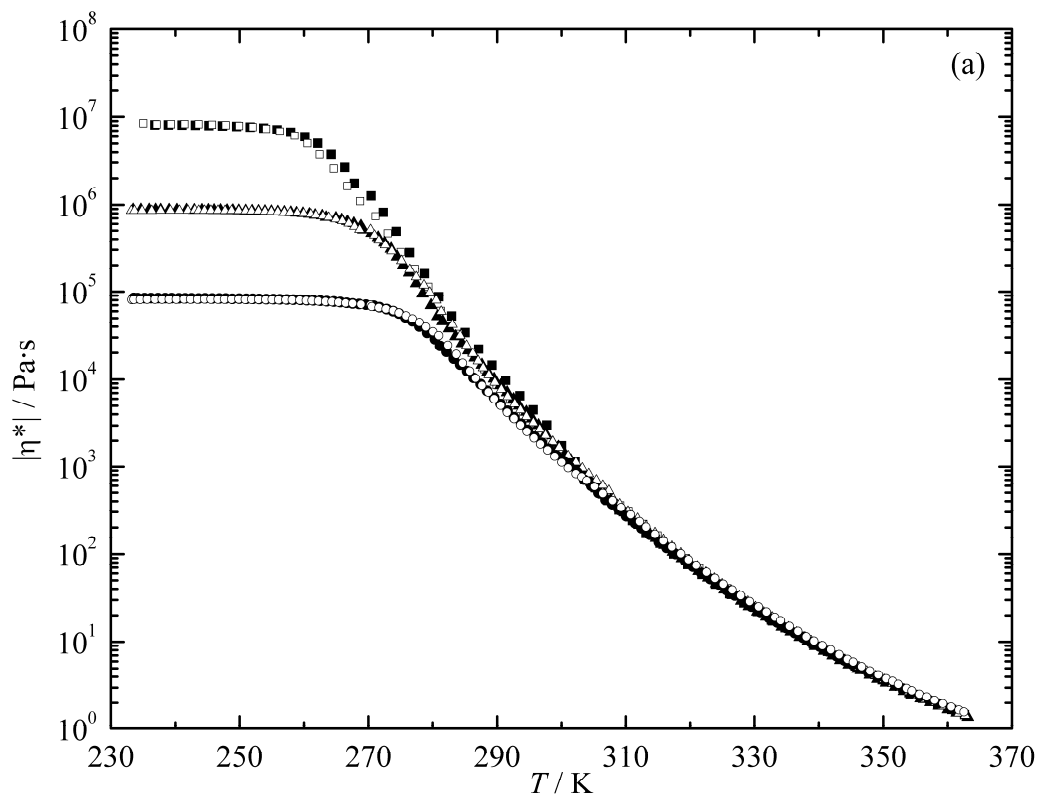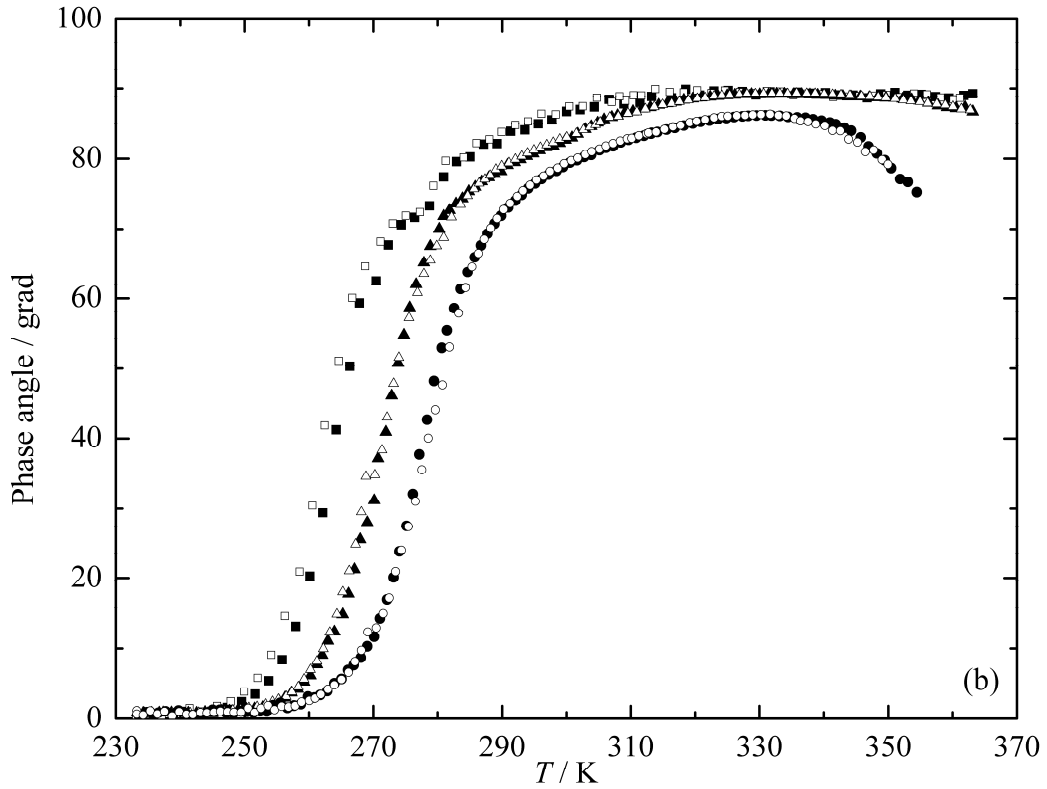
Figure 6.2. Frequency and temperature dependence of complex viscosity (a) and phase angle (b) for Athabasca bitumen (3 K min^{-1}, 0.3 % strain, 1000 μm gap): ■, cooling, $\omega = 0.63$ s^{-1}; □, heating, $\omega = 0.63$ s^{-1}; ▲, cooling, $\omega = 6.3$ s^{-1}; △, heating, $\omega = 6.3$ s^{-1}; ●, cooling, $\omega = 63$ s^{-1}; ○, heating, $\omega = 63$ s^{-1}.

oscillation frequencies at constant shear strain of 0.3 %. Rheological measurements from (233 to 313) K were carried out in the ETC/LTE using the lowest possible pressure of cold nitrogen, and at $T > 298$ K – in the ETC without cooling. Viscosity and phase angle values for the bitumen obtained using these two configurations agree with one another within 5 % and 1 %, respectively, in the overlap region – (298 to 313) K, i.e. the effect of local cooling in the

ETC/LTE is insignificant for high viscous Athabasca bitumen. Both sets of viscosity data are reported in Figure 6.2a and are indistinguishable.

In the studied temperature interval, the complex viscosity of Athabasca bitumen was found to be reversible with temperature variation when other shearing conditions are maintained constant. However, a frequency dependence is evident
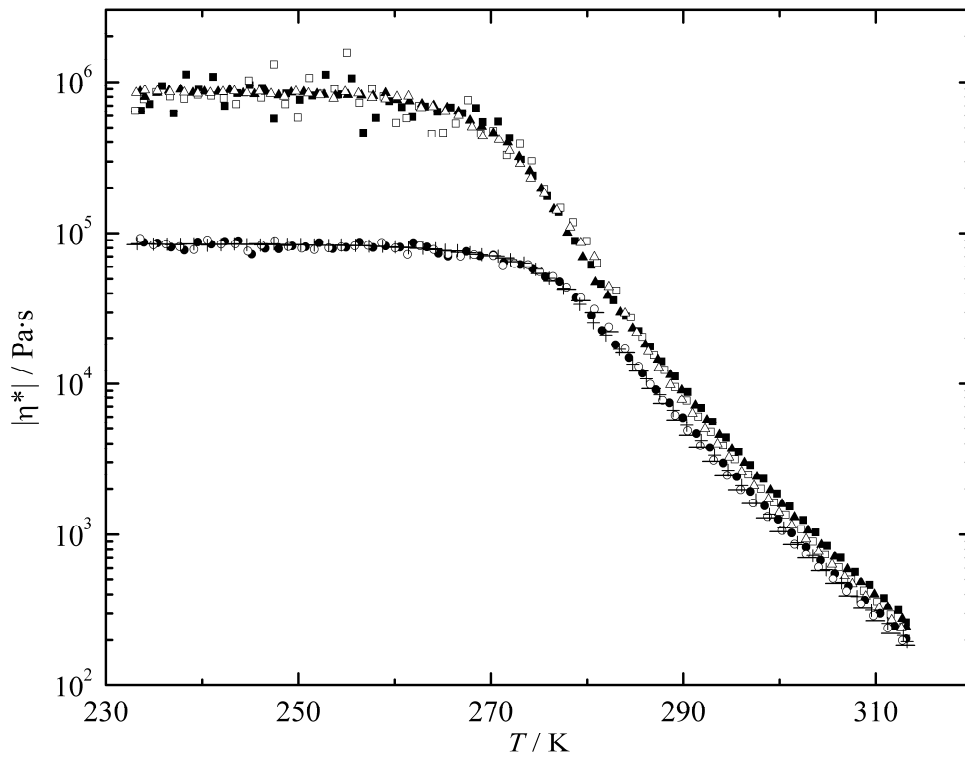
Figure 6.3. Shear stress dependence of viscosity for Athabasca bitumen (3 K min^{-1}, 1000 μm gap, τ is the shear stress): ■, cooling, ω = 6.3 s^{-1}, τ = 50 Pa; □, heating, ω = 6.3 s^{-1}, τ = 50 Pa; ▲, cooling, ω = 6.3 s^{-1}, τ = 500 Pa; △, heating, ω = 6.3 s^{-1}, τ = 500 Pa; ●, cooling, ω = 63 s^{-1}, τ = 200 Pa; ○, heating, ω = 63 s^{-1}, τ = 200 Pa; +, cooling, ω = 63 s^{-1}, τ = 2000 Pa; –, heating, ω = 63 s^{-1}, τ = 2000 Pa.

which provides evidence for non-Newtonian shear-thinning behavior, discussed in detail below, while the complex viscosity of Athabasca bitumen is independent of the shear stress (shear amplitude) applied (Figure 6.3). Higher temperature measurements, up to 413 K, revealed irreversibility of complex viscosity upon heating and cooling (Figure 6.4, two heating-cooling cycles). This behavior could be connected with irreversible (or slowly reversing) phase transitions in
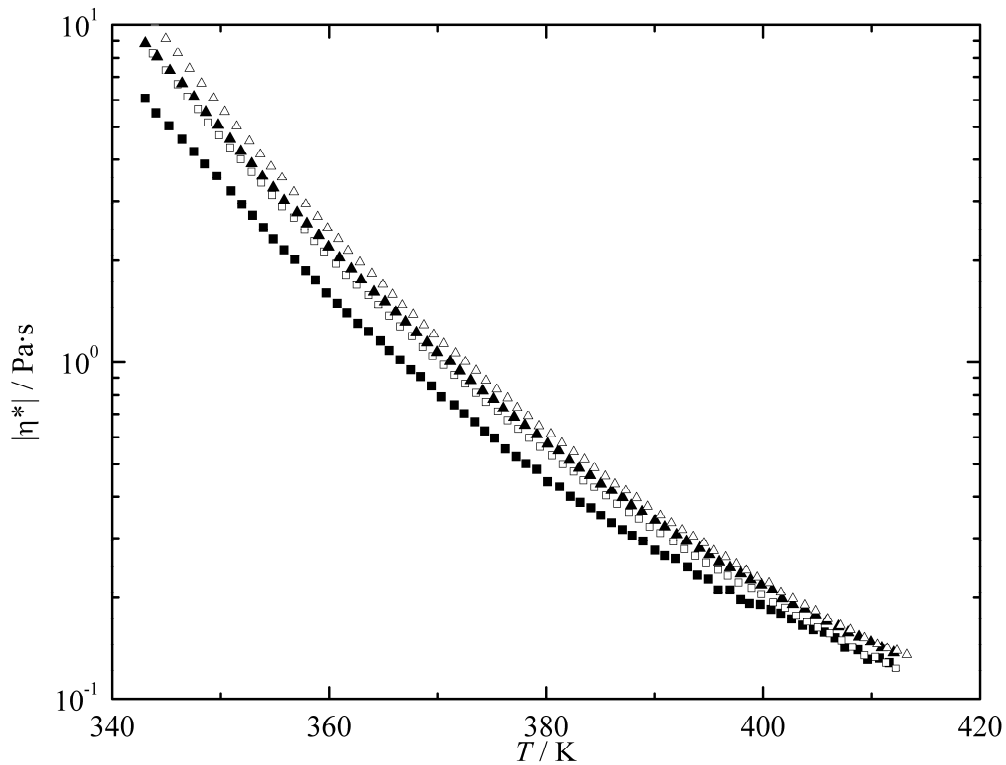
Figure 6.4. Evidence of a slow or irreversible phase transition in Athabasca asphalthenes from high-temperature viscosity measurements (3 K min^{-1}, 500 μm gap, ω = 6.3 s^{-1}, 5 Pa stress), successive experiments: ■, heating 1; □, cooling 1; ▲, heating 2; △, cooling 2.

asphalthenes. For example, from DSC measurements,[2,33,34] the melting behavior of asphalthenes includes an irreversible transition – first DSC scans are always more complicated than subsequent ones, which typically show only one broad endothermic transition. Since the rate of this transformation is lower than the temperature scanning rate in the viscosity measurements, the irreversible or slowly reversing behavior is observed in more than one (heating + cooling) cycle.

Maya crude oil. Since a large amount of sample (10 ml) is used with the double gap cylinder of the Peltier system, temperature sweep experiments could not give reliable viscosity values due to thermal inertia of materials on heating and cooling. That is why, complex viscosity and phase angle of Maya crude oil were measured from (203 to 298) K isothermally with a step of 5 K (or 2.5 K in the temperature range where viscosity gradient is high). In contrast to Athabasca bitumen, the results of the measurements are strongly influenced by the thermal prehistory of the Maya crude sample as well as experimental conditions. The isothermal equilibration time before an experiment is crucial for reaching constant viscosity values for Maya crude (Figure 6.5). Since the measuring system is closed and there is no evaporation of light components, this behavior could be explained by low rates of formation of contacts between molecules and molecular aggregates in the oil media and enough time should be given to the material to form an equilibrium interparticle network. The complex viscosity of Maya crude oil also exhibits a noticeable dependence on shear strain applied after reaching equilibrium (Figure 6.6). Low shear strain (depending on temperature) gives constant time-independent viscosity values, whereas higher strain results in
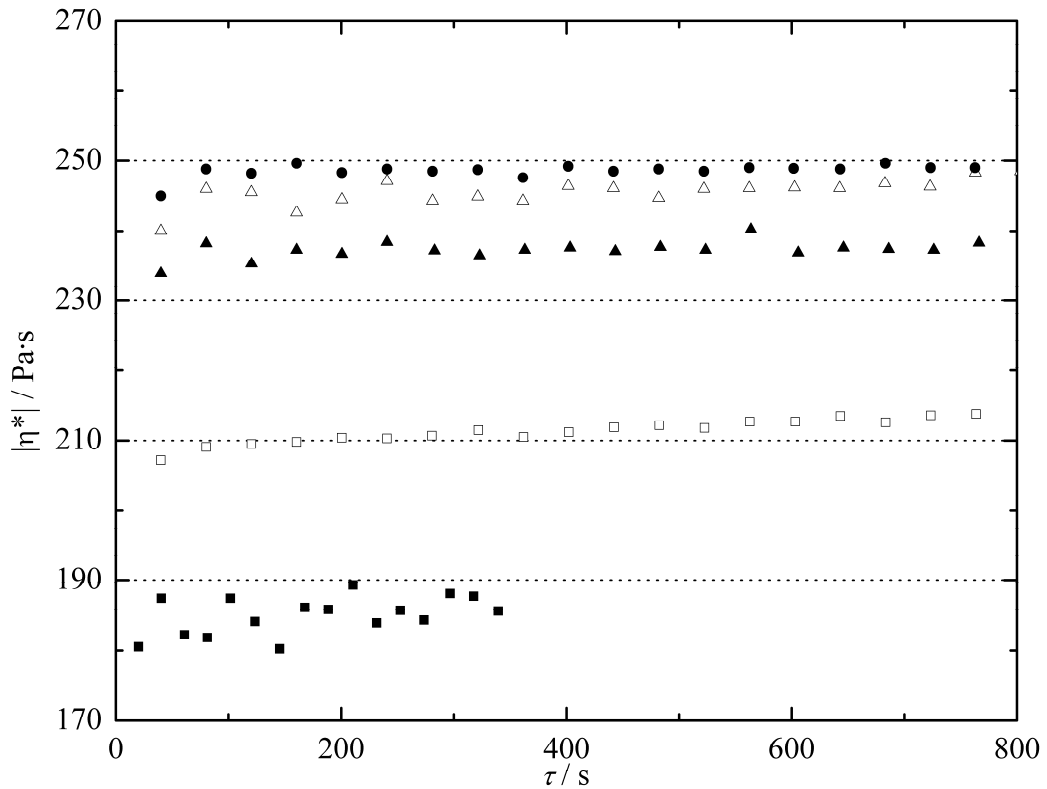
Figure 6.5. Time dependence of viscosity for Maya crude oil upon equilibration after reaching a stable temperature T = 260.65 K (double gap cylinder – Peltier assembly, ω = 0.63 s^{-1}, 0.1% strain): ■, after 30 min; □, after 60 min; ▲, after 135 min; △, after 190 min; ●, after 205 min.

continuous decrease in complex viscosity with time, which is characteristic of thixotropy. At lower temperatures, smaller strains reveal thixotropy and it is of larger magnitude than at higher temperatures, e.g.: compare Figure 6.6a with Figure 6b. This behavior is consistent with the earlier comment on kinetics of the inter particle network formation. Low strain does not influence the stability of the
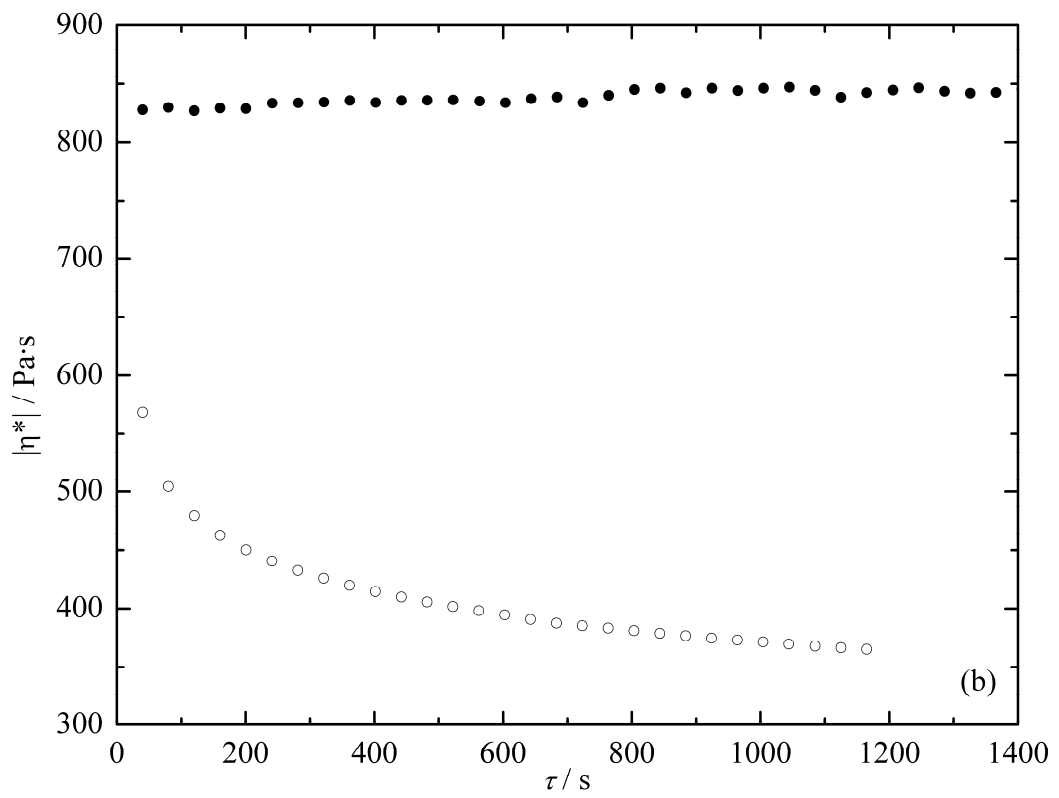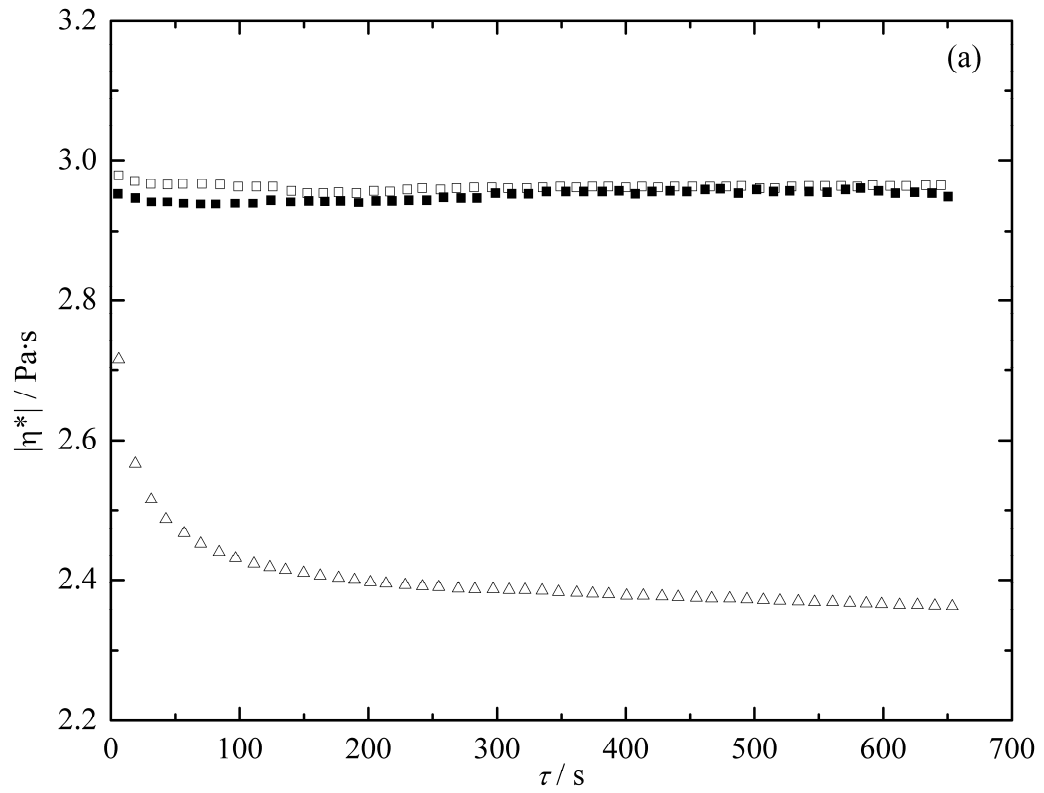
Figure 6.6. Time dependence of viscosity for Maya crude oil at (a) $T = 273.15$ K and $\omega = 6.3$ s^{-1} ; (b) $T = 258.15$ K and $\omega = 0.63$ s^{-1} (double gap cylinder – Peltier assembly): ■, 1% strain; □, 2% strain; △, 100%; ●, 0.2% strain; ○, 5% strain.

well-formed network but higher strain breaks networks down. At higher temperatures, some weak bonds are broken thermally, reducing the impact of thixotropy compared with lower temperatures.

Taking into account these two observations, the following experimental conditions were chosen for measurements of viscosity of Maya crude oil: (1) samples were maintained at each temperature until constant equilibrium viscosity values were reached; (2) all measurements were carried out at shear strain low enough not to provoke thixotropy but high enough to provide good accuracy for rheological measurements. The latter point is important since low shear strain, especially at high temperatures, is generated by stress, which could be close to or below the detection limit of the rheometer, causing significant scatter in the viscosity data. The complex viscosity and phase angle results for Maya crude oil are presented in Figure 6.7. Results obtained using parallel plates with the ETC/LTE and a double gap cylinder with the Peltier assembly agree within 7 % at $T = 258.15$ K, where the two methods overlap. Finally, along with Athabasca bitumen, the viscosity of Maya crude oil exhibits a frequency dependence.

Non-Newtonian behavior. Both Maya crude oil and Athabasca bitumen exhibit non-Newtonian shear-thinning behavior, i.e. viscosity decreases with increasing

126
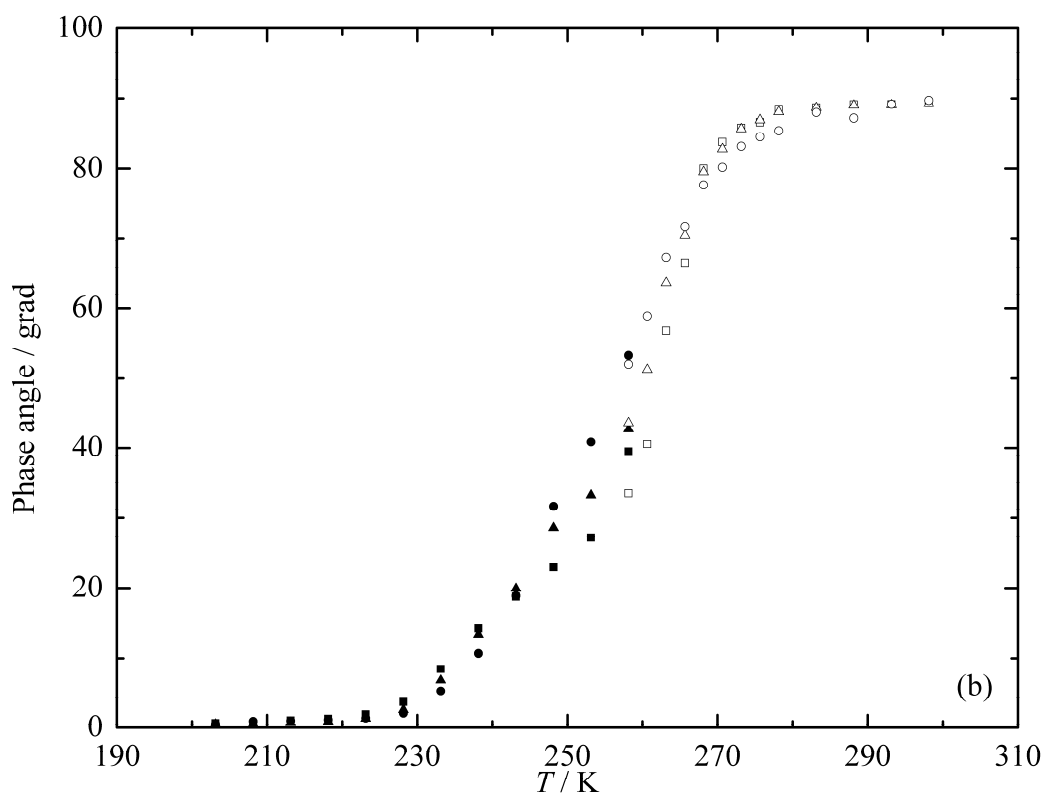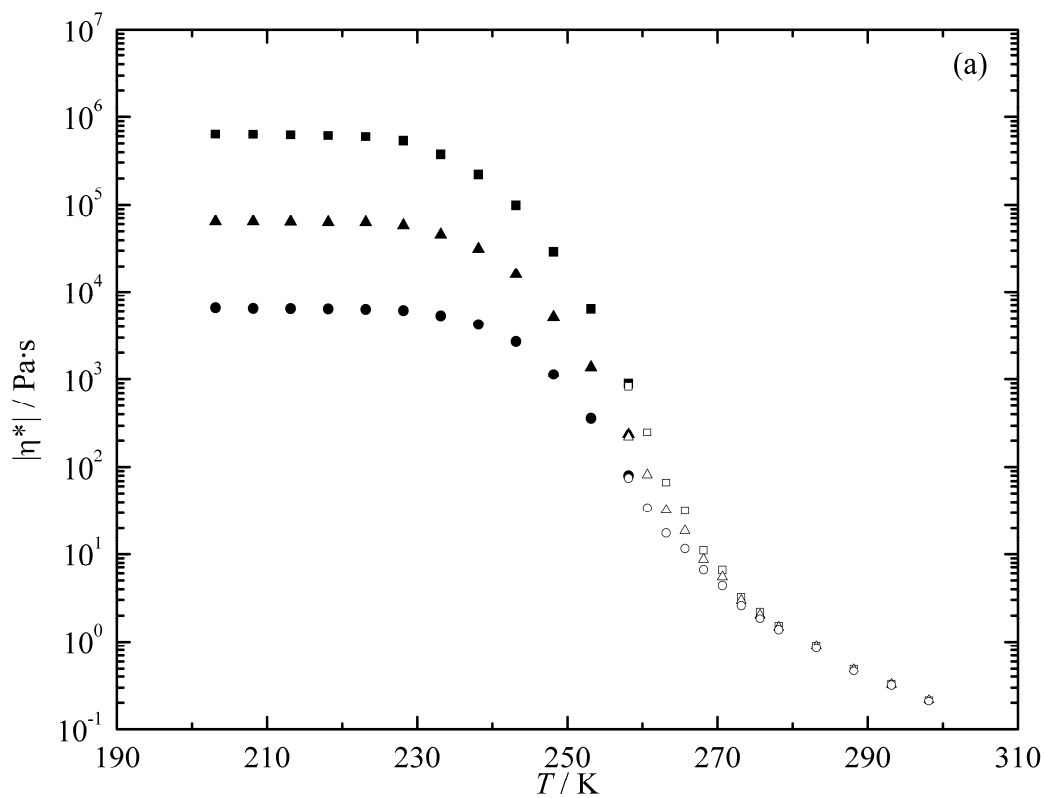
Figure 6.7. Frequency and temperature dependence of complex viscosity (a) and phase angle (b) for Maya crude oil (strain – see text, DGC-PA is the double gap cylinder – Peltier assembly, PP-ETC is the parallel plates – extended temperature cell): □, DGC-PA, $\omega = 0.63$ s^{-1}; △, DGC-PA, $\omega = 6.3$ s^{-1}; ○, DGC-PA, $\omega = 63$ s^{-1}; ■, PP-ETC, $\omega = 0.63$ s^{-1}; ▲, PP-ETC, $\omega = 6.3$ s^{-1}; ●, PP-ETC, $\omega = 63$ s^{-1}.

oscillation frequency. The greatest impact (up to 3 orders of magnitude) is observed at low temperatures where the complex viscosity has a plateau (temperature independent viscosity): below (260 to 280) K for Athabasca bitumen and below (230 to 240) K for Maya crude. Based on our previous study of the phase behavior of Maya crude,[2] the low-temperature plateau for complex viscosity can be attributed to a solid-continuous phase state. The solid to liquid maltene transition for Maya crude begins at approximately 170 K (from calorimetric measurements[2]) while the phase angle rises from 0° at (220 to 230) K (Figure 6.7b). A similar phase angle rise for Athabasca bitumen occurs at (250 to 260) K (Figure 6.2b). For the phase angle to rise, about 35 % liquid on volume basis must be present.[2] Complex viscosity only begins to decrease, once sufficient liquid is present for the fluid to flow, as is clear from a comparison between Figures 6.2a and 6.2b for Athabasca bitumen and Figures 6.7a and 6.7b for Maya crude. At a phase angle of 45°, there is approximately 50 % liquid and at 90° (at the upper plateau of phase angle), a minimum of 65 % liquid must be present.[2] At higher temperatures, Athabasca bitumen and Maya crude continue to behave as non-Newtonian shear-thinning fluids, but the impact of frequency on viscosity

128

values diminishes with increasing temperature. Maya crude becomes Newtonian at (280 to 285) K, i.e. viscosity becomes independent of frequency, whereas Athabasca bitumen exhibits moderate non-Newtonian character up to (310 to 315) K.

The rheological measurements in this work demonstrate that heavy oils and bitumen are non-Newtonian fluids at low temperatures. Their complex viscosities are sensitive to experimental conditions, and the viscosities of both hydrocarbon resources possess a temperature dependence, a frequency dependence, a dependence on thermal prehistory; and a time dependence (thixotropy). Two orders of magnitude variations in complex viscosity values are observed at low temperatures (less than ~270 K for Athabasca bitumen and less than ~240 K for Maya crude oil). Clearly, details of rheological measurements and sample history are important factors explaining the large reported variations for bitumen and heavy oil "viscosity" data.

6.3.3. Comparison of rheological results for Athabasca bitumen with literature data. The present results and literature values for the viscosity of Athabasca bitumen are presented in Figure 6.8. Differences between reported values range up to three orders of magnitude at fixed temperature. Variation is greatest at low temperatures and diminishes as temperature is increased.

Details of experiment. The viscosity data for Athabasca bitumen reported in Figure 6.8 were obtained using diverse viscometers including capillary flow, rotating cylinder, cone and plate, and rolling ball viscometers. Each measurement method is characterized by a range of shear conditions, that can differ from

129
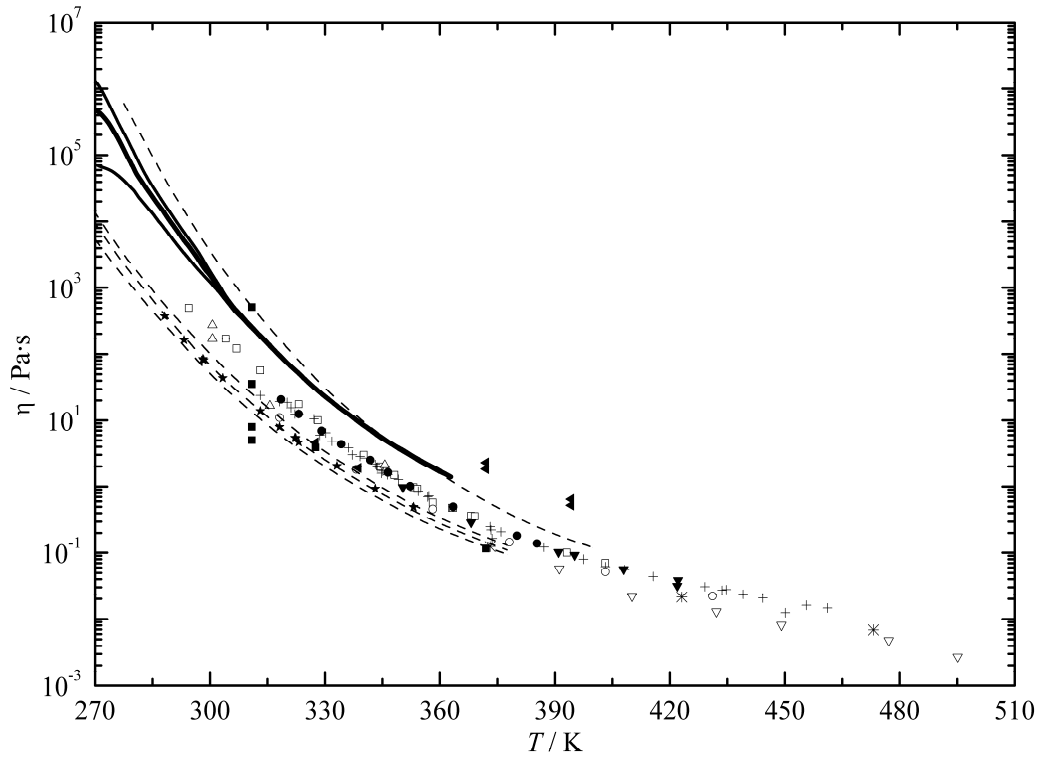
Figure 6.8. Viscosity variation for Athabasca bitumen with temperature: solid lines, PPV, ω = 0.63, 6.3, 63 and 630 s^{-1} (this work); dash lines, from different locations, CapV, γ' n/s (Ref. 5); ◀, method n/s, γ' n/s (Ref. 6); ■, from different locations, method n/s ; γ' n/s (Ref. 7); ○, CCV, γ' from 13 s^{-1} to 2300 s^{-1} (Ref. 8); ▽, RBV, γ' from 14 s^{-1} to 225 s^{-1} (Refs. 9, 10); [9,10]; ▼, CCV, γ' from 12 s^{-1} to 1400 s^{-1} (Refs. 9, 10); □, CCV, γ' n/s (Refs. 11, 12); +, CCV, γ' n/s (Ref. 13); △, MS, γ' = 1 s^{-1} (Ref. 14); ✳, CapV, γ' n/s (Ref. 15); ●, CCV, γ' is n/s (Ref. 16); ★, CCV, γ' = 460 s^{-1} (Ref. 17). Abbreviations and symbols: PPV, parallel plate viscometer; CapV, capillary viscometer; CCV, concentric cylinder viscometer; RBV, rolling ball viscometer; MS, mechanical spectrometer; n/s, not stated; γ', shear rate; ω, angular frequency (equivalent to shear rate).

sample to sample and among methods. For example, in the case of rotational viscometers the steady shear mode was used for all measurements reported in the literature.[8-14,16,17] In this study, oscillatory rheometry was performed. According to the Cox-Merz rule,[35] the complex viscosity $|\eta^*(\omega)|$ in an oscillatory experiment (where ω is the angular frequency, $\omega = 2\pi f$) is equivalent to the steady shear viscosity $\eta(\gamma')$ (where γ' is the shear rate) provided that $\omega = \gamma'$. Therefore, we can compare "oscillatory" viscosity values with "steady-shear" ones provided that we have information on the shear rate/frequency applied. As bitumen and heavy oil are shear-thinning fluids, "viscosity" has meaning only if the shear condition is clearly defined. For example, from Figures 6.2a and 6.3 only oscillatory frequency (or shear rate) has an influence on the viscosity of Athabasca bitumen. Most publications avoid direct reporting of the values of shear rate applied in their steady-shear measurements. Even if these parameters are given (Figure 6.8), they are essentially different for low and high temperatures (e.g., Refs. 8–10). Below 310 K, viscosity values obtained in this work approach the average of the previously reported range for viscosity data as long as a higher angular frequency is used. Thus, differences in shear rates can explain the discrepancies among viscosity values due to non-Newtonian behavior of Athabasca bitumen at least up to 310 K. Thermal irreversibility of viscosity for Athabasca bitumen, if heated above 360 K, due to slowly reversing or irreversible phase transitions in asphalthenes also play a role. Consequently, a thermal history of Athabasca bitumen before and during viscosity measurements is important since this can also lead to additional viscosity variation. In this work, viscosity was measured below

360 K, so the influence of thermal history during experiments was avoided. The absence of thermal history information (e.g. order of measurements) in Ref. 5-13, 15, 16 creates ambiguity in data interpretation even under conditions where bitumen exhibits Newtonian behavior and in principal all measurement methods should yield equivalent results.
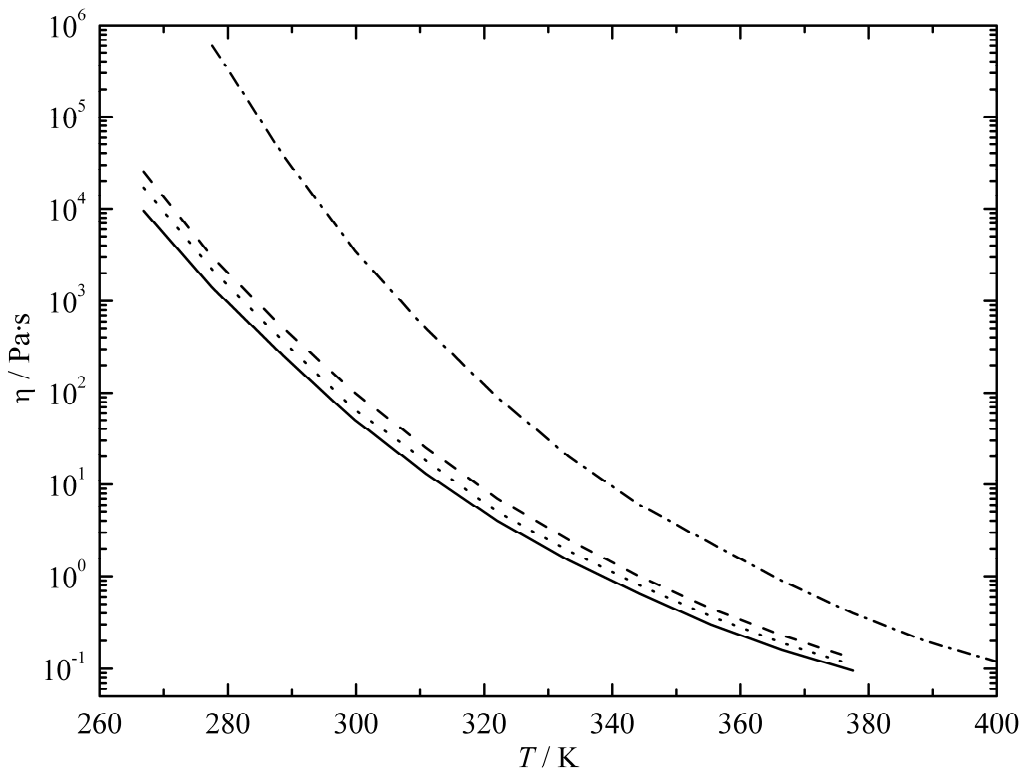
Figure 6.9. Temperature dependence of viscosity for Athabasca bitumen from different locations and elevations determined by Ward and Clark[5] (measurement method – capillary viscometry; recovery method – benzene-based extraction standardized for all samples; Bitumount #1 to #4 differ by 180 m elevation): solid line, Bitumount # 1; dashed line, Bitumount # 2, 3, and Ells River; dotted line, Bitumount # 4; dash-dotted line, Abasand.

Geographic location and depth within a reservoir. Ward and Clark[5] found that bitumen from Abasand has a viscosity up to three orders of magnitude higher than bitumen from more northern locations in the Athabasca region (Figure 6.9).

The variation with depth within a reservoir is less pronounced (less than one order of magnitude) but still appreciable and viscosity has a tendency to increase with depth. Ward and Clark[5] extracted all of their samples according to the same procedure, and used the same viscosity measurement technique (capillary viscometry) for all samples. One is tempted to conclude that the differences identified are attributable to sample source only, but the prevailing shear rate in the capillary is a function of the "viscosity". At low temperatures, the samples are not Newtonian, so differences among samples, though real, become exaggerated. Erno et al.[36], who used a cone and plate viscometer for viscosity experiments at 298 K at (1 to 10) s^{-1} shear rates, also found an increase of viscosity of heavy oils with depth within a well for different locations in Alberta (Canada).

Most publications do not include detailed information on bitumen origin, which restricts our ability to correlate viscosity with geographical origin and with elevation within a reservoir. A supplier but not the exact deposit and/or elevation is typically provided (e.g., Great Canadian Oil Sands Ltd.,[11–14] Syncrude Canada Ltd.,[8,17] Shell Canada Ltd. (one of the bitumen samples from Ref. 7), Abasand Oil Ltd.,[5] Research Council of Alberta,[6,21] etc.). Samples could be obtained directly from one location or could be blends from different deposits leased by the supplier. For example, the bitumen sample studied in this work could be a mixture

or an individual sample from Mildred Lake, Aurora and/or North Mine deposits – the main operation areas of Syncrude Canada Ltd. located between Abasand and Bitumount.

Production and post-production treatment procedure. From a chemical and structural point of view, bitumen in a deposit and materials produced from it are not identical, i.e. different production procedures yield bitumen with differing properties. This variation strongly depends on the production and post-production treatments.

Two methods are applied for producing bitumen from oil sands at the industrial scale – in-situ and mining processing schemes. In both, additional components are normally used for injection into wells or extraction from mined sands – water (or steam) or solvent. Hence, samples studied in this work or by other authors have undergone one of these two production procedures. In general, each additive has a well-known influence on viscosity. For example, the viscosity of bitumen usually increases when small amounts of water are added (up to 10 % to 40 %) while further addition reduces viscosity.[3,37] Solvent addition decreases viscosity.[3] From a practical perspective, post-production procedure variations can change fluid properties significantly. For example, if high temperature distillation is used in a naphtha-based production method,[7] light ends present in the bitumen are removed along with the naphtha. This increases the viscosity. At the same time, residual naphtha reduces viscosity.

Among the data from Figure 6.8, a mining + water and naphtha addition production procedure was used in Refs. 6, 17 and this work. A solvent-based one

was applied to samples in Refs. 5, 11–16. Based on information given in the references, solvent and water residues may be present in some cases.[6,14,15,17] There is no apparent trend in the viscosity values for bitumen exposed to these different production procedures. No extraction process was applied in Refs. 8–10 since the bitumen sample was obtained as it oozed from the mined tar sand[8] or by centrifugation through filter pads.[9,10] According to Henry and Fuhr[38] who ultracentrifuged oilsand samples without adding solvent, the Athabasca bitumen adhering to the sand grains was asphaltene deficient relative to the supernatant bitumen but the latter contained more light components, which are usually lost during solvent extraction procedure. They found that the viscosity of ultracentrifuged bitumen was the lowest and that of bitumen recovered by solvent extraction was the highest. Consequently it is not surprising that the viscosity for the samples obtained without adding solvent[8-10] fall below most of the data sets presented in Figure 6.8. Since the bitumen sample studied in this work was exposed to distillation at high temperatures between (523 and 623) K (removal of naphtha) following warm-water extraction, it is not surprising that its viscosity is higher than that of other samples treated under milder conditions – at 423 K[11-13,16] or at 308 K[14].

6.4. Conclusions

Maya heavy oil and Athabasca bitumen are shear thinning fluids over temperature ranges of industrial interest for production, storage, and transport. Complex viscosity must be associated with a specified shear condition in order for

reported viscosity values to have meaning. Up to three orders of magnitude variation in reported viscosity values for Athabasca bitumen can be attributed to the impact of shear as an uncontrolled variable in viscosity measurements. At elevated temperatures, bitumen and heavy oil approach Newtonian rheological behavior. Sample origin, production method and post-production treatments can also account for up to three orders of magnitude variation in measured viscosity values. By contrast, thermal and shearing history plays a secondary role. Variations, if present, fall within one order of magnitude, however, the effect of thixotropy for such complex fluids should be taken into consideration. A clear understanding of the variables affecting the rheological properties of bitumen and heavy oil is of crucial importance for selecting or optimizing flow regimes for their production and transport. Results reported here are expected to reduce the technical uncertainty related to the design and development of heavy oil and bitumen production and transport processes and to allow practitioners to discriminate real from phantom variables present in their own measurements and in the literature.

References

(1) *Alberta's Energy Reserves 2007 and Supply/Demand Outlook 2008-2016*; ERCB Document # ST98-2008; Energy Resources Conservation Board: Calgary, Canada, 2008.

(2) Fulem, M.; Becerra, M.; Hasan, M. D. A.; Zhao, B.; Shaw, J. M. Phase behaviour of Maya crude oil based on calorimetry and rheometry. *Fluid Phase Equilib.* **2008**, *272*, 32–41.

(3) Robinson, D. B. (ed.). *The thermodynamic and transport properties of bitumens and heavy oils*; AOSTRA Technical Report; Alberta Oil Sands Technology and Research Authority: Edmonton, Canada, 1984.

(4) Seyer, F. A.; Gyte, G. W. Viscosity. In *AOSTRA Technical Handbook on Oil Sands, Bitumens and Heavy Oils*; Hepler, L. G., Hsi C., Eds.; AOSTRA Technical Publication: Edmonton, Canada, 1989; pp. 155–184.

(5) Ward, S. H.; Clark, K. A. *Determination of the viscosities and specific gravities of the oils in samples of Athabasca bituminous sand*; Report 57; Research Council of Alberta: Edmonton, Canada, 1950.

(6) Charbonnier, R. P.; Draper, R. G.; Harper, W. H.; Yates, A. *Analyses and characteristics of oil samples from Alberta*; Information Circular IC 232; Canada Department of Energy Mines and Resources, Mine Branch: Ottawa, Canada, 1969; pp. 182–184.

(7) Camp, F. W. (Ed.). *The Tar Sands of Alberta, Canada*; 2nd ed.; Cameron Engineers Inc.: Denver, Colorado, 1974; p. 23.

(8) Flock, D. L.; Boogmans, T. *A laboratory investigation of steam solvent extraction of heavy oils and bitumen for in-situ application*; Final Report on AOSTRA Research Agreement 8, March 1978 (cited in Ref. 3).

(9) Briggs, J. P. *Summary of viscosity measurement data obtained during February and March 1978*; Alberta Research Council: Edmonton, Alberta, Canada, April 1978 (cited in Ref. 3).

(10) Briggs, J. P. *The measurement of bitumen viscosity at shear rates, temperatures and pressures which approximate to reservoir conditions*; Alberta Research Council: Edmonton, Alberta, Canada, June 1978 (cited in Ref. 3).

(11) Jacobs, F. A.; Donnelly, J. K.; Stanislav, J.; Svrcek, W. Y. Viscosity of gas-saturated bitumen. *J. Can. Pet. Technol.* **1980**, *19* (4), 46–50.

(12) Khan, M. A. B.; Mehrotra, A. K.; Svrcek, W. Y. Viscosity models for gas-free Athabasca bitumen. *J. Can. Pet. Technol.* **1984**, *23* (3), 47–53.

(13) Svrcek, W. Y.; Donnelly, J. K.; Stanislav, J. *Measurement, correlation and prediction of oil sand hydrocarbons*; Final Report on AOSTRA Research Agreement 13, June 1979 (cited in Ref. 3).

(14) Dealy, J. M. Rheological properties of oil sand bitumens. *Can. J. Chem. Eng.* **1979**, *57*, 677–683.

(15) Robinson, D. B.; Sim, S-K.; Chen, C-J. *The behavior of bitumen mixtures during in-situ recovery*; Final Report on AOSTRA Agreement 184, July 1983 (cited in Ref. 3).

(16) Mehrotra, A. K.; Svrcek, W. Y. Viscosity, density and gas solubility data for oil sand bitumen. Part I: Athabasca bitumen saturated with CO and C_2H_6. *AOSTRA J. Res.* **1985**, *1*, 263–268.

(17) Schramm, L. L.; Kwak, J. C. T. The rheological properties of an Athabasca bitumen and some bituminous mixtures and dispersions. *J. Can. Pet. Technol.* **1988**, *27* (1), 26–35.

(18) Fu, B. C. H. *An evaluation of mechanisms and criteria for solvent extraction of bitumen from Athabasca oil sand*; M.Sc. Thesis; University of Toronto, Department of Chemical Engineering and Applied Chemistry: Toronto, Ontario, Canada, 1978.

(19) Patel, M. S. *Determination of viscosities of oils from Mannville formation oil sand*; Research Council of Alberta: Edmonton, Alberta, Canada, October 1973 (cited in Ref. 3).

(20) Smolek, K. *Viscometric investigation of bitumen from Athabasca oil sands at subcracking temperatures and elevated pressures*; Alberta Research Council: Edmonton, Alberta, Canada, May 1976 (cited in Ref. 3).

(21) Mehrotra, A. K.; Svrcek, W. Y. Viscosity of compressed Athabasca bitumen. *Can. J. Chem. Eng.* **1986**, *64*, 844–847.

(22) Bowman, C. W. Molecular and interfacial properties of Athabasca tar sands. In *Proceedings of the 7th World Petroleum Congress, Mexico City*; Vol. 3; Elsevier: New York, 1967; pp. 583–604.

(23) Closmann, P. J.; Seba, R. D. Laboratory test on heavy oil recovery by steam injection. *Soc. Pet. Eng. J.* **1983**, *23*, 417–426.

(24) Nagra, S. S.; Armstrong, D. A.; Adam, F.C. Test for radiation fluidization of Athabasca tar sands. *Energy Processing/Canada* **1978**, *71*, 58–64.

(25) Bunger, J. W.; Thomas, K. P.; Dorrence, S. M. Compound types and properties of Utah and Athabasca tar sand bitumens. *Fuel* **1979**, *58*, 183–195.

(26) Fu, B. C. H.; Phillips, C. R. New technique for determination of diffusivities of volatile hydrocarbons in semi-solid bitumen. *Fuel* **1979**, *58*, 557–560.

(27) Rubinstein, I.; Strausz, O. P. Physical properties of conventional and biodegraded oils, *Am. Chem. Soc. Div. Fuel Chem. Preprints* **1977**, *22* (3), 20-25.

(28) Baughman, G. L. (Ed.). *Synthetic Fuels Data Handbook*; 2nd ed.; Cameron Engineers Inc.: Denver, USA, 1978; p. 274.

(29) Smith, N. A. C.; Smith, H. M.; Blade, O. C.; Garton, E. L. *The Bureau of Mines routine method for the analysis of crude petroleum, Part I: The analytical method*; Bulletin 490; U.S. Bureau of Mines: Washington, USA, 1951.

(30) Luo, P.; Gu, Y. Effects of asphaltene content on the heavy oil viscosity at different temperatures. *Fuel* **2007,** *86*, 1069-1078.

(31) Lin, M.-S.; Chaffin, J. M.; Davison, R. R.; Glover, C. J.; Bullin, J. A. A new suspension viscosity model and its application to asphaltene association thermodynamics and structures. In *Structures and Dynamics of Asphaltenes*; Mullins, O. C.; Sheu, E. Y., Eds.; Plenum Press: New York, 1998; p 267-302.

(32) Enbridge Pipelines Inc.: Crude oil characteristics http://www.enbridge.com/pipelines/about/operatingPipeline/crude-oil.php

(33) Zhang, Y.; Takanohashi, T.; Sato, S.; Saito, I.; Tanaka, R. Observation of glass transition in asphaltenes. *Energy Fuels* **2004**, *18*, 283-284.

(34) Zhang, Y.; Takanohashi, T.; Shishido, T.; Sato, S.; Saito, I.; Tanaka, R. Estimating the interaction energy of asphaltene aggregates with aromatic solvents. *Energy Fuels* **2005**, *19*, 1023-1028.

(35) Cox, W. P.; Merz, E. H. Correlation of dynamic and steady flow viscosities. *J. Polym. Sci.* **1958**, *28*, 619–622.

(36) Erno, B. P.; Chriest, J. R.; Wilson, R. C. Depth-related oil viscosity variation in Canadian heavy oil reservoirs. *J. Can. Pet. Technol.* **1991**, *30* (3), 38–41.

(37) Steinborn, R.; Flock, D. L. The rheology of heavy crude oils and their emulsions. *J. Can. Pet. Technol.* **1983**, *22* (5), 38–52.

(38) Henry, D.; Fuhr, B. Preparation of bitumen form oil sand by ultracentrifugation. *Fuel* **1992**, *71*, 1515-1518.

Chapter 7

Rheological Properties of Nanofiltered Athabasca Bitumen and Maya Crude Oil

MD. Anwarul Hasan, Michal Fulem, Ala Bazyleva, John M. Shaw

Abstract

Complex viscosities of permeate and retentate samples obtained by filtering Athabasca bitumen and Maya crude oil through 5, 10, 20, 50 and 200 nm ceramic filters at 473 K were investigated over the temperature interval 298 K to 373 K. The pentane-asphaltene content of the samples varied from 1.5 wt % to 57.2 wt % while the asphaltene free composition of the samples did not vary from the feed composition within experimental error. At temperatures below 323 K, part of the maltenes of both of these hydrocarbon resources is solid. The solid maltene fraction is a function of temperature. If this additional solid is taken into account, the experimental relative viscosities for both Athabasca bitumen and Maya crude related samples fall on a single master curve, over the entire temperature interval irrespective of asphaltene content. The rheological behavior of all feed, permeate and retentate samples is consistent with that of a slurry comprising a Newtonian liquid plus a dispersed solid comprising non-interacting hard spheres, where the solid fraction is the sum of the solid maltene plus asphaltene mass fractions. Failure to account for solid maltenes in the interpretation of rheological data for these hydrocarbon resources leads to misattributions related to the nature and the

importance of the role that asphaltenes play in the determination of the complex viscosity of these hydrocarbon resources.

Key words: bitumen; asphaltenes; viscosity; phase behavior; nanofiltration, multiphase

7.1. Introduction

Bitumen and heavy oils are poorly-characterized asphaltene-rich complex hydrocarbon mixtures which pose numerous challenges during production, transport and refining. [1] The high viscosity of these hydrocarbon resources is a key processing determinant which is frequently attributed to their asphaltene content and to asphaltene – maltene interactions. For example, Mack et al. [2] showed that the viscosity of a de-asphalted oil was up to several hundred times lower than the viscosity of mixtures comprising up to 20 vol.% asphaltenes + parent oil. Moreover, asphaltenes flocculate, aggregate, and sediment [3-5] even in aromatic solvents such as toluene, at concentrations as low as 100 mg/L. [6] Aggregation is linked to processing problems from formation damage and well plugging [7] to reactor and line coking to distillation tower plugging [8-14] to catalyst deactivation. [15] Improved understanding of asphaltenes, and their influence on the properties of bitumen and heavy oils would help solve many of these problems [16] and would facilitate development of more efficient processes

143

for production, transport and refining for these important hydrocarbon resources. [17]

The viscosity of bitumen and heavy oil is a key process variable for which data are available. [18] However, most of the available data focus on the dependence of viscosity on external factors such as pressure, temperature, and the presence of various additives, e.g.: diluents (benzene, toluene, n-decane, etc.) and dissolved gases (CO_2, N_2, CH_4, C_2H_6, etc). A few studies also consider the shear rate dependence of viscosity. Reported viscosity data [19-30] were obtained using various viscometers such as capillary flow, rotating cylinder, cone and plate, and rolling ball viscometers. In the case of rotational viscometers the steady shear mode was used for almost all measurements. [25-28] The impact of viscosity measurement techniques on the values of viscosity obtained is discussed in detail elsewhere. [31]

Investigations on the influence of asphaltenes on hydrocarbon resource viscosity have focused on model mixtures where chemically separated (solvent extracted) asphaltenes are added to standard organic solvents or to de-asphalted oil (maltenes) to obtain samples with a range of asphaltene concentrations. [32]

The aggregation of asphaltenes in various solvents has also been studied [33, 34, 7, 15]. Bouhadda et al. [33] found that aggregated asphaltene particles in toluene appear spherical for concentrations up to 15 vol.% and have an aggregation number of ~5. The results by Lorenz et al. [35] suggest that asphaltenes appear to be nearly spherical and non-solvated in mixtures with kerosene, gas oil, benzene

144

and decalin as well as in various lighter fractions of crude oil obtained through ultracentrifugation for concentrations ranging from 1 to 2 wt.%. Reerink [36] modeled asphaltene aggregates as oblate ellipsoids with a minor axis of about 1 nm and a major axis of about 5-9 nm and computed intrinsic viscosities in the range 5 to 8 where a value of 2.5 is consistent with rigid hard spheres. Using small-angle neutron scattering, Gawrys and Kilpatrick [37] showed that asphaltenes in mixed (toluene + methanol) or (toluene + heptane) solutions aggregate to form oblate cylinders. Takeshige [34] suggested that asphaltenes in benzene consist of double layers with semi axes of 3.19, 1.05 and 0.36 nm. Priyanto et al. [7] observed two distinct points of sharp change of slope in relative viscosity versus asphaltene concentration graphs, which they attributed to micellization phenomena. In a series of studies carried out at the Texaco Research Center, [38-43] asphaltenes obtained from five different sources yielded very similar rheological behavior indicating that the effect of shape and extent of solvation for those materials were quite similar. There is little agreement in the literature other than that asphaltenes appear to be particulate!

The phase behavior of heavy oils, apart from asphaltenes, is also complex. For example, Athabasca bitumen and Maya crude oil both comprise a minimum of three phases at 300 K – solid asphaltenes, liquid maltenes and solid maltenes. The phase behaviors of Maya crude oil [44] and Athabasca bitumen [45] are addressed in detail elsewhere. A key attribute relevant to the interpretation of rheological data presented here is that the maltenes of these feeds solidify – Figure 7.1.

The hypothesis tested in this work is whether taking into account the phase behavior of the maltenes, neglected in prior research, can reduce the ambiguity in the interpretation of the rheological behavior of asphaltenes in hydrocarbon resources. For example, Maya crude comprises 15.7 wt.% pentane insoluble asphaltenes. At 283 K, ~ 18 wt.% of the maltene fraction is also solid while at 325 K, the maltene fraction is liquid. [44] Without fore knowledge of this significant change in phase behavior, the rheological behavior and changes in rheological behavior in this temperature interval can be misinterpreted and misattributed. In
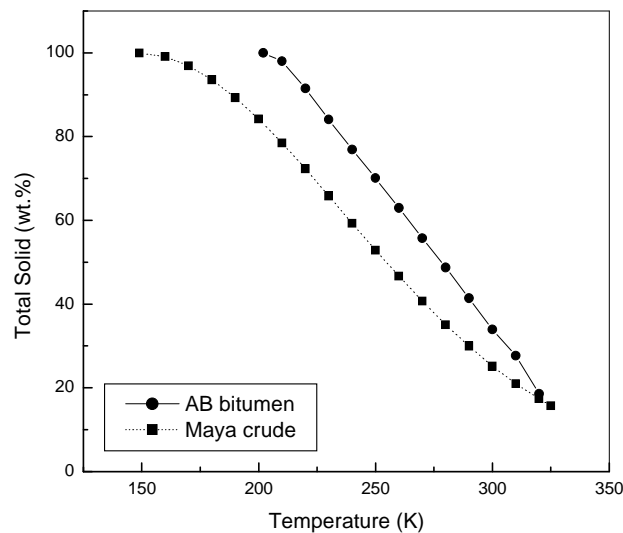
Figure 7.1. Total solid (wt.%) for Athabasca bitumen and Maya crude oil.

this contribution, the rheological behavior of Athabasca bitumen and Maya crude oil, along with their permeates and retentates obtained by solvent-free nano-filtration [46] are investigated. The results obtained are interpreted in light of the

146

underlying phase behavior of these samples and the theory related to the rheology of dispersions.

7.2. Rheological Response of Dispersions

A detailed review of the rheology of dispersions is beyond the scope of the present work. Readers are referred eleswhere. [47-51] For a dispersion of non-interacting uniform rigid spherical particles in a Newtonian fluid, relative viscosity can be predicted using various hard sphere models. [49-51] As the size, shape, size distribution, surface texture, of asphaltene particles and aggregates deviate from those of an ideal hard sphere, the relative viscosity of dispersions changes accordingly. Numerous empirical and semi-empirical models have been proposed to account for specific cases. [49-51] However, Sudduth [52] showed that many of these equations can be reduced to a single generalized form:

$$\ln(\eta/\eta_0) = \left(\frac{[\eta]}{k}\right)\left(\frac{1}{\sigma-1}\right)\left[(1-k\varphi)^{1-\sigma} - 1\right] \qquad (1)$$

Where η is the viscosity of dispersion, η_o is the viscosity of the continuous phase, $[\eta]$ is intrinsic viscosity, φ is the volume fraction of particles, k is the crowding factor, and σ is the particle interaction coefficient. In this paper the generalized Sudduth equation (eq. (1)) is used to interpret rheological data. This equation describes the behavior of Newtonian and non-Newtonian suspensions alike. The values of parameters are linked directly to fluid and particle physics theory. For

147

example, the intrinsic viscosity [η] for a slurry of spherical particles dispersed in a Newtonian fluid is 2.5; σ is 3.5 for non interacting hard spheres, and $1 < k < 2$. To make the best use of the theory related to relative viscosity, the volume or mass fraction of dispersed species in the crude and bitumen samples must be known accurately, and the liquid composition should be invariant. These aspects are both challenging because the solid mass fraction of the maltene varies with temperature. Hence, the solid free liquid composition varies with temperature, as does the average density of particles. The viscosity of the solid free continuous medium must be obtained by extrapolating experimental viscosity data to zero solids.

7.3. Experimental

7.3.1. Materials:

The Athabasca bitumen and Maya crude oil samples along with permeates and retentates obtained from nanofiltration experiments were available from a prior study, [46] where the apparatus, and sample preparation and analysis procedures are described in detail. SARA analyses are rehearsed in Tables 7.1 and 7.2 for convenience. For chemically separated maltenes, n-pentane, was added to bitumen / crude oil at a solvent to oil ratio of 40:1. The solution was stirred

Table 7.1. SARA analysis (wt. %) of Athabasca Bitumen Derived Samples [a]

	ABP10	ABP20	ABP50	AB	ABR200	ABR10
Saturates	18.9	18.4	17.1	16.1	9.4	8.9
	(20)*	(21)*	(20)*	(20)*	(20)*	(21)*
Aromatics	56.7	53.0	53.4	48.5	26.0	25.4
	(60)*	(59)*	(62)*	(60)*	(52)*	(59)*
Resins	19.1	18.2	15.9	16.8	14.6	8.7
	(20)*	(20)*	(18)*	(21)*	(29)*	(20)*
Asph.altenes (C5)	5.3	10.4	13.6	18.6	50.0	57.2

[a]ABP10: Athabasca bitumen 10 nm permeate; ABR10: Athabasca bitumen 10 nm retentate; ABP20: Athabasca bitumen 20 nm permeate; ABR200: Athabasca bitumen 200 nm retentate; ABP50: Athabasca bitumen 50 nm permeate.

* Data are on an asphaltene-free base, wt.%.

Table 7.2. SARA analysis (wt. %) of Maya Crude Oil Derived Samples [a]

	MP5	MP10	MP20	MP50	Maya crude	MR5
Saturates	39.6	34.4	34.1	31.7	31.6	16.9
	(40)*	(37)*	(37)*	(35)*	(38)*	(32)*
Aromatics	46.7	43.7	43.1	47.1	42.5	26.4
	(47)*	(47)*	(47)*	(52)*	(51)*	(50)*
Resins	12.3	15.7	14.8	11.8	10.2	10.0
	(12)*	(17)*	(16)*	(13)*	(12)*	(19)*
Asphaltenes (C5)	1.5	6.2	8.1	9.4	15.7	46.7

[a] MP5: Maya 5 nm permeate; MP10: Maya 10 nm permeate; MP20: Maya 20 nm permeate; MP50: Maya 50 nm permeate; MR5: Maya 5 nm retentate.

*Data are on an asphaltene-free base, wt.%.

overnight at room temperature and then filtered in two steps by vacuum filtration using a Fisher brand filter paper Q2, with a pore size between 1-5 µm, and then a 0.22 µm Millipore membrane (mix cellulose ester). The filtration membranes and the flask were washed with small volumes of n-pentane in order to eliminate residual oil. This step was repeated until the filtrate was colorless. The permeate was distilled to separate solvent from the maltenes.

7.3.2. Rheology Measurements:

Complex viscosity $|\eta^*|$ measurements were carried out using a Bohlin Gemini 200 HR Nano-Rheometer (Malvern Instrument, UK) over the temperature 298 K to 373 K. Two types of the measuring configurations were used:

1) parallel plate geometries with 25 mm and 40 mm diameters plates supplied with the extended temperature cell providing a temperature range of 123 K to 823 K with stability of $\pm$ 0.2 K; it was used in most of the experiments;

2) a double gap 24/27 mm concentric cylinder with the Peltier cylinder assembly allowing measurements from 253 K to 453 K with stability of $\pm$ 0.2 K. This latter geometry was used for very low viscosity samples, e.g. the chemically separated Maya maltene.

The thermocouple probe which reads the temperature of the bottom plate and hence indicates the temperature of the sample being sheared was calibrated to international temperature scale ITS 90 using a PT 100 resistance thermometer. The thermocouple in the Peltier cylinder was calibrated in the same way. In both cases, the uncertainty of temperature measurements was estimated to be $\pm$ 0.2 K.

In the double gap cylinder, the gap was fixed at the default value of 0.15 mm. For the parallel plate configuration, gaps of 0.85 mm, 1.0 mm and 1.6 mm were applied for highly viscous samples, e.g. Athabasca bitumen and retentates, whereas 0.20 mm or 0.45 mm were used for samples with intermediate viscosities (1.0 Pa·s to 500 Pa·s). These gaps were chosen based on test measurements on three different standard materials: Canon certified standard N2700000SP, PRA standard oil # 12, and PRA standard oil U0600. Viscosity measurements with the Canon certified viscosity standard N2700000SP (with viscosity of 1650 Pa·s at 310.5 K) were carried out to validate experimental conditions and parameter values selections for Athabasca bitumen. The conditions used for the Maya crude oil and permeates were validated using PRA standard oil # 12 and PRA standard oil U0600 with viscosities of 0.972 Pa·s and 0.1 Pa·s at 298 K respectively. The agreement with the recommended data was within 5%.

In order to ensure the consistency of the measurements obtained using different geometries, experiments were performed using more than geometry in the overlap range where geometries could be used interchangeably. Results agreed within experimental error. In some cases, experiments were repeated with more than one gap to ensure that the gap used was within appropriate limits. Artifacts related to "gap loading" were thus avoided.

The measurements were performed using the oscillatory shear method. The frequency of the oscillation was varied between 0.0001 Hz and 100 Hz depending on the sample. We use the term "frequency" in this paper, but it should be noted

that the frequency of oscillation is equivalent to the term shear rate used in steady shear experiments, when both are expressed in the same units, i.e.: the Cox-Merz rule ($|\eta^*(\omega)| = \eta(\dot{\gamma}=\omega)$) can be applied. All measurements were performed under nitrogen in order to avoid oxidation of the samples. For all experiments, an oscillation amplitude sweep test was performed first, at the lowest and the highest frequencies, to identify the stress and strain limits for the linear viscoelastic region, within which subsequent experiments were conducted.

7.4. Results and Discussion

7.4.1. Overview of Rheological Data for Athabasca Bitumen and Maya Crude Oil

The complex viscosity data obtained from oscillatory shear measurements at 298, 303, 323, 348 and 373 K are reported in Figures 7.2 (a) and (b) for Athabasca bitumen and in Figure 7.2 (c) for Maya crude oil. For low viscosity samples, the inertia effect becomes significant at high frequencies, which causes fluctuation and scatter in measured data. Therefore, complex viscosity data for the frequency range of 0.1 Hz to 100 Hz are only shown for highly viscous samples. Athabasca bitumen is about three orders of magnitude more viscous than Maya crude oil at 298 K. The viscosity of both materials is highly sensitive to temperature. A rise in temperature from 298 K to 373 K drops the viscosity of Athabasca bitumen and Maya crude by three orders of magnitude and two orders of magnitude,

respectively. Both Maya crude and Athabasca bitumen exhibit Newtonian plateaus at low shear rate over the entire temperature interval evaluated, although it is only evident at frequencies less than 0.01 Hz for Athabasca bitumen at 298 K – Figure 7.2 (b).
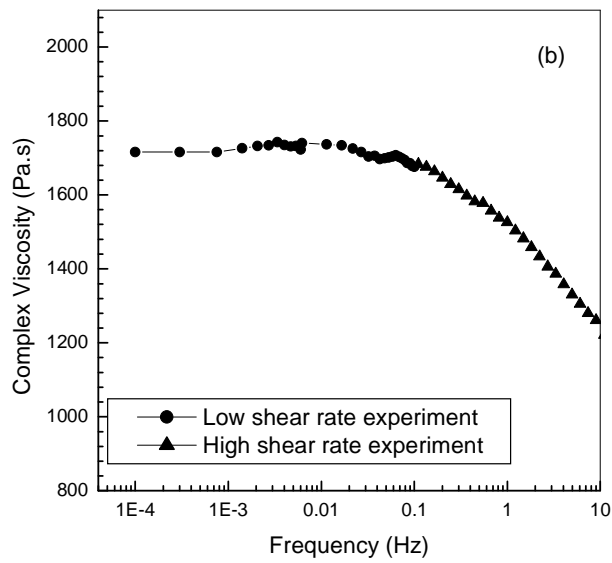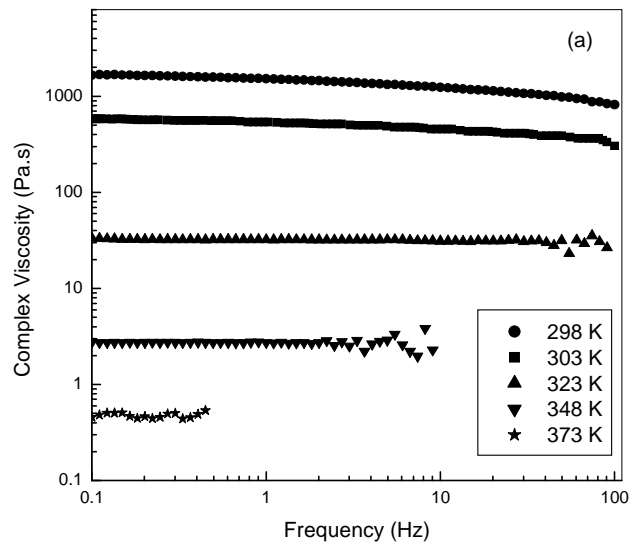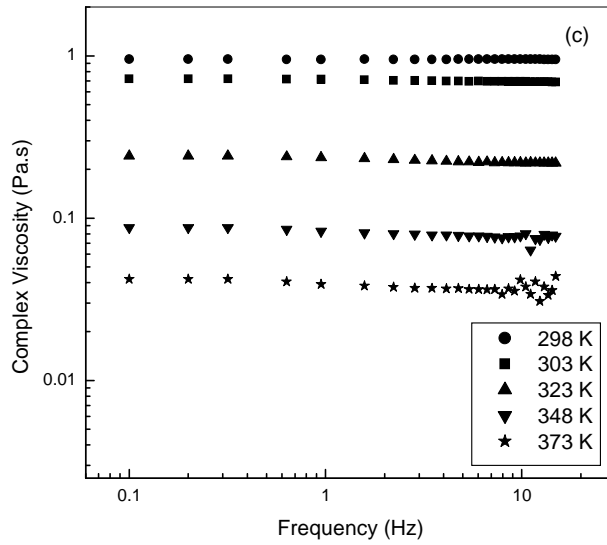
Figure 7.2. Complex viscosity for: (a) Athabasca bitumen summary, (b) Athabasca bitumen low frequency measurements at 298 K, and (c) Maya crude oil summary.

Figure 7.3 shows a comparison between zero shear complex viscosity values of Athabasca bitumen obtained in this study with apparent viscosity values, η, reported previously. [21-28] The complex viscosity values obtained in this study are higher except for values obtained by Ward and Clark [24] (Abasand), Charbonnier et al. [22] (for some locations) and Camp [21] (Abasand). This is because zero shear viscosities are by definition the highest values and because our bitumen sample is a partially processed product from a naphtha recovery unit at Syncrude. Some of the more volatile constituents of the bitumen have been removed. Differences in extraction and post-extraction
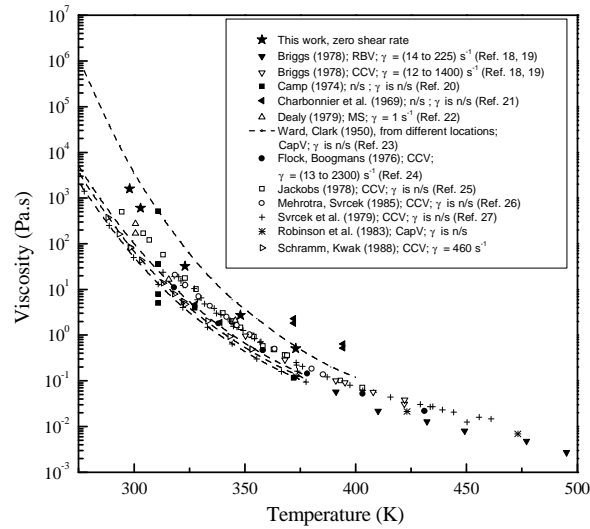
Figure 7.3. A comparison between the zero shear complex viscosity values for Athabasca bitumen obtained in this study with apparent viscosities of other studies in the literature.

processes, source location, measurement method and measurement operating parameter differences [31] can all account for significant differences in reported viscosity among samples.

7.4.2. Rheological Properties of Nanofiltered Permeates and Retentates

Rheological data for permeates at 298 K, the lowest temperature evaluated, are shown in Figures 7.4 (a) and (b) for Athabasca bitumen permeates and Maya crude oil permeates respectively. All permeates exhibit a Newtonian plateau at

low frequency. Rheological data for retentates, at 323 K, are shown in Figure 7.5 for both Athabasca bitumen retentates and Maya crude oil retentates. The complex viscosity for the retentates increases as the frequency decreases. Such a shear dependent behavior at low frequencies is typically observed when a gel type microstructure is present or when particles form a continuous network. At 298 K, Athabasca bitumen and Maya crude oil and their related permeates are both Newtonian, a particulate network is the more logical explanation for this non-Newtonian behavior of retentate samples. These results lend support for a colloidal structure for hydrocarbon resources first suggested without proof by Nellensteyn [53] decades ago.

Zero shear complex viscosity values for all permeate and retentate samples along with the resource samples are presented in Table 7.3. The zero shear viscosity for some retentate samples could not be measured and was estimated using the superposition principle. [54] These are noted with a dagger in Table 7.3. The complex viscosity, $\eta^*(\omega)$ is defined as $|\eta^*(\omega)|^2 = |\eta'(\omega)|^2 + |\eta''(\omega)|^2$, where $\eta'(\omega)$ is dynamic viscosity defined as $\eta' = G''/\omega$, and $\eta''(\omega)$ is the imaginary part of complex viscosity (resulting from the elastic component) defined as $\eta'' = G'/\omega$. The G'' is the viscous modulus, G' is elastic modulus and ω is the angular frequency. On the Newtonian plateau, the viscous component dominates, $\eta^*(\omega) \approx \eta'(\omega) \approx \eta_o$. So the zero-shear viscosity, η_o can be determined from the slope of G'' versus
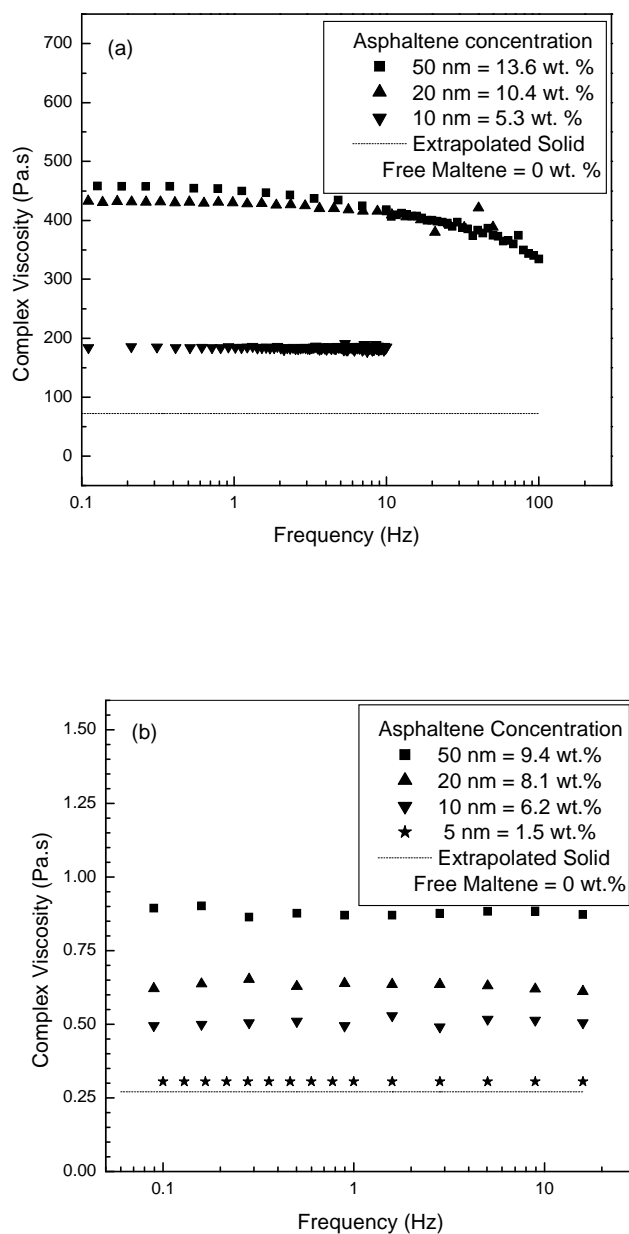
Figure 7.4. Complex viscosity for nanofiltered-permeate samples at 298 K: (a) Athabasca bitumen, and (b) Maya crude oil.

Table 7.3. Summary of Solid Concentrations, and Complex and Relative Viscosities of Samples.

Sample	Temperature K	asphaltenes[‡] (wt.%)	Solid maltene (wt.%)	Total solids (wt.%)	Zero shear complex viscosity (Pa·s)	Zero solid relative viscosity	Zero asphaltene relative viscosity	Chemically separated maltene based relative viscosity
ABP10	298	5.3	19.6	24.9	185	2.58	0.989	30.1
	323	5.3	0	5.3	5.63	0.776	0.777	8.78
	348	5.3	0	5.3	0.683	0.671	0.670	2.85
	373	5.3	0	5.3	0.189	1.02	1.02	2.70
ABP20	298	10.4	18.5	28.9	426	5.93	2.28	69.4
	323	10.4	0	10.4	11.7	1.61	1.61	18.3
	348	10.4	0	10.4	1.20	1.18	1.18	5.00
	373	10.4	0	10.4	0.244	1.31	1.31	3.48
ABP50	298	13.6	17.9	31.5	458	6.38	2.45	74.6
	323	13.6	0	13.6	11.9	1.64	1.64	18.6
	348	13.6	0	13.6	1.13	1.11	1.11	4.71
	373	13.6	0	13.6	0.305	1.64	1.64	4.35
AB (Bitumen)	298	18.6	16.8	35.4	1710	23.8	9.14	279
	303	18.6	13.4	32.0	581	13.2	6.81	161
	323	18.6	0	18.6	32.4	4.47	4.47	50.5
	348	18.6	0	18.6	2.72	2.67	2.67	11.3
	373	18.6	0	18.6	0.507	2.73	2.73	7.23
ABR200	298	50.0	10.3	60.3	$8.84 \cdot 10^{8\,†}$	$1.23 \cdot 10^7$	$4.73 \cdot 10^6$	$1.44 \cdot 10^8$
	323	50.0	0	50	$1.00 \cdot 10^{6\,†}$	$1.38 \cdot 10^5$	$1.38 \cdot 10^5$	$1.56 \cdot 10^6$

	348	50.0	0	50	$6.98 \cdot 10^3$ [†]	$6.85 \cdot 10^3$	$6.84 \cdot 10^3$	$2.91 \cdot 10^4$
	373	50.0	0	50	$3.20 \cdot 10^2$	$1.72 \cdot 10^3$	$1.72 \cdot 10^3$	$4.56 \cdot 10^3$
ABR10	323	57.2	0	57.2	$7.50 \cdot 10^5$ [†]	$1.03 \cdot 10^5$	$1.03 \cdot 10^5$	$1.17 \cdot 10^6$
	373	57.2	0	57.2	$3.80 \cdot 10^2$	$2.04 \cdot 10^3$	$2.04 \cdot 10^3$	$5.42 \cdot 10^3$
MP5	298	1.5	12.0	13.5	0.305	1.13	0.852	6.09
	303	1.5	8.9	10.4	0.210	0.961	0.631	5.20
	323	1.5	0.8	2.3	0.132	1.31	1.31	4.34
	373	1.5	0	1.5	$1.20 \cdot 10^{-2}$	0.574	0.574	
MP10	298	6.2	11.4	17.6	0.506	1.88	1.41	10.1
	303	6.2	8.4	14.6	0.318	1.45	0.955	7.87
	323	6.2	0.8	6.9	0.142	1.41	1.41	4.67
	373	6.2	0	6.2	$1.44 \cdot 10^{-2}$	0.689	0.689	
MP20	298	8.1	11.2	19.3	0.631	2.34	1.76	12.6
	303	8.1	8.3	16.4	0.420	1.92	1.26	10.4
	323	8.1	0.7	8.8	0.150	1.49	1.49	4.93
	373	8.1	0	8.1	$1.66 \cdot 10^{-2}$	0.794	0.794	
MP50	298	9.4	11.0	20.4	0.879	3.26	2.46	17.5
	303	9.4	8.2	17.5	0.445	2.04	1.34	11.0
	323	9.4	0.7	10.1	0.170	1.69	1.69	5.59
	373	9.4	0	9.4	$1.77 \cdot 10^{-2}$	0.847	0.847	
Maya Crude	298	15.7	10.2	25.9	0.954	3.54	2.66	19.0
	303	15.7	7.6	23.3	0.701	3.21	2.11	17.4
	323	15.7	0.7	16.4	0.225	2.23	2.23	7.40
	348	15.7	0	15.7	$7.90 \cdot 10^{-2}$	1.82	1.82	3.00
	373	15.7	0	15.7	$3.90 \cdot 10^{-2}$	1.87	1.87	
MR5	323	46.7	0.4	47.1	$6.87 \cdot 10^4$ [*]	$6.82 \cdot 10^5$	$6.82 \cdot 10^5$	$2.26 \cdot 10^6$

‡ Phase angle and calorimetric measurements for neat asphaltenes suggest that while phase

transitions to liquid begin at lower temperatures, asphaltenes are largely solid up to 373 K

† Zero shear viscosity for these samples was obtained using the superposition approach.

* For MR5 retentate, viscosity was available at one temperature. This value was obtained at 0.01

Hz and is not a zero shear value.

Table 7.4. Zero Shear Reference Viscosities (Pa·s)

T, K	Athabasca bitumen			Maya crude oil		
	extrapolation solids free	extrapolation 0 % asphaltenes	maltenes measurement (chemical separation)	extrapolation solids free	extrapolation 0% asphaltenes	Maltenes measurement (chemical separation)
298	71.8	187	6.14	0.270	0.358	0.0501
303	44.1	85.3	3.60	0.219	0.333	0.0404
323	7.25	7.25	0.641	0.101	0.101	0.0304
348	1.02	1.02	0.240	0.0434	0.0434	0.0266
373	0.186	0.186	0.0701	0.0209	0.0209	
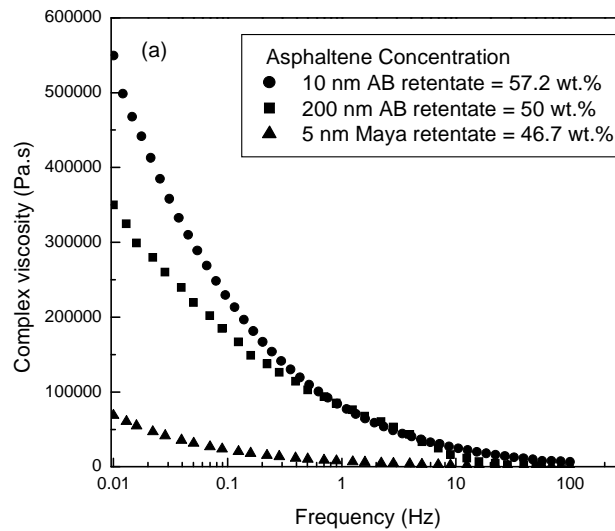
Figure 7.5. Complex viscosity values for Athabasca bitumen and Maya crude oil retentates at 323 K.

ωa_T master curve (a_T is a shift factor) constructed by shifting G'' curves at different temperatures along ω axis. G'' master curves were obtained for retentate samples where possible. Figure 7.6 (a) shows the viscous modulus (G'') for the Athabasca bitumen 200 nm retentate sample at different temperatures. The G'' master curve for this case, illustrating the method for obtaining the zero shear viscosity for the 200 nm retentate sample at 298 K is shown in Figure 7.6 (b). A terminal zone (constant slope regime) is clearly visible at very low frequencies in the G'' master curve. A tangent line is drawn in the terminal zone of the master curve, and is extended until it intersects the vertical line at $\omega a_T = 1$. The G'' value at this
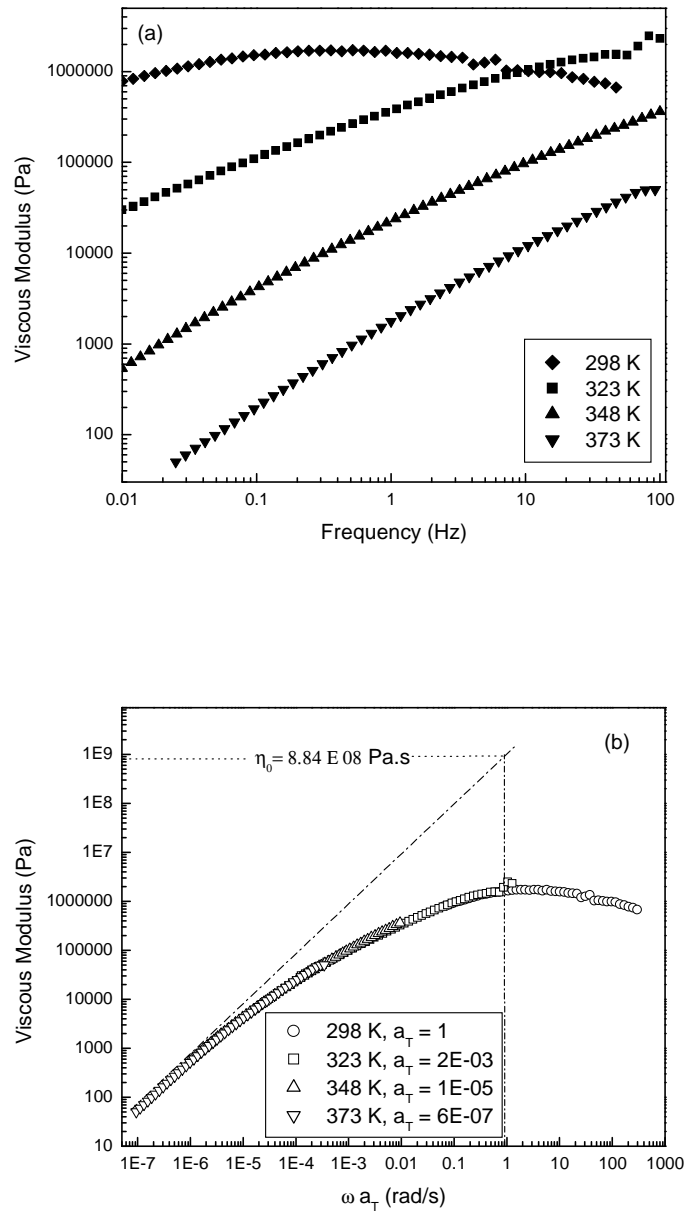
Figure 7.6. (a) Viscous modulus data for Athabasca bitumen 200 nm retentate,

(b) viscous modulus master curve used to estimate the zero shear viscosity at 298

K (a_T is the shift factor).

intersection point gives the zero shear viscosity of the sample. A key assumption in this calculation is that the composition of the liquid is invariant. As we are extrapolating into the low temperature region where part of the maltene solidifies, the values obtained are viewed as tentative and are not used in the modeling work.

7.4.3. The Impact of Solid Maltenes on the Viscosity of Athabasca Bitumen and Maya Crude Oil

The solid-liquid transitions for both Athabasca bitumen and Maya crude oil maltenes take place over broad temperature ranges, from ~160 K to 325 K for Maya crude maltenes, and from ~ 210 K to 323 K for Athabasca bitumen maltenes. [44, 45] 16.8 % and 10.2 %, respectively, of Athabasca bitumen and Maya crude maltenes are solid at 298 K. Asphaltenes are also solid at 298 K and the total solid mass fractions for Athabasca bitumen and Maya crude at 298 K are 35.4% and 25.9% respectively as shown in Figure 7.1. This effect complicates the interpretation of rheological data, as the solid content, solid density and the composition of the solid free maltene in permeate, resource and retentate samples, are functions of temperature below 323 K. From calorimetric data [44, 45] Maya and Athabasca asphaltenes begin to melt at about 340 K. However, the phase angle for pentane asphaltenes does not start to increase from zero degrees until around 380 K, indicating that up to this temperature asphaltenes comprise a minimum of 65 % solids. Moreover, asphaltenes remain filterable from maltenes at 473 K. [46] Clearly, liquid asphaltenes remain part of the dispersed solid asphaltene particles at 473 K. The structure of the two phase particles is unknown.
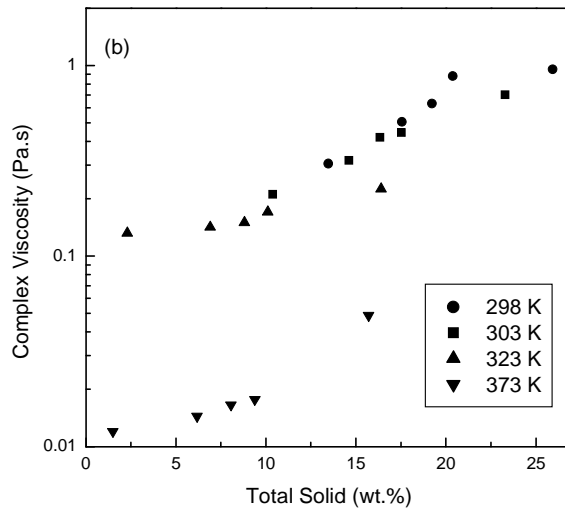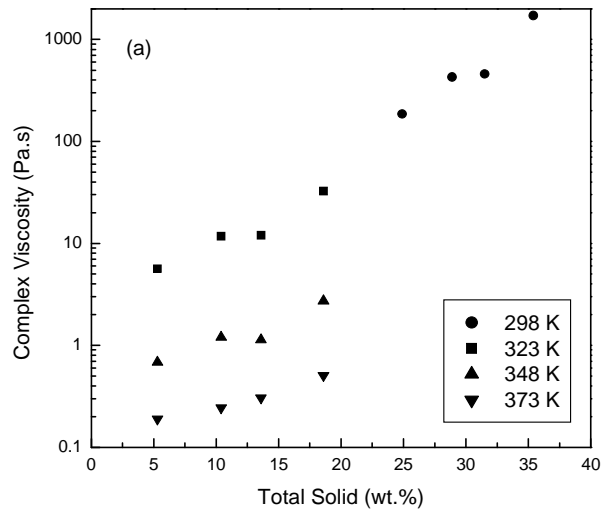
Figure 7.7. Zero shear complex viscosity as a function of sample solid content: (a) Athabasca bitumen and (b) Maya crude oil related samples.

In this study we assume the particles are solid continuous. The solid maltene, asphaltene and total solid wt. % along with zero shear complex viscosities of samples are summarized in Table 7.3. The zero shear complex viscosities of permeate samples are reported in Figures 7.7 (a) and (b) for Athabasca bitumen and Maya crude oil related samples respectively. Temperature is a parameter.

To estimate the viscosity of the solid free Athabasca maltene and Maya crude oil maltene, the experimental viscosity values for permeates and resource samples were fitted with the generalized Sudduth model, equation 1, and the Arrhenius equation:

$$\eta_o = Ae^{(E/RT)} \tag{2}$$

where A is the pre-exponential factor, E is the activation energy of viscous flow for solid-free maltene, R is the universal gas constant, and T is absolute temperature. Taking intrinsic viscosity $[\eta] = 2.5$ and the particle interaction coefficient, $\sigma = 3.5$, the best fit was obtained for $k = 1.38$ with $A = 9.69 \cdot 10^{-12}$ Pa·s and $E = 73.5$ kJ·mol^{-1} for Athabasca bitumen samples, and $A = 8.05 \cdot 10^{-7}$ Pa·s and $E = 31.5$ kJ·mol^{-1} for Maya crude samples. The values of the activation energy are in good agreement with literature values [55-60], which lie mainly between 10 kJ·mol^{-1} and 80 kJ·mol^{-1} depending on the viscosity, asphaltene concentration and mixture homogeneity of the oil. For example, Ronningsen et al. [55] found the activation energy of a number of North Sea crude oil samples, with viscosity lying

between 3.7 mPa·s and 155 mPa·s (at 293 K), to lie in the range 10 to 40 kJ·mol^{-1}. For crude oils with viscosity from 0.135 Pa·s to 2.24 Pa·s (at 293 K), [56] activation energy was about 20 kJ·mol^{-1}. For the Cold Lake and Lloydminster oil samples with viscosities of about 100 Pa·s (at about 295 K) [57] and 0.3 to 50 Pa·s (at 293 K), [58] activation energy are 80 kJ·mol^{-1} and 60 to 80 kJ·mol^{-1}, respectively. The extrapolated solid free maltene viscosity values for Athabasca bitumen and Maya crude oil are listed in Table 7.4. These viscosity values are higher than the viscosities of chemically separated maltenes also shown in Table 7.4, due to the presence of residual solvents in the chemically separated maltene samples.

Experimental zero solid relative viscosity values (defined as the zero shear complex viscosity divided by the solid free maltene viscosity) for the Athabasca bitumen and Maya crude oil samples along with those of their permeates are also shown in Table 7.3 and are plotted in Figures 7.8 (a) and (b) respectively. The zero solid relative viscosities for all samples are shown in Figure 7.8 (c). The relative viscosities of all permeates, feeds and retentate samples fall on a single master curve. Sudduth's correlation [52] (equation 1) with $[\eta] = 2.5$; $\sigma = 3.5$; and $k = 1.38$, is also shown in Figure 7.8 (c). There are two types of solids present. Their individual densities are unknown a priori. Differences between solid wt.% and vol.% are accommodated in the value of the crowding factor, k,
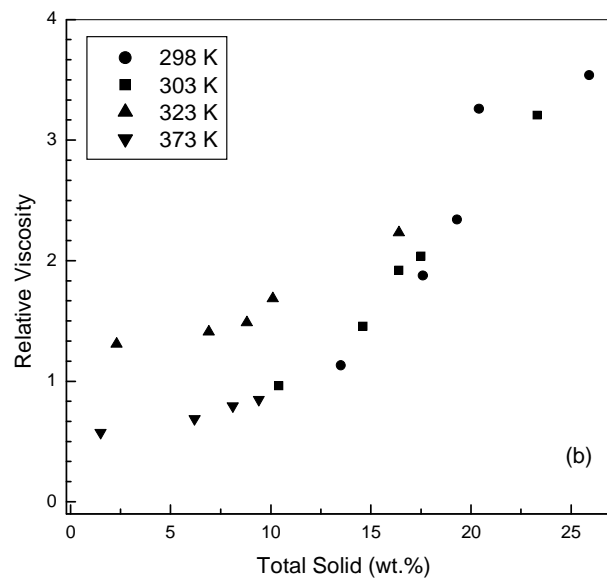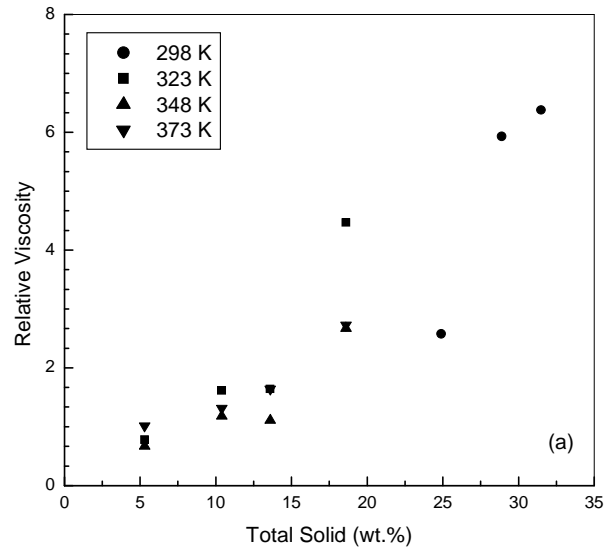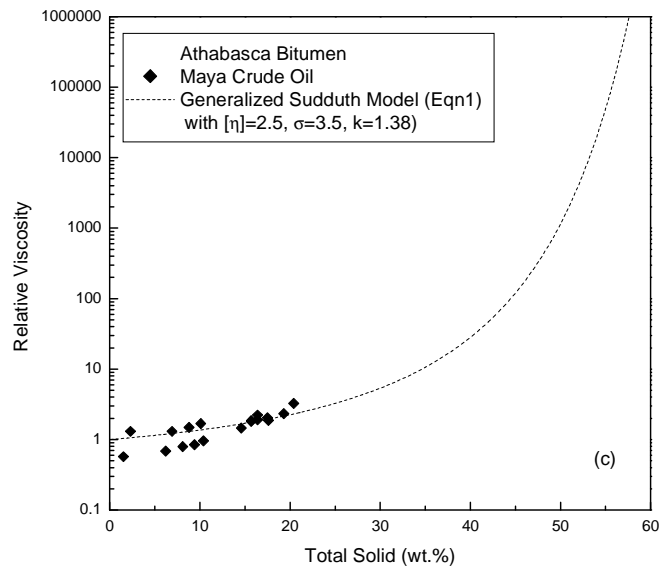
Figure 7.8. Zero-shear zero-solid relative viscosities: (a) Athabasca bitumen permeates, (b) Maya crude permeates, (c) all data.
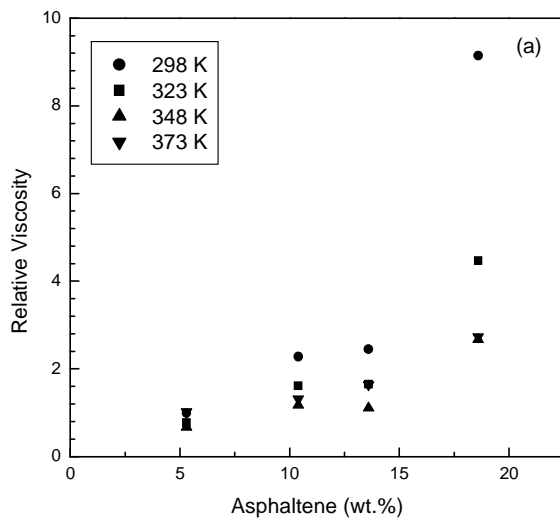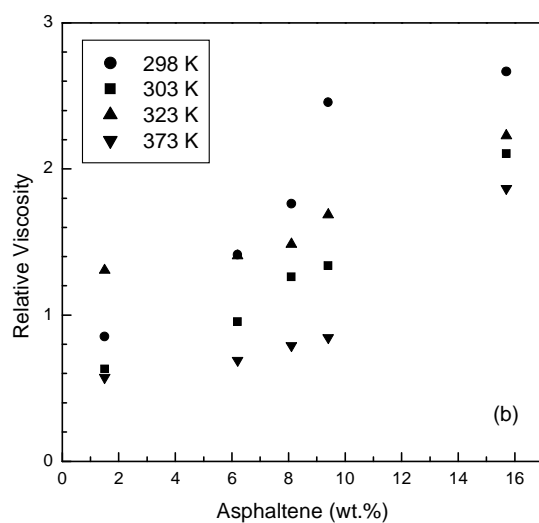
Figure 7.9. Zero-shear, zero-asphaltene relative viscosities: (a) Athabasca bitumen permeates, (b) Maya crude permeates.

which is the only parameter adjusted in the model. Both types of solids are expected to be denser than the liquid maltenes. As the crowding factor appears twice in equation 1, this represents a compromise. One could add additional parameters in the denominator for each feed but this is not justified by the data. The rheological behaviors of Athabasca bitumen and Maya crude oil-feeds, retentates and permeates are consistent with the behavior of slurries comprising a Newtonian liquid plus rigid hard spheres in the temperature range 298 K to 373 K. Some of the relative viscosities fall below 1. This reflects the combined impact of experimental error and extrapolation to zero solids content.

If the impact of solid maltene is ignored, one is confronted with significant apparent temperature dependences for relative viscosities at fixed asphaltene wt.%

170

at temperatures where the maltenes are partially solid. For example, a zero asphaltene reference viscosity can be obtained using equation 1, evaluated at the wt. % solid maltene in a sample. Reference viscosities for this case are reported in Table 7.4 and relative viscosity values obtained are plotted against wt. % asphaltenes in Figure 7.9. Apparent temperature dependence is evident for Athabasca bitumen related samples, Figure 7.9 (a). For Maya crude oil related samples, Figure 7.9 (b), the impact is less pronounced because less of the maltene is solid. An alternative relative viscosity can also be defined using measured chemically separated maltene viscosity as the reference viscosity. Reference viscosities for this case are also shown in Figure 7.4. Relative viscosities are reported in Tables 3 and plotted in Figures 7.10 (a) and (b) for Athabasca bitumen and Maya crude oil related samples respectively. Again, the apparent temperature dependence of rheological behavior is significant. These apparent temperature dependences have been attributed to
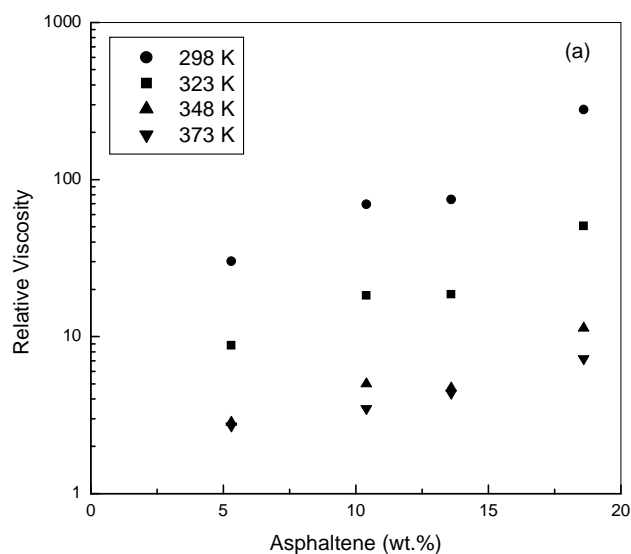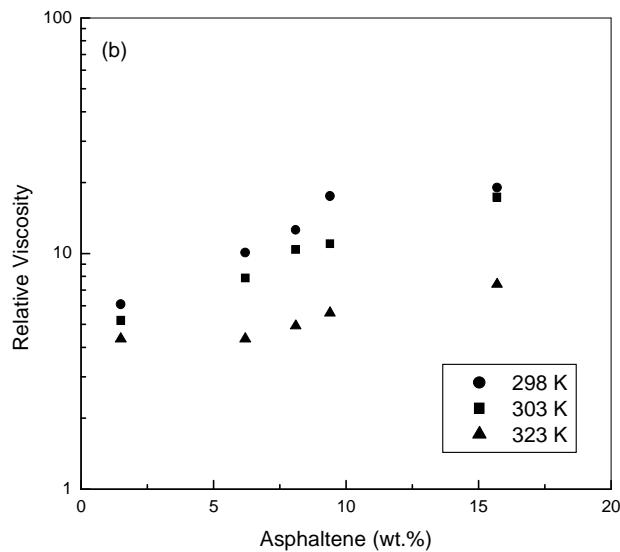
Figure 7.10. Zero-shear, chemically separated maltene-based relative viscosities: (a) Athabasca bitumen permeates, (b) Maya crude permeates.

change of shape of asphaltene aggregates, asphaltene-maltene interaction, or asphaltene self association [56, 58, 61]. These appear to be misattributions based on artifacts, and measured variables that introduce additional fluid physics and fluid chemistry not needed to explain the rheological behavior of such fluids. Rheological investigations of hydrocarbon resources must account for the impacts of solid maltenes along with the asphaltenes in modeling and analysis.

7.5. Conclusions

Hydrocarbon resources such as Athabasca bitumen and Maya crude oil possess complex phase behaviors and present equally complex rheological properties. The

impact of non-asphaltenic solids, on the complex viscosity of hydrocarbon resource samples at specific temperatures and on trends with temperature, is underscored in this contribution. Solid maltenes are shown to play a crucial role in determining the rheological properties of bitumen and heavy oil. Permeates, retentates and feeds associated with nanofiltered Maya crude oil and Athabasca bitumen exhibit rheological behaviors consistent with slurries comprising a Newtonian liquid + non-interacting hard spheres in the temperature range 298 K to 373 K when the role of solid maltenes is included. Failure to account for solid maltenes in the interpretation of rheological data for these hydrocarbon resources leads to misattributions related to the nature and the importance of the role that asphaltenes play in the determination of hydrocarbon resource viscosity.

References

[1] A.G. Mazza, Modelling of the liquid-phase thermal cracking kinetics of athabasca bitumen and its major chemical fractions, (Ph.D.), University of Toronto, Canada, 1987.

[2] C. Mack, J. Phys. Chem. 36 (1932) 2901.

[3] V.A.M. Branco, G.A. Mansoori, L.C. De Almeida Xavier, S.J. Park, H. Manafi, Asphaltene flocculation and collapse from petroleum fluids, J. Pet. Sci. Eng. 32 (2001) 217-230.

[4] J. Murgich, O.P. Strausz, Molecular mechanics of aggregates of asphaltenes and resins of the athabasca oil, Pet. Sci. Technol. 19 (2001) 231-243.

[5] H.W. Yarranton, Asphaltene self-association, J. Dispersion Sci. Technol. 26 (2005) 5-8.

[6] G. Andreatta, N. Bostrom, O.C. Mullins, High-q ultrasonic determination of the critical nanoaggregate concentration of asphaltenes and the critical micelle concentration of standard surfactants. , Langmuir 21 (2005) 2728-2736.

[7]   S. Priyanto, G.A. Mansoori, A. Suwono, Measurement of property relationships of nano-structure micelles and coacervates of asphaltene in a pure solvent, Chem. Eng. Sci. 56 (2001) 6933-6939.

[8] R.S. Taylor, P.S. Stemler, A. Lemieux, G.C. Fyten, A. Cheng, Prevention of refinery tower plugging by residual oil gellant chemicals in crude-pilot plant evaluation of alternative oil gellants. 7th Canadian International Petroleum Conference, Calgary, Alberta, Canada, 2006, pp. Paper 053.

174

[9] P.M. Licha, L. Herrera, Electrical and other effects related to the formation and prevention of asphaltenes deposition., Soc. pet. Eng. j. Paper 5304 (1975).

[10] J. Escobedo, G.A. Mansoori, Viscometric principles of onsets of colloidal asphaltene flocculation in paraffinic oils and asphaltene micellization in aromatics., SPE Prod. Facil. (1997) 116-122.

[11] G.D. Holder, R.M. Enick, R.S. Mohamed, Fluid Phase Equil. 117 (1996) 126-137.

[12] M.M. Sharma, T.F. Yen, G.V. Chilligarian, E.C. Donaldson, Some chemical and physical problems in enhanced oil recovery opzrations Development in Petroleum Science, New York, 1985, pp. 223-249.

[13] M.P. Licha, Oil Sands (1977) 609-624.

[14] I.C. Jacobs, M.A. Thorne, SPE Paper No. 14823 (1986).

[15] E.Y. Sheu, Petroleum asphaltene-properties, characterization, and issues, Energy & Fuels 16 (2002) 74-82.

[16] R.S. Mohamed, A.C.S. Ramos, W. Loh, Aggregation behavior of two asphaltenic fractions in aromatic solvents, Energy & Fuels 13 (1999) 323-327.

[17] R.E. Baltus, Characterization of asphaltenes and heavy oils using hydrodynamic property measurements. in: O. C. Mullins, and E. Y. Sheu, (Eds.), Structures and dynamics of asphaltenes. Plenum Press, New york and London, pp. 303-335.1998.

[18] F.A. Seyer, G.W. Gyte, "Viscosity", chapter 4 in aostra technical handbook on oil sands, bitumens and heavy oils. In: L. E. Hepler, and C. Hsi, (Eds.), Aostra technical publication series. AOSTRA Technical Publication, Alberta, 1989.

[19] J.P. Briggs, The measurements of bitumen viscosity at shear rates, temperatures and pressures which approximate to reservoir conditions. Alberta Research Council, Edmonton, Alberta, Canada,, 1978.

[20] J.P. Briggs, Summary of viscosity measurements data obtained during february and march 1978. Alberta Research Council, Edmonton, Alberta, Canada,, 1978.

[21] F.W. Camp, The tar sands of alberta, canada In: F. W. Camp, (Ed., The tar sands of alberta, canada Cameron Engineers Inc., 1976.

[22] R.P. Charbonnier, R.G. Draper, W.H. Harper, A. Yates, Analyses and characteristics of oil samples from alberta, . Canada Department of energy mines and resources, Mine Branch pp. 182-184 1969.

[23] J.M. Dealy, Rheological properties of oil sand bitumens, Can. J. Chem. Eng. 57 (1979) 677-683.

[24] S.H. Ward, K.A. Clark, Determination of the viscosities and specific gravities of the oils in samples of athabasca bituminous sand. Research Council of Alberta 1950.

[25] D.L. Flock, T. Boogmans, A laboratory investigation of steam solvent extraction of heavy oils and bitumen for in-situ application, final report on aostra research agreement8, , 1978.

[26]   F.A. Jacobs, Viscosity of carbon dioxide saturated athabasca bitumen University of Calgary Calgary, 1978.

[27]   A.K. Mehrotra, W.Y. Svrcek, Viscosity, density and gas solubility data for oil sand bitumen. Part i: Athabasca bitumen saturated with co and c2h6, AOSTRA J. Res. 1 (1985) 263-268.

[28]   W.Y. Svrcek, J.K. Donnelly, J. Stanislav, Measurement, correlation and prediction of oil sand hydrocarbons, final report on aostra research agreement 13, 1979.

[29]   D.B. Robinson, S.-K. Sim, C.-J. Chen, The behavior of bitumen mixtures during in-situ recovery, final report on aostra agreement 184, 1983.

[30]   L.L. Schramm, J.C.T. Kwak, The rheological properties of the athabasca bitumen and some bituminous mixtures and dispersion, J. Can. Pet. Tech. 27 (1988) 26-35.

[31]   A. Bazyleva, M.A. Hasan, M. Fulem, M.S. John, Bitumen and heavy oil rheological properties-reconcilliation with viscosity measurements, Journal of Chemical Engineering Data Submitted (2009).

[32]   J. Marques, Hydrocraquage catalytique des asphaltenes pour l'hydrotraitement de residus en lit fixe, (Ph. D.), Docteur De L'Universite De Poitiers, Lyon, 2006.

[33]   Y. Bouhadda, D. Bendedouch, E. Sheu, A. Krallafa, Some preliminary results on a physico-chemical characterization of a hassi messaoud petroleum asphaltene, Energy & Fuels 14 (2000) 845-853.

[34]   W. Takeshige, Hydrodynamic shape and size of khafji asphaltene in benzene, J. Colloid Interface Sci. 234 (2001) 261-268.

[35] P.B. Lorenz, R.J. Bolen, H.J. Dunning, I.A. Eldib, J. Colloid. Sci. 16 (1961) 493.

[36] H. Reerink, Ind. Eng. Chem. Prod. Res. Develop. 12 (1973) 82

[37]   K.L. Gawrys, P.K. Kilpatrick, Asphaltenic aggregates are polydisperse oblate cylinders, J. Colloid Interface Sci. 288 (2005) 325-334.

[38] D.A. Storm, R.J. Baressi, E.Y. Sheu, Rheological study of ratawi vacuum residue in the 298-673 k temperature range, Energy & Fuels 9 (1995) 168-176.

[39] E.Y. Sheu, M.B. Shields, D.A. Storm, Viscosity of base-treated asphaltene solutions, Fuel 73 (1994) 1766-1771.

[40] D.A. Storm, E.Y. Sheu, Rheological studies of ratawi vacuum residue at 366 k, Fuel 72 (1993) 233-237.

[41] E.Y. Sheu, M.M. De Tar, D.A. Storm, Rheological properties of vacuum residue fractions in organic solvents, Fuel 70 (1991) 1151-1156.

[42] D.A. Storm, R.J. Barresi, S.J. Decanio, Colloidal nature of vacuum residue, Fuel 70 (1991) 779-782.

[43]   D.A. Storm, E.Y. Sheu, M.M. Detar, R.J. Barresi, A comparison of the macrostructure of ratawi asphaltenes in toluene and vacuum residue, Energy & Fuels 8 (1994) 567-569.

[44] M. Fulem, M. Becerra, M.A. Hasan, B. Zhao, J.M. Shaw, Phase behaviour of maya crude oil based on calorimetry and rheometry, Fluid Phase Equilib. 272 (2008) 32-41.

[45] M.A. Hasan, M. Fulem, M. Becerra, B. Zhao, J.M. Shaw, Phase behaviour of athabasca bitumen based on calorimetry and rheometry, Fluid Phase Equilib. In Progress (2009).

[46] B. Zhao, J.M. Shaw, Composition and size distribution of coherent nanostructures in athabasca bitumen and maya crude oil, Energy & Fuels 21 (2007) 2795-2804.

[47] A. Einstein, A new determination of the molecular dimensions, Annalen Der Physik 19 (1906) 289-306.

[48] A. Einstein, A new determination of the molecular dimensions (vol 19, pg 289, 1906), Annalen Der Physik 34 (1911) 591-592.

[49] G.K. Batchelor, The stress system in a suspension of force-free particles, J. Fluid Mech. 41 (1970) 21.

[50] G.K. Batchelor, Effect of brownian motion on bulk stress in a suspension of spherical-particles, J. Fluid Mech. 83 (1977) 21.

[51] G.K. Batchelor, J.T. Green, The determination of the bulk stress in a suspension of spherical-particles to order c^2, J. Fluid Mech. 56 (1972) 401-427.

[52] R.D. Sudduth, A generalized model to predict the viscosity of solutions with suspended particles. I, J. Appl. Polym. Sci. 48 (1993) 25-36.

[53]   F.J. Nellensteyn, The colloidal structure of bitumen, Delft Technical Universtiy, 1923.

[54]   M.V. Gurp, J. Palmen, Time-temperature superposition for polymeric blends, Rheology Bulletin 67 (1998) 5-8.

[55]   H.P. Ronningsen, B. Bjorndal, A.B. Hansen, W.B. Pedersen, Wax precipitation from north sea crude oils. 1. Crystallization and dissolution temperatures, and newtonian and non-newtonian flow properties, Energy & Fuels 5 (1991) 895-908.

[56] M.V. Kök, J. Letoffe, P. Claudy, Dsc and rheometry investigations of crude oils, J. Therm. Anal. Calorim. 56 (1999) 959-965.

[57] J. Bryan, A. Kantzas, C. Bellehumeur, Oil-viscosity predictions from low-field nmr measurements, SPE 89070, SPE Res. Eval. Eng 8 (2005) 44-52.

[58] P. Luo, Y. Gu, Effects of asphaltene content on the heavy oil viscosity at different temperatures, Fuel 86 (2006) 1069-1078.

[59] I.N. Evdokimov, N.Y. Eliseev, D.Y. Eliseev, Effect of asphaltenes on the thermal properties of emulsions encountered in oil recovery operations, Fuel 83 (2004) 897-903.

[60] I.N. Evdokimov, N.Y. Eliseev, D.Y. Eliseev, Thermophysical properties and phase-behaviour of asphaltene-containing petroleum fluids, Fluid Phase Equilib. 212 (2003) 269-278.

[61]   M.-S. Lin, J.M. Chaffin, R.R. Davison, C.J. Glover, J.A. Bullin, A new suspension viscosity model and its application to asphaltene association thermodynamics and structures. in: O. C. Mullins, and E. Y. Sheu, (Eds.),

Structures and dynamics of asphaltenes. Plenum Press, New York, pp. 267-302.1998.

Chapter 8

Pentane-Asphaltene rheological behavior in reconstituted crude oils

MD. Anwarul Hasan and John M. Shaw

Abstract

The properties of asphaltenes present in crude oils remain the subjects of debate in the literature. In this work, the complex and zero shear viscosities of reconstituted samples prepared by mixing chemically separated pentane asphaltenes and maltenes were obtained. The samples were of four different types, namely: Athabasca asphaltene + Athabasca maltene (reconstituted Athabasca bitumen), Maya asphaltene + Maya maltene (reconstituted Maya crude), as well as cross mixtures comprising Athabasca asphaltene + Maya maltene, and Maya asphaltene + Athabasca maltene. The zero shear viscosities of these samples are compared with one another, with the zero shear viscosities of asphaltene + pure diluent binary mixtures, and with zero shear viscosities of nanofiltered Athabasca bitumen and Maya crude oil samples reported previously. The Maya and Athabasca asphaltene properties in re-constituted samples are shown to differ from one another and from those in nanofiltered samples. However, the large temperature and composition variation of the relative viscosity of such mixtures is attributed primarily to redistribution of residual pentane from the maltenes to the asphaltenes on reconstitution and only secondarily to properties of the chemically separated asphaltenes themselves. The physics and chemistry of asphaltene

behavior and of the differences arising from separation methods and diluent environments are not resolved in the present work and remain subjects for ongoing investigation.

Key words: Bitumen; Asphaltenes; Viscosity; Phase behavior; Nanofiltration, Reconstitute, Artifact.

8.1. Introduction

Bitumen and heavy oils are characterized by high density and viscosity, low hydrogen to carbon ratios, high carbon residues, and high asphaltene, heavy metal, sulfur and nitrogen[1,2] contents relative to conventional crude oils. A major processing limitation with heavy oils and bitumens is their extremely high viscosity that negatively affects production, transport and refining.[3,4] The high viscosity of bitumen and heavy oil is frequently attributed to the asphaltene fraction. The tendency for asphaltenes to flocculate, aggregate, or sediment is well known,[4-6] even in hydrocarbons where they are defined as soluble.[7, 8] These behaviors are linked to processing problems from formation damage and well plugging,[9] to reactor and line coking, to refinery tower plugging,[10-16] to catalyst deactivation.[17] Improved understanding of asphaltene nano-aggregates and their properties is expected to lead to novel strategies for mitigating many of these problems.

There is only limited agreement in the literature concerning the properties of asphaltenes. The mean size, structure and behavior of asphaltenes in standard organic solvents have been studied extensively and continue to be active areas of research. Diverse shape, size, and other properties have been reported for asphaltenes in hydrocarbon liquids over time.[9,17-20] Alternative non-particulate interpretations of data on which such determinations have been made are also available.[21] Some properties, like the existence of a critical micelle concentration have come to be refuted. Others such as asphaltene resin association have been challenged.[22] Asphaltene behaviors in crude oils and deasphalted oils were reviewed by Baltus et al.[23] Key works reported there include those by Mack et al.[24], Lorenz et al.[25], Reerink [26] and workers at the Texaco Research Center.[18, 27-31] Another pertinent summary of the literature was edited by Mullins et al.[32] Again diverse perspectives are presented.

Recent work on crude oil reconstitution,[33] the non-Newtonian rheological behavior of heavy oil,[34] and the rheology and phase behavior of nanofiltered as opposed to chemically separated oils[35,36] highlight the complexity associated with the reconstitution of oils, and attempts to attribute specific properties to individual fluid fractions. For example, Marques et al.,[33] noted the impact of dispersing asphaltenes in toluene prior to addition to the deasphalted crude and then evaporating the toluene vs. direct mixing of asphaltene powder with deasphalted crude on the resulting homogeneity of the reconstituted crude. The impact of maltene phase behavior on the rheological properties of heavy oil and bitumen, which is frequently attributed to asphaltenes, has also been addressed.[35] At low

temperatures maltenes solidify and make a significant contribution to the dispersed solids content of feedstocks. The feedstocks also become non-Newtonian in their rheological behavior at low temperature. Thus, many "viscosity" measurement techniques, which are based on Newtonian behavior become inapplicable, and data derived from them are invalid.[34] Misattribution of these impacts to asphaltenes and their properties leads to the apparent presence of properties for which there is no supporting fluid physics. Inclusion of these low temperature effects greatly simplifies our understanding of the phase behavior of asphaltene rich feedstocks. For example, zero shear relative viscosity vs. solids wt. % for nanofiltered Maya crude and Athabasca bitumen become a temperature and base oil independent function. The rheological behavior of feed, permeate and retentate samples was found to be consistent with that of a slurry comprising a Newtonian liquid plus a dispersed solid comprising non-interacting hard spheres, where the solid fraction was taken as the sum of the solid maltene plus asphaltene mass fractions. From a purely rheological perspective, non-interacting and non-circulating liquid drops would yield comparable behavior.

In this contribution, the rheological behavior of reconstituted Athabasca bitumen and Maya crude oil samples prepared by mixing chemically separated asphaltenes and maltenes is evaluated. The results obtained are compared with the rheological behavior of nanofiltered samples derived from the same feed stocks that were published previously,[35] and asphaltene + tetrahydrofuran, toluene and 1-methyl naphthalene binary mixtures. Central questions in this work include whether and in what way the properties of reconstituted samples resemble properties of

feedstocks and nanofiltered feedstocks, and whether simple standard theories and models related to the rheology of dispersions are applicable to reconstituted feedstocks, as is the case for nano filtered feedstocks.

8.2. Theory

8.2.1. Rheological Response of Dispersions

A detailed review of the rheology of dispersions is beyond the scope of the present work. Readers are referred eleswhere.[37, 38] Here key phenomena are outlined briefly. For dispersions of non-interacting mono-dispersed rigid spherical particles in a Newtonian fluid, relative viscosity is temperature independent and can be predicted and correlated using various hard sphere models up to volume fractions 0.30 [39-42] For higher volume fractions additional empirical and semi-empirical equations are available.[43-47] As the size, shape, size distribution and surface properties, such as particle-particle and particle-fluid interactions, of particles deviate from this base case, the relative viscosity of dispersions changes as illustrated in Figure 8.1.[48-51] The impacts of these deviations are diverse and it is critical to have a clear understanding of particle properties, or changes in particle properties with concentration in order to correlate much less predict resulting behaviors. For example, if particles interact with the surrounding fluid, as the particles become smaller the impact on viscosity increases at fixed volume fraction, where as if the particles do not interact with the fluid, their impact diminishes as the particles approach molecular dimensions.

186
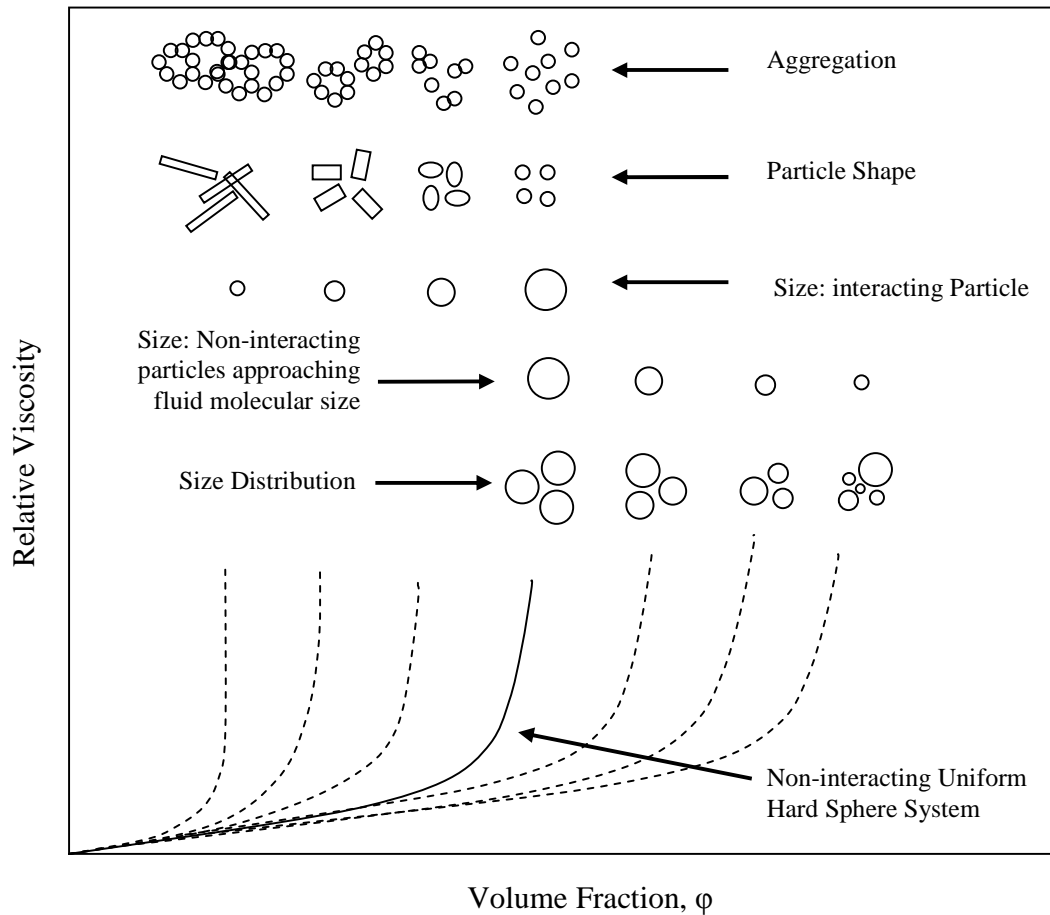
Figure 8.1. Qualitative effect of particle characteristics on the relative viscosity of colloidal dispersions.[48-51]

Shifts in average aggregate size distribution and structure with composition also impact relative viscosity. The extent to which such physical phenomena influence the rheological behavior of asphaltene + feedstock mixtures is unknown a priori and it is not clear whether simple models of dispersion behavior based on a

specific particle physics phenomenon can correlate or capture the behavior of such mixtures. These models typically possess two asymptotes as illustrated in Figure 8.1 and the functions tend to be concave. At low volume fractions, particles have little impact on relative viscosity where as at high volume fractions the dispersions approach solid like rheological behaviors and the relative viscosity trends to infinity.

8.2.2. Rheology of Asphaltene + hydrocarbon mixtures

In our prior work,[35] the rheological behavior of nanofiltered Athabasca bitumen and Maya crude oil related permeate and retentate samples were found to be consistent with slurries comprising a Newtonian liquid + non-interacting spherical particles in the temperature range 298 K to 373 K, because the zero shear relative viscosity of all of the samples was correlated using Sudduth's equation:[52]

$$\ln(\eta/\eta_0) = \left(\frac{[\eta]}{k}\right)\left(\frac{1}{\sigma-1}\right)\left[(1-k\varphi)^{1-\sigma}-1\right] \qquad (8.1)$$

where, η_o is the viscosity of the continuous phase, η is the viscosity of the dispersion, $[\eta]$ is the intrinsic viscosity (2.5 for spherical particles in Newtonian liquids), k is the crowding factor, σ is the interaction coefficient (3.5 for non-interacting hard spheres), and φ is the volume fraction of particles. The relative viscosity for all samples was fit with a single set of temperature independent values, namely: $[\eta] = 2.5$, $\sigma = 3.5$, and $k = 1.38$, the only regressed coefficient,

resulting in a temperature and fluid independent function. As asphaltene aggregate density in mixtures and hence volume fraction are not known a priori, wt. fraction was used as a surrogate. Asphaltene wt. fractions in nanofiltered samples ranged from 0.015 for 5 nm Maya permeate to just over 0.7 for 50 nm Maya retentate. This places the maximum value for the crowding factor at less than ~ 1.4. The minimum value is also constrained, because even the densities of pure crystalline polynuclear aromatic solids, such as coronene, are less than 1470 Kg/m^3. The minimum value for the crowding factor must exceed ~ 0.7. For the model to be internally consistent and make physical sense, the crowding factor must fall within these narrow bounds and is not a freely regressed parameter.

Other workers have applied the Pal-Rhode's equation:[53]

$$\eta / \eta_0 = (1 - k_s \varphi)^{-[\eta]} \qquad (8.2)$$

where K_s is the solvation constant, to describe the viscosity of asphaltenes in standard organic solvents,[23] and in natural and synthetic vacuum residues.[54] Reported values for the solvation constant range from 1 to 9.3.[55] The "shape factor" a generalization of the intrinsic viscosity, appearing in equation 8.2, is also allowed to vary in regressions. These coefficients are typically liquid and temperature dependent, indicating a broad range of behaviors for chemically separated asphaltene + hydrocarbon liquid mixtures that are inconsistent with the physics linked to simple dispersion models. Further, parameters appearing in

189

diverse rheological models applied to the same viscosity data, may indicate that infinite viscosity asymptotes are approached at volume fractions from ~ 0.3 to ~ 0.7,[56] suggesting that diverse and incompatible fluid physics may be at play in the same mixtures. Care must be taken not to over interpret such fits. The adage that correlation does not imply causality is pertinent. Physical interpretation requires data from independent data sets. Sirota and Yin,[57] for example, reinforce this point with their work on the physical behaviour of chemically separated asphaltenes in mixtures with organic solvents.

8.3. Experimental

8.3.1. Materials:

Athabasca bitumen (Alberta, Canada) was obtained from Syncrude Canada Ltd., and Maya crude oil (Mexico) was obtained from the Mexican Petroleum Institute (IMP). The SARA analyses of Athabasca bitumen (AB) and Maya crude oil are reported in Table 8.1. Additional analyses are available elsewhere.[58] Purities of

Table 8.1. SARA analysis (wt. %) of Athabasca bitumen and Maya crude Oil

	Athabasca bitumen	Maya crude oil
Saturates	16.1	31.6
Aromatics	48.5	42.5
Resins	16.8	10.2
Asphaltenes (C5)	18.6	15.7

pentane, toluene, and tetrahydrofuran were 99% while that of 1-methyl naphthalene was 97%.

8.3.2. Sample Preparation:

Asphaltenes and Maltenes were separated from Athabasca bitumen and Maya crude oil using n-pentane. For this separation, n-pentane was added to bitumen / crude oil at a ratio of 40:1. The mixture was stirred overnight at room temperature and then filtered in two steps by vacuum filtration. First, the mixture was filtered through a Fisher brand filter paper Q2, with a pore size 1-5 µm. The permeate was then filtered using a 0.22 µm Millipore cellulose ester membrane. The filters and the flask were washed with small volumes of n-pentane to eliminate residual oil. This step was repeated until the filtrate was colorless. The membranes with the precipitated material were dried at 100 °C for 30 minutes and placed overnight in a vacuum oven at 9 kPa and 303 K. The permeate was distilled at 313 K and 9 kPa in a rota-evaporator to eliminate n-pentane.

Ensuring homogeneous re-dispersion of asphaltenes during re-constitution of oil samples is a difficult task. Marques et al.[33, 59] found that mixing asphaltene powder with maltenes and stirring the resulting mixtures at 353 K for eight hours was inadequate. In this work, asphaltene + maltene dispersions were prepared by mixing asphaltenes with maltenes at room temperature. The mixtures were then kept in sealed stainless steel vials in an oven at 473 K for 72 hours so that

comparisons with nanofiltered samples, treated in a similar manner, could be made. The samples were then placed in an ultrasonic bath for 12 hours at 333 K. Mass balances were performed on all samples. Samples that showed any mass loss following this procedure were discarded. Rheological measurements were performed for three aliquots taken from different elevations within each sample vial. Aliquots for which the rheological data from the three measurements were similar [within +/- 5 %] were considered macroscopically homogeneous. Average zero shear viscosity values are reported in Tables 8.2 and 8.3. For asphaltene + pure organic liquid mixtures, constituents were mixed at room temperature in air tight vials that were then placed in an ultrasonic bath for several hours. Mass balances were also performed for these samples.

8.3.3. Rheological Experiments:

Complex viscosity $|\eta*|$ measurements were carried out using a Bohlin Gemini 200 HR Nano-Rheometer (Malvern Instrument, UK) over the temperature 298 K to 373 K. Three types of measuring configurations were used:

1) Parallel plate geometries with 40 mm diameter plates supplied with the extended temperature cell with stability of $\pm$ 0.2 K. This geometry was used for samples prepared in Athabasca maltene for which sample evaporation is not a problem over the time and temperature range of measurements.[34]

2) Parallel plate geometries with 40 mm diameter plates along with a solvent trap supplied with a Peltier plate assembly with stability of $\pm$ 0.2 K. This configuration

Table 8.2. Solid concentrations, zero shear and relative viscosities of Athabasca maltene related nanofiltered and reconstituted samples.

T, K	asphaltenes (wt. %)	solid maltene[35] (wt. %) in sample	total solids (wt. %)	nanofiltered Athabasca bitumen[35]		chemically separated and reconstituted samples			
						Athabasca asphaltenes in Athabasca maltene		Maya asphaltenes in Athabasca maltene	
				zero shear viscosity (Pa·s)	zero solid relative viscosity	zero shear viscosity (Pa·s)	Zero solid relative viscosity	zero shear viscosity (Pa·s)	Zero solid relative viscosity
298	0	20.7	20.7	187/72*	2.6	6.1/2.7*	2.3		
303	0	16.5	16.5	85/44*	1.9	3.6/2.0*	1.8		
323	0	0	0	7.3	1.0	0.64	1.0		
348	0	0	0	1.0	1.0	0.24	1.0		
373	0	0	0	0.19	1.0	0.070	1.0		
298	5.3	19.6	24.9	185	2.6	55	20	108	40
303	5.3	15.6	20.9			27	14	54	27
323	5.3	0	5.3	5.6	0.8	3.0	4.7	5.9	9.2
348	5.3	0	5.3	0.68	0.7	0.47	2.0	0.89	3.7
373	5.3	0	5.3	0.19	1.0	0.13	1.8	0.25	3.6
298	10.4	18.5	28.9	430	5.9	170	63	303	112
303	10.4	14.8	25.2			87	43	141	70
323	10.4	0	10.4	12	1.6	7.9	12	13	20
348	10.4	0	10.4	1.2	1.2	0.80	3.3	1.7	6.9
373	10.4	0	10.4	0.24	1.3	0.12	1.8	0.43	6.2
298	13.6	17.9	31.5	460	6.4	225	83	412	152
303	13.6	14.3	27.9			105	52	201	100
323	13.6	0	13.6	12	1.6	9.0	14	19	30
348	13.6	0	13.6	1.1	1.1	1.0	4.2	2.4	10
373	13.6	0	13.6	0.31	1.6	0.22	3.1	0.63	8.9
298	18.6	16.8	35.4	1710	24	375	138	670	247
303	18.6	13.4	32.0	581	13	173	86	305	151
323	18.6	0	18.6	32	4.5	14	22	24	37
348	18.6	0	18.6	2.7	2.7	1.8	7.6	3.2	13
373	18.6	0	18.6	0.51	2.7	0.51	7.3	0.78	11

* Extrapolated values for solid free liquid.

Table 8.3. Solid concentrations, zero shear and relative viscosities of Maya maltene related nanofiltered and reconstituted samples.

| T, K | asphaltenes (wt. %) | solid maltene[35] (wt. %) | total solids (wt. %) | nanofiltered Maya crude oil samples[35] | | chemically separated and reconstituted samples | | | |
| | | | | | | Athabasca asphaltenes in Maya maltene | | Maya asphaltenes in Maya maltene | |
				zero shear viscosity (Pa·s)	zero solid relative viscosity	zero shear viscosity (Pa·s)	zero solid relative viscosity	zero shear viscosity (Pa·s)	zero solid relative viscosity
298	0	12.1	12.1	0.36/0.27*	1.3			0.038/0.033*	1.2
303	0	9.0	9.0	0.33/0.22*	1.5			0.028/0.028*	1.0
323	0	0.8	0.8	0.10	1.0			0.015	1.0
348	0	0	0	0.043	1.0			0.0074	1.0
373	0	0	0	0.021	1.0			0.0042	1.0
298	5.3	11.5	16.8			0.10	3.0	0.13	4.0
303	5.3	8.5	13.8			0.075	2.7	0.088	3.2
323	5.3	0.8	6.1			0.023	1.5	0.029	2.0
348	5.3	0	5.3			0.012	1.6	0.014	1.9
373	5.3	0	5.3			0.0061	1.5	0.0083	2.0
298	6.2	11.4	17.6	0.51	1.9	0.11	3.4	0.15	4.6
303	6.2	8.4	14.6	0.32	1.5	0.078	2.8	0.13	4.5
323	6.2	0.7	6.9	0.14	1.4	0.028	1.9	0.064	4.3
348	6.2	0	6.2			0.013	1.8	0.026	3.5
373	6.2	0	6.2	0.014	0.7	0.0075	1.8	0.012	2.8
298	9.4	11.0	20.4	0.88	3.3	0.17	5.0	0.23	6.9
303	9.4	8.2	17.5	0.45	2.0	0.12	4.1	0.14	5.1
323	9.4	0.7	10.1	0.17	1.7	0.038	2.6	0.067	4.5
348	9.4	0	9.4			0.016	2.2	0.040	5.5
373	9.4	0	9.4	0.018	0.9	0.0095	2.2	0.0094	2.2
298	10.4	10.9	21.3			0.22	6.6	0.32	9.8
303	10.4	8.1	18.5			0.16	5.7	0.21	7.6
323	10.4	0.7	11.1			0.054	3.6	0.085	5.7
348	10.4	0	10.4			0.022	3.0	0.051	7.0
373	10.4	0	10.4			0.010	2.4	0.015	3.6
298	13.6	10.5	24.1			0.26	7.8	0.55	17
303	13.6	7.8	21.4			0.18	6.5	0.48	17
323	13.6	0.7	14.3			0.070	4.6	0.20	14
348	13.6	0	13.6			0.041	5.6	0.082	11
373	13.6	0	13.6			.028	6.5	0.043	10
298	15.7	10.2	25.9	0.95	3.5	0.31	9.4	0.60	18
303	15.7	7.6	23.3	0.70	3.2	0.21	7.4	0.60	21
323	15.7	0.7	16.4	0.23	2.2	0.089	6.0	0.15	10
348	15.7	0	15.7	.079	1.8	0.043	5.9	0.051	7.0
373	15.7	0	15.7	.039	1.9	0.018	4.3	0.050	12
298	18.6	9.9	28.5			3.3	99	5.4	163
303	18.6	7.3	25.9			2.1	77	3.4	122
323	18.6	0.6	19.2			0.23	15	0.32	22
348	18.6	0	18.6			0.061	8.3	0.13	18
373	18.6	0	18.6			0.032	7.6	0.073	17

Extrapolated values for solid free liquid.

was used for reconstituted samples prepared with Maya maltene to avoid sample loss during the course of measurement.[34]

3) A double gap 24/27 mm concentric cylinder with the Peltier cylinder assembly allowing measurements with stability of ± 0.2 K. This latter geometry was used for very low viscosity samples: chemically separated Maya maltene, asphaltnes + pure organic liquids, and pentane + chemically separated maltenes.

For the double gap cylinder, the gap was fixed at 0.15 mm. For the parallel plate configuration, gaps of 0.3 mm, 0.45 mm and 0.75 mm were applied depending on how viscous the samples were. These gaps were chosen based on test measurements on two standard materials: PRA standard oil # 12, and PRA standard oil U0600. The other conditions used in the experiments e.g. shear stress or strain, measurement time, frequency etc. were also validated using PRA standard oil # 12 and PRA standard oil U0600 with viscosities of 0.972 Pa·s and 0.1 Pa·s at 298 K respectively. The agreement with the recommended data was within 5%. In order to ensure the consistency of the measurements obtained using different geometries, experiments were performed using two geometries in the overlap range where different geometries could be used interchangeably. Results agreed within experimental error, as was observed previously.[34] In some cases, experiments were repeated with more than one gap to ensure that the gap used was within appropriate limits. Artifacts related to "gap loading" were thus avoided.[34]

Rheological measurements with Athabasca samples were performed using the oscillatory shear method under nitrogen cover while those with Maya samples were performed using oscillatory shear method under the solvent trap. Measurements with pure diluents were performed using the steady shear method. The frequency was varied between 0.1 Hz and 100 Hz. In the oscillatory shear method, frequency of oscillation is equivalent to the term shear rate used in steady shear experiments, when both are expressed in the same units, the Cox-Merz rule ($|\eta^*(\omega)| = \eta(\dot{\gamma}=\omega)$) can be applied. Oscillation amplitude sweep tests were performed first at the lowest and the highest frequencies, to identify the stress and strain limits for the linear viscoelastic region, within which subsequent measurements were obtained.

8.4. Results and Discussion

8.4.1. Viscosity:

Complex viscosities at 298 K for reconstituted samples and heat-treated Maya crude and Athabasca bitumen are reported in Figures 8.2 and 8.3 respectively. As it is at low temperatures where non-Newtonian effects are expected,[34] this presents the most challenging condition for the identification of zero shear viscosity values. With the possible exception of some cases in Figure 8.2 d, all samples plateau at frequencies greater than 1 Hz, and even these samples plateau at ~ 0.1 Hz. The zero shear viscosity is readily identified for all compositions and temperatures evaluated. Zero shear viscosity values are reported in Table 8.2 and

196
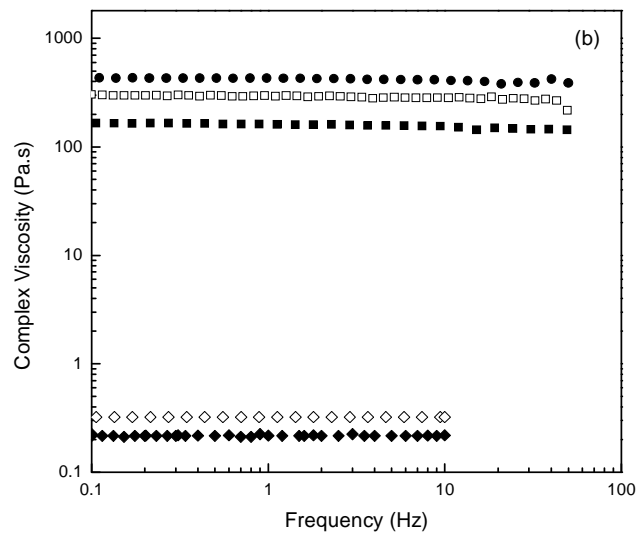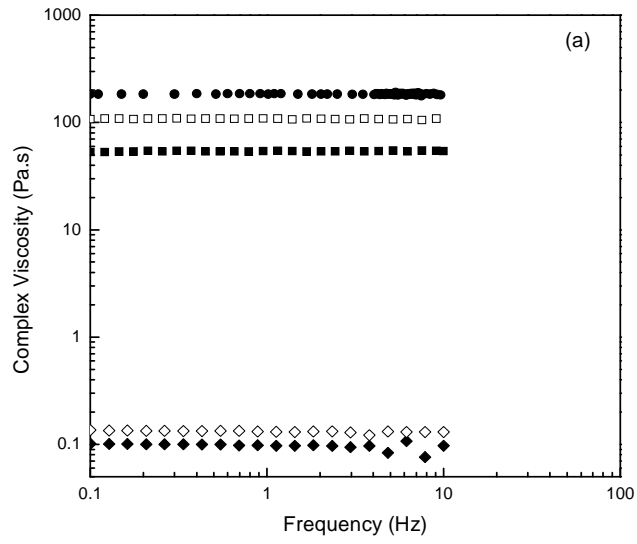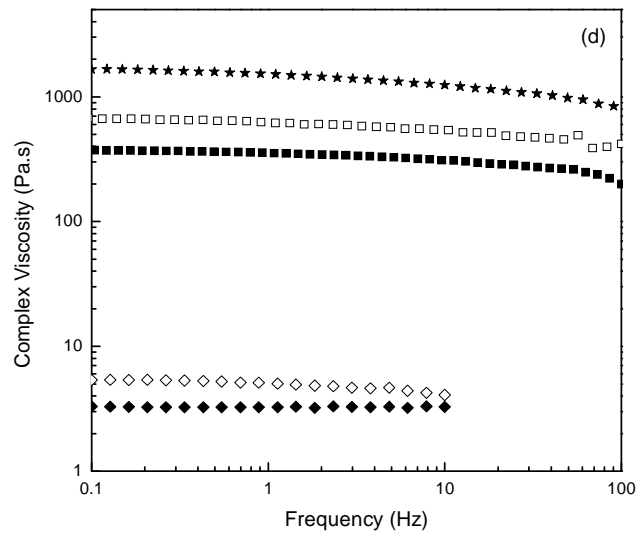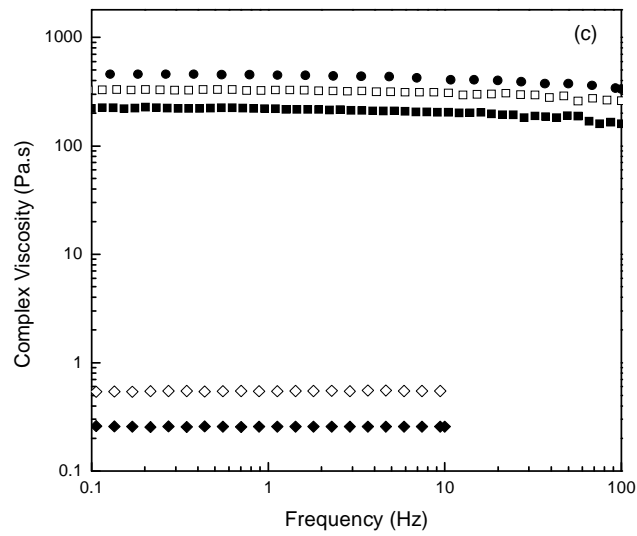
Figure 8.2. Complex viscosity of Athabasca bitumen based samples, at 298 K(a) 5.3%, (b) 10.4%, (c) 13.6%, and (d) 18.6% asphaltenes.●, Nanofiltered AB samples, ★, Heat treated AB; □, Maya asphaltene in AB maltene; ■, AB asphaltene in AB maltene; ◇, Maya asphaltene in Maya maltene, and ◆, AB asphaltene in Maya maltene.

199
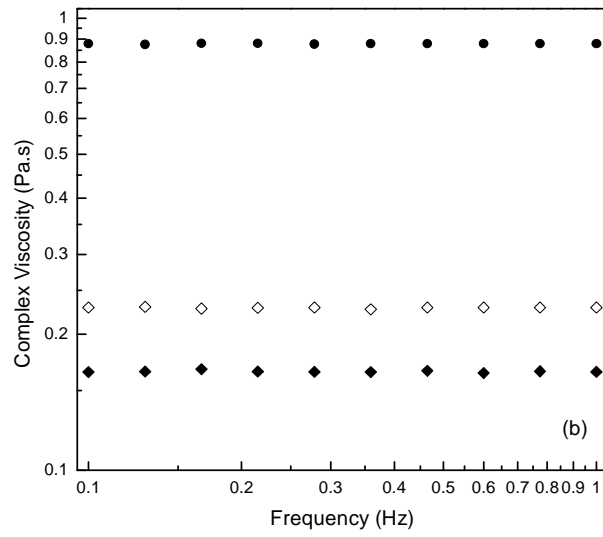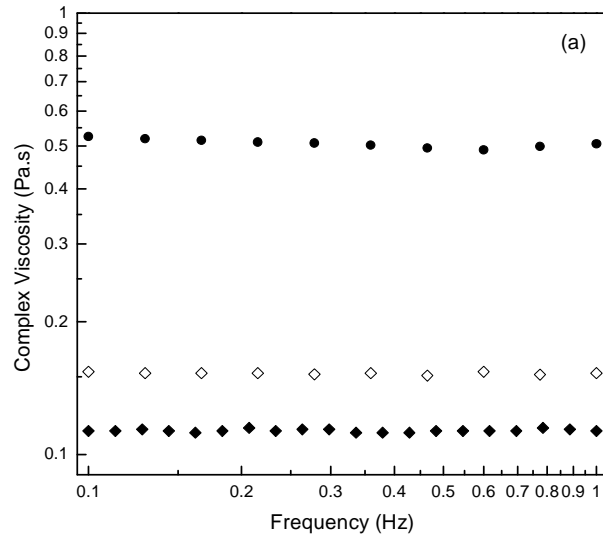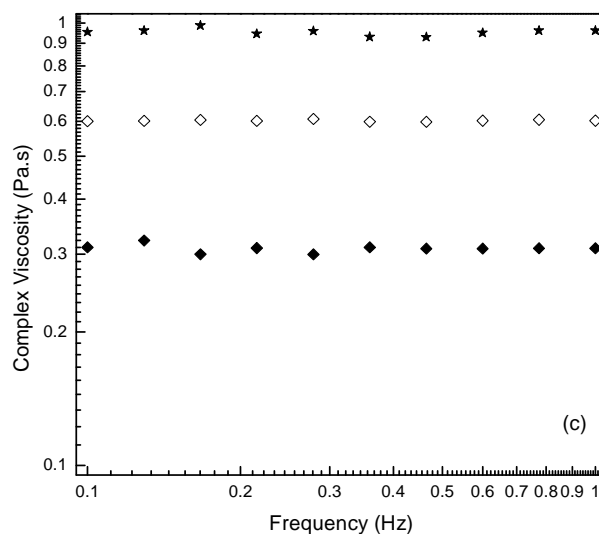
Figure 8.3. Complex viscosity of Maya maltene based samples, at 298 K: (a) 6.2%, (b) 9.4%, (c) 15.7% asphaltenes. ●, Nanofiltered Maya samples; ★, Heat treated Maya crude; ◆, Maya asphaltene in Maya maltene; ◆, AB asphaltene in Maya maltene.

Table 8.3 along with extrapolated zero solids viscosities. Zero shear viscosities of chemically separated maltenes and nanofiltered samples were measured. The zero solids viscosities are estimates. As Athabasca and Maya maltenes comprise a mix of solids and liquids up to approximately 320 K, their viscosities on a solids free basis, were extrapolated, using Arrhenius extrapolation of higher-temperature zero-shear viscosities (323 K, 348 K, and 373 K). Viscosity values for nanofiltered maltenes were also obtained by extrapolation. This is necessary because asphaltene-free permeates were not obtained by nanofiltration. Permeate with 1.5 wt % pentane asphaltenes, obtained with a 5 nm nominal pore size, was

available for Maya crude, while permeate with 5.3 wt % pentane asphaltenes obtained with a 10 nm nominal pore size, was available for Athabasca bitumen[58]. The extrapolation procedure for nanofiltered samples is discussed elsewhere.[35] The relative viscosity of all samples and the total solid concentrations are also reported in Tables 8.2 and 8.3. The relative viscosity reported here is the ratio of the zero shear viscosity of the reconstituted samples to that of solid free maltene at the same temperature. The total solid wt. % is the sum of asphaltene wt. % and solid maltene wt. % of the samples.

8.4.2. Nanofiltered versus Reconstituted Samples:

The zero shear viscosities of both asphaltene free and solid free nanofiltered maltenes, obtained without the use of solvents, are roughly one order of magnitude greater than the corresponding values of chemically separated maltenes as shown in Tables 8.2 and 8.3. This difference, noted in our prior work, is attributed to the presence of residual solvent in the chemically separated maltene samples. A small mass fraction of solvent has a significant impact on viscosity values as shown in Tables 8.4 and 8.5 and on the viscosity relative to the nanofiltered maltene, Figures 8.4a and 8.4b when pentane is added to chemically separated Maya and Athabasca maltenes respectively. The composition and temperature dependences are both significant.

If the asphaltene properties are unaffected by precipitation and redispersion, then according to equations 8.1 and 8.2, and other simple models of dispersion

behavior, the zero shear viscosity of the nanofiltered samples should be a simple multiple of the zero shear viscosity of reconstituted Maya crude and Athabasca bitumen samples. The zero shear viscosities of nanofiltered and reconstituted Athabasca and Maya samples are compared in Figure 8.5 a. The viscosities of reconstituted samples are consistently lower than nanofiltered samples with the same asphaltene wt %, as expected, but the viscosity ratio of nanofiltered vs reconstituted samples, is a function of temperature, Figure 8.5b, and the ratio is significantly less than one would anticipate based on the viscosity ratio of the chemically separated and nanofiltered maltenes on their own, Figure 8.6, if simple models of dispersion behavior were directly applicable.

Table 8.4. Zero shear viscosity of chemically separated Maya maltene + pentane mixtures

pentane (wt. %)	zero shear viscosity				
	298 K	303 K	323 K	348 K	373 K
0	0.0384	0.0308	0.0150	0.00735	0.00422
1	0.0337	0.0275	0.0136	0.00681	0.00400
2.5	0.0272	0.0225	0.0115	0.00599	0.00363
5	0.0200	0.0171	0.00924	0.005	0.00321
10	0.0129	0.0112	0.00653	0.00382	0.00275

Table 8.5. Zero shear viscosity of chemically separated Athabasca maltene + pentane mixtures

Pentane (wt. %)	Zero shear viscosity				
	298 K	303 K	323 K	348 K	373 K
0	6.14	3.59	0.641	0.2340	0.0701
2.5	2.89	1.84	0.427	0.202	0.0996
5	1.41	0.894	0.215	0.196	0.0486
10	0.475	0.413	0.144	0.101	0.0475
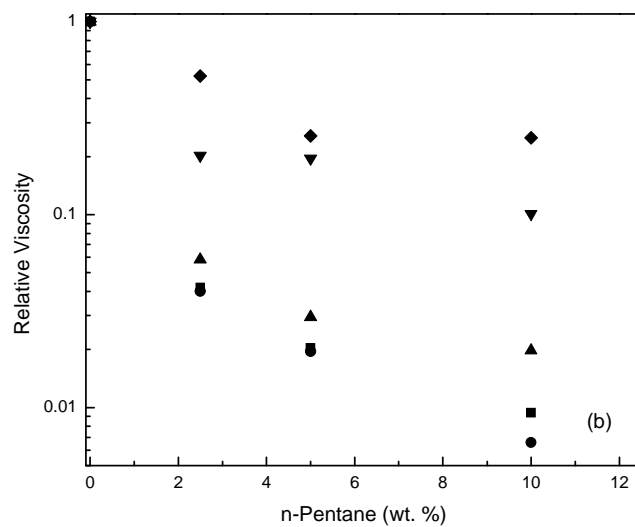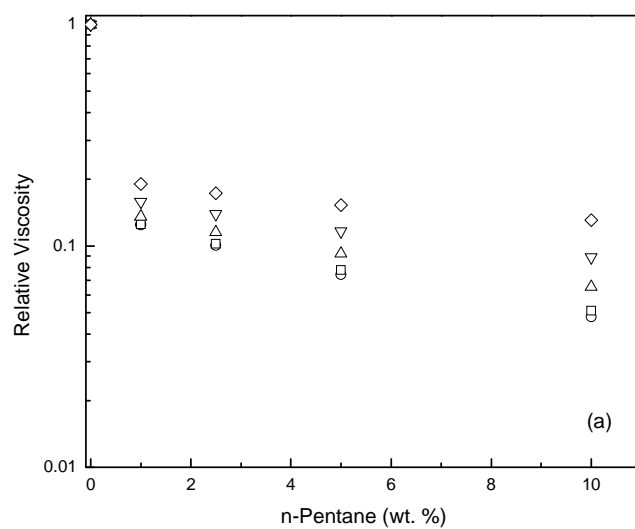
Figure 8.4. Relative viscosity of pentane + Maya maltene (a) and Athabasca Maltene (b) mixtures. Temperature is a parameter. (Maya samples: ○, 298 K; □, 303 K; △, 323 K; ▽, 348 K, ◇, 373 K. Athabasca Bitumen samples; ●, 298 K; ■, 303 K; ▲, 323 K; ▼, 348 K, ◆, 373 K).
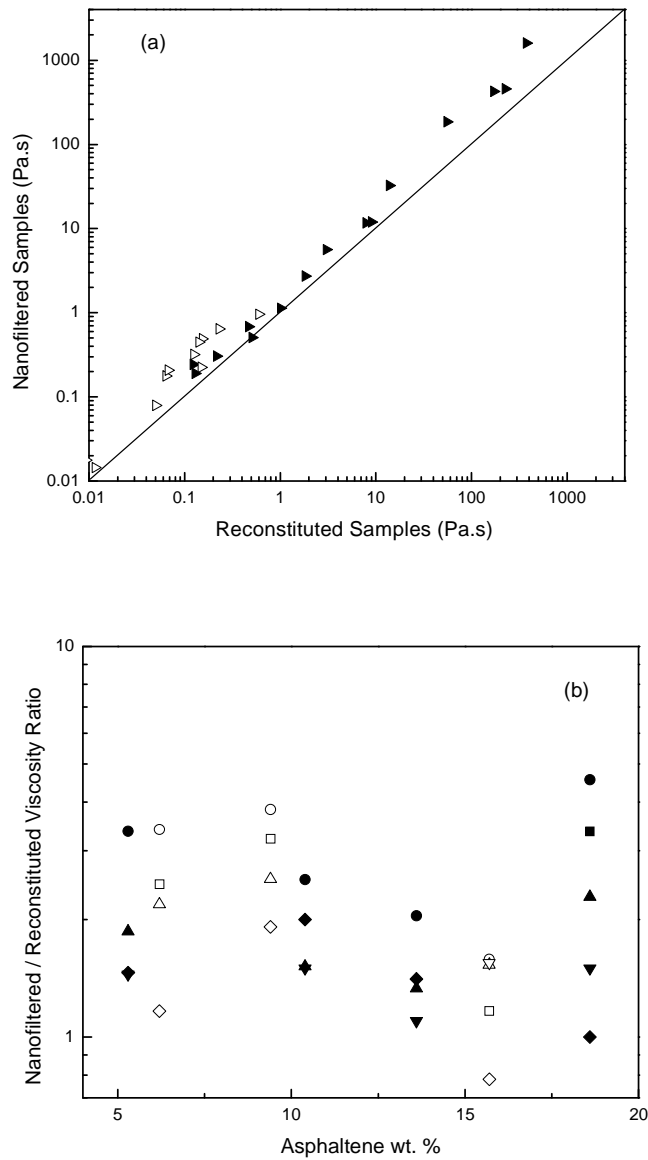
Figure 8.5. a) A comparison between the zero shear viscosities of nanofiltered and reconstituted samples with the same asphaltene content: ▷, Maya crude; ►, Athabasca bitumen, b) The ratio of the viscosity of nanofiltered to reconstituted samples as a function of mixture composition (Maya samples: ○, 298 K; □, 303 K; △, 323 K; ▽, 348 K, ◇, 373 K. Athabasca Bitumen samples; ●, 298 K; ■, 303 K; ▲, 323 K; ▼, 348 K, ◆, 373 K).

8.4.3. Reconstituted versus cross-reconstituted samples

The zero shear viscosity of reconstituted Maya and Athabasca samples are compared with their cross mixtures, Athabasca asphaltenes in Maya maltenes and Maya asphaltenes in Athabasca maltenes, at the same asphaltene mass % and temperature, in Figure 8.7. Athabasca asphaltenes have consistently less impact on viscosity compared to Maya asphaltenes. The impact on viscosity is approximately a factor of two irrespective of asphaltene wt % and temperature. As the base maltenes are the same, this difference can only be attributed to differences in the properties of the two chemically separated asphaltenes.
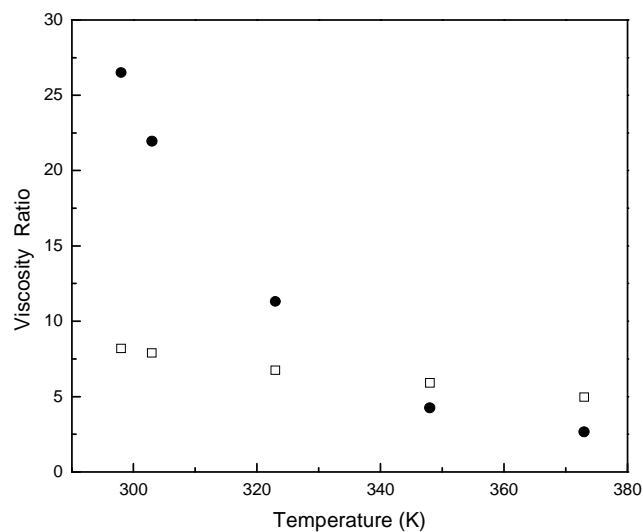
Figure 8.6. The viscosity ratio of nanofiltered maltene to chemically separated maltene as a function of temperature: □, Maya maltene; ●, Athabasca maltene.
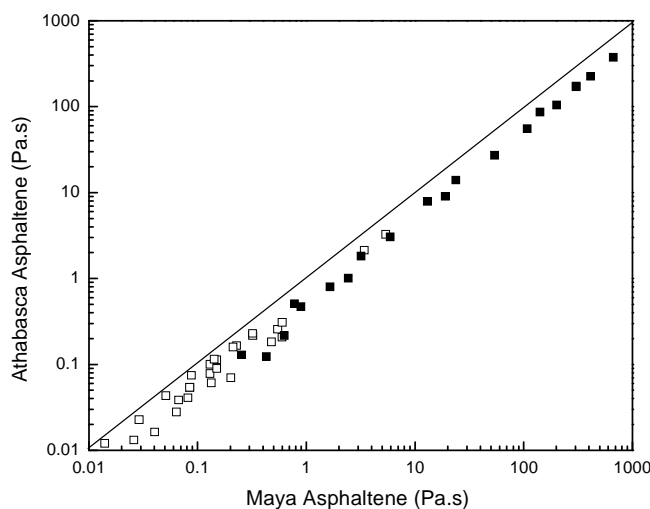
Figure 8.7. A comparison of zero shear viscosities of reconstituted Maya and Athabasca samples with reconstituted cross mixtures of Maya asphaltenes in Athabasca maltenes and Athabasca asphaltenes in Maya maltenes at same asphaltene wt.%.□, Maya maltene; ■, Athabasca maltene.

8.4.4. Relative viscosity

To connect measured zero shear viscosities to dispersion models, relative viscosities of dispersions are typically compared to those of standard cases sketched in Figure 8.1 where the volume fraction of the dispersed phase comprises the independent variable. The relative zero-shear viscosities of mixtures comprising chemically separated asphaltenes in Athabasca and Maya maltenes are shown in Figures 8.8 (a) and (b) respectively. Temperature is a parameter. The solid curve, equation 8.1, where $[\eta] = 2.5$, $\sigma = 3.5$, and $k = 1.38$,
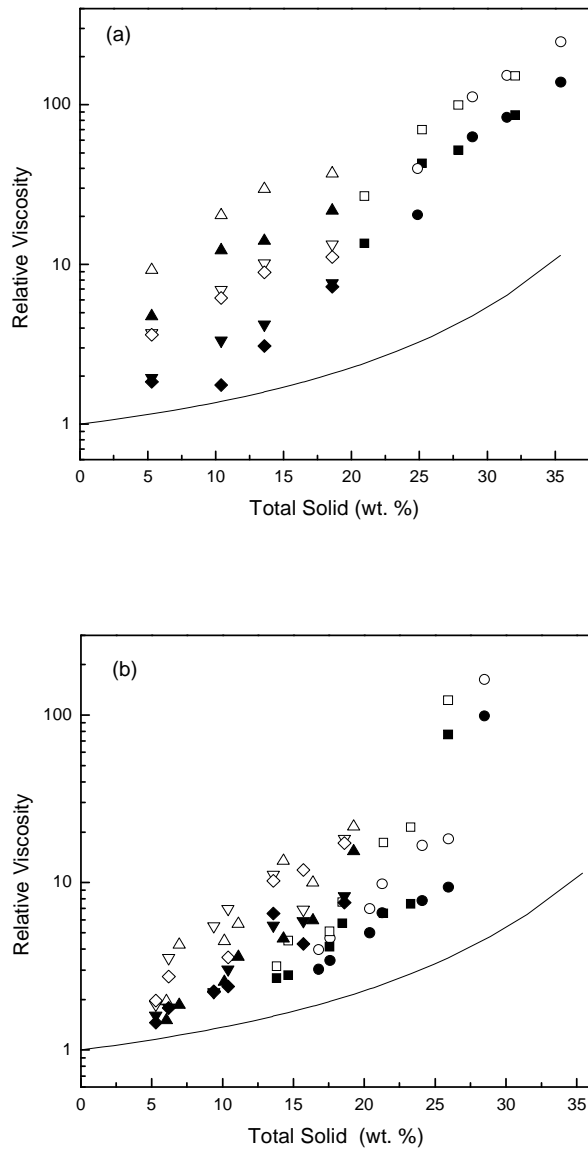
Figure 8.8. The relative viscosity of reconstituted asphaltene + maltene samples (a) in Athabasca maltenes, (b) in Maya maltenes. Maya asphaltenes:○, 298 K; □, 303 K; △, 323 K; ▽, 348 K, ◇, 373 K; Athabasca asphaltenes ●, 298 K; ■, 303 K; ▲, 323 K; ▼, 348 K, ◆, 373 K. Solid curve, equation 8.1 with parameters describing the behavior of nanofiltered samples[35].

is a temperature independent regression for the relative viscosity of nanofiltered Athabasca bitumen and Maya crude samples. The relative viscosities of reconstituted samples are plotted against the solids mass fraction of samples, as volume fractions are not known. The relative viscosity values are more than one order of magnitude greater than those of the nanofiltered samples having the same nominal composition, in some cases, but are comparable in magnitude to published values for relative viscosities of other reconstituted oils where composition ranges overlap.[56] The values are also temperature dependent. Thus the rheological behavior of chemically separated asphaltene + maltene mixtures appears to differ from comparable nanofiltered samples both quantitatively and qualitatively.

8.4.5. Interpretation of the absolute and relative viscosity data for reconstituted samples

Pentane redistribution within the reconstituted mixtures presents an uncontrolled variable affecting the interpretation of the relative viscosity data for the reconstituted samples. This arises because the zero shear viscosity of the maltenes is impacted significantly by small mass fractions of pentane, Figures 8.4 and 8.6. The impact is particularly large at low temperature. The impact remains significant but diminishes at higher temperatures. For example, the zero shear viscosities of nanofiltered Maya and Athabasca maltenes are 8 and 26 times the chemically separated analogues at 298 K but are only 5 and 3 times greater respectively at 373 K. A similar though less dramatic diminution of the impact of

pentane on the viscosity values is observed when pentane is added to the chemically separated maltenes. If a small fraction of the pentane present in the maltene is sorbed on or by the added asphaltenes, the reported relative viscosities of the dispersions becomes too high, because the pentane content of the maltene is reduced by such transfer. This potential artifact affects the interpretation of relative viscosity data for all reconstituted crude mixtures in the present work and in the literature. It would not however affect the interpretation of mixtures with pure hydrocarbon liquids where the composition of the liquid is not altered by sorption.

It is for this reason that sets of rheological measurements for Athabasca asphaltenes and Maya asphaltenes in toluene, 1-methyl naphthalene, and tetrahydrofuran were undertaken. Zero shear viscosity data for these mixtures are reported in Tables 8.6 and 8.7 while the relative viscosity data for individual liquids are reported in Figures 8.9 a-c and summarized in Figure 8.10. The composition dependence of relative viscosity while significant vis-à-vis nanofiltered samples, is an order of magnitude smaller than for the reconstituted Maya crude, Athabasca bitumen, and related cross mixtures. The temperature dependence of the relative viscosity at fixed composition is significantly less than for the reconstituted samples as well. Temperature effects are small and approach measurement error, except at high asphaltene mass %, where measurements may be sensitive enough for variations in the extent of sorption with temperature to be observed.

Table 8.6. Zero shear viscosity of Maya asphaltenes + pure hydrocarbon

liquids

Asphaltene (wt. %)	zero shear viscosity (Pa.s)				
	298 K	303 K	323 K	348 K	373 K
toluene					
0	0.00054	0.000521	0.000409	0.000325	0.000235
1	0.000588	0.000546	0.000458	0.000332	0.000271
2	0.000599	0.000561	0.000453	0.000391	0.000276
5.3	0.000745	0.000703	0.000575	0.000456	0.000339
10.4	0.00115	0.00107	0.000818	0.000618	0.000484
18.6	0.00279	0.00247	0.00182	0.00122	0.000939
30	0.00762	0.0065	0.00386	0.00239	0.00174
1-methyl napthalene					
0	0.00287	0.00255	0.00173	0.00119	0.000915
1	0.00319	0.00291	0.00194	0.00136	0.000976
2	0.00331	0.00294	0.002	0.00139	0.000981
5.3	0.00437	0.00387	0.00257	0.0017	0.00127
10.4	0.00733	0.00636	0.00393	0.00249	0.00172
18.6	0.0215	0.0179	0.00943	0.0052	0.00335
30	0.169	0.126	0.0494	0.0316	0.0106
tetrahydrofuran					
0	0.000434	0.000431	0.000393		
1	0.000423	0.000419	0.000403		
2	0.000475	0.000422	0.000397		
5.3	0.000564	0.000527	0.000428		
10.4	0.000842	0.000777	0.000623		
18.6	0.00143	0.00134	0.000996		
30	0.00982	0.00888			

Table 8.7. Zero shear viscosity of Athabasca asphaltenes + pure hydrocarbon

liquids

Asphaltene (wt. %)	Zero Shear Viscosity (Pa.s)				
	298 K	303 K	323 K	348 K	373 K
toluene					
0	0.00054	0.000521	0.000409	0.000325	0.000235
1	0.000544	0.000531	0.000422	0.000339	0.00024
2	0.000595	0.000563	0.00047	0.000357	0.000285
5.3	0.000686	0.000664	0.000551	0.000436	0.000325
10.4	0.000988	0.000925	0.000728	0.000559	0.00035
18.6	0.00195	0.00179	0.00133	0.000972	0.000759
30	0.00471	0.00429	0.00281	0.00191	0.00147
1-methylnapthalene					
0	0.00287	0.00255	0.00173	0.0012	0.000915
1	0.00297	0.00266	0.00181	0.00122	0.000902
2	0.00327	0.00291	0.00197	0.00132	0.000984
5.3	0.00436	0.00386	0.00261	0.00177	0.00132
10.4	0.00779	0.00675	0.00418	0.00261	0.00181
18.6	0.016	0.0134	0.00781	0.00453	0.00274
30	0.0476	0.0379	0.0181	0.00909	0.00541
tetrahydrofuran					
0	0.000434	0.000431	0.000393		
1	0.000458	0.000447	0.000405		
2	0.000493	0.000459	0.000399		
5.3	0.000621	0.00058	0.000482		
10.4	0.000914	0.000847	0.000669		
18.6	0.00192	0.00175	0.00135		
0	0.000434	0.000431	0.000393		
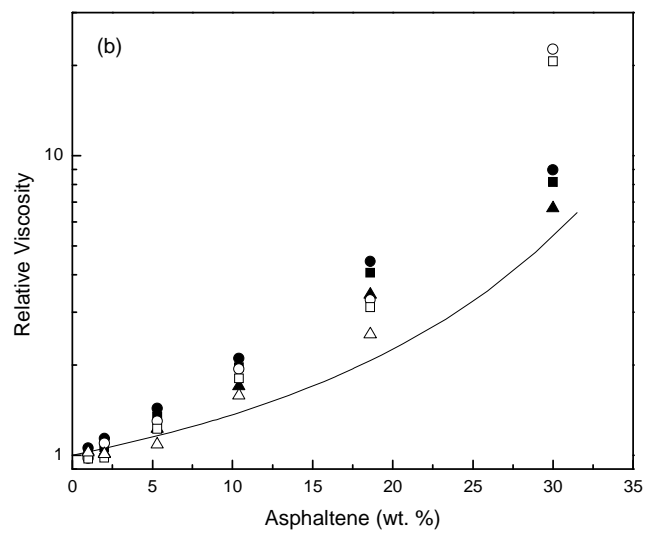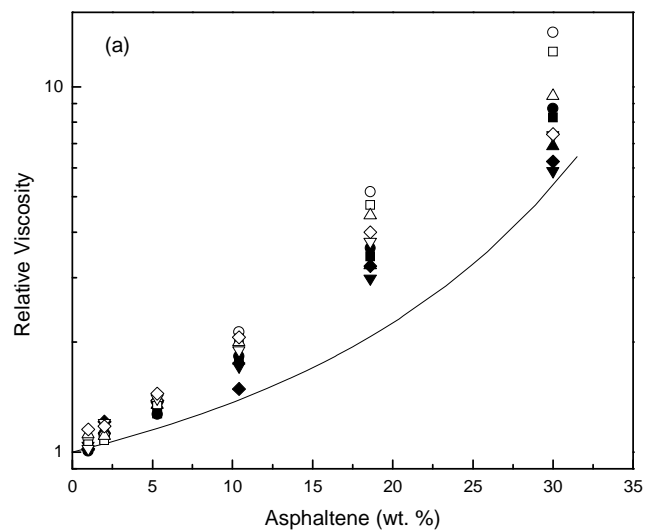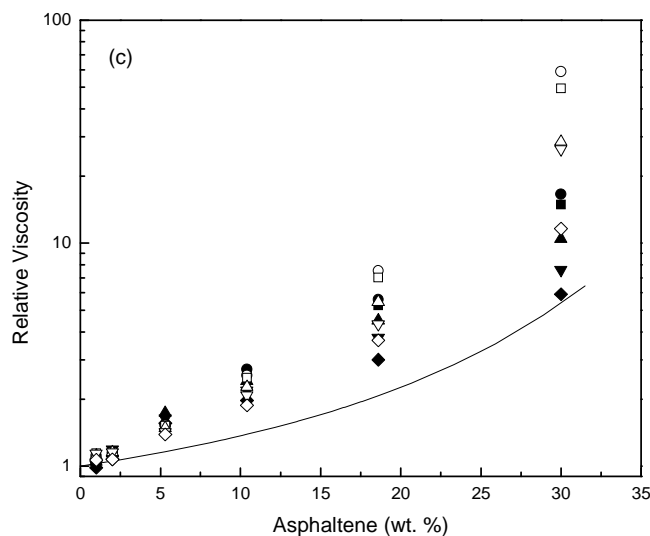
Figure 8.9. Relative viscosity of Maya and Athabasca asphaltenes in a) toluene, b) tetrahydrofuran, c) 1 methyl naphthalene. Temperature is a parameter. Maya asphaltenes: ○, 298 K; □, 303 K; △, 323 K; ▽, 348 K, ◇, 373 K. Athabasca asphaltenes: ●, 298 K; ■, 303 K; ▲, 323 K; ▼, 348 K, ◆, 373 K. Solid curve, equation 8.1 with parameters describing the behavior of nanofiltered samples[35].

From the forgoing, it is clear that the exaggerated composition and temperature dependence for relative viscosity exhibited by the reconstituted samples and reflected in Figure 8.8 can be attributed to measurement artifacts. Consequently, relative viscosity data for reconstituted crude samples cannot be interpreted meaningfully from the perspective of asphaltene structure or variation of asphaltene structure with temperature or asphaltene-oil interaction and must be
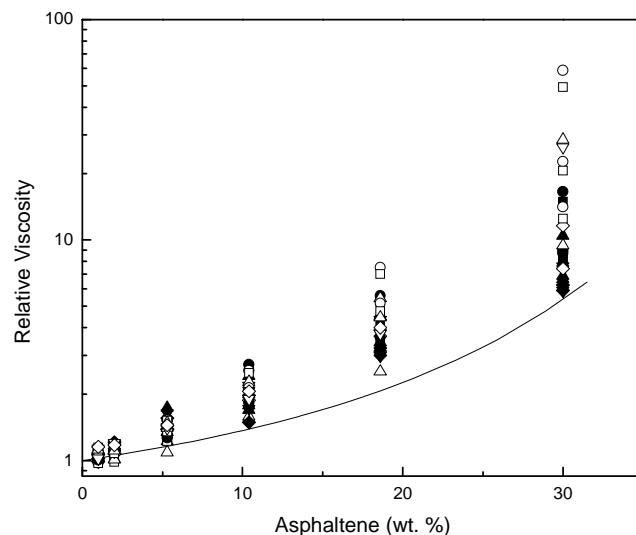
Figure 8.10. A summary of the relative viscosity of Maya and Athabasca asphaltene in pure hydrocarbon liquids. Maya asphaltenes: ○, 298 K; □, 303 K; △, 323 K; ▽, 348 K, ◇, 373 K; Athabasca asphaltenes ●, 298 K; ■, 303 K; ▲, 323 K; ▼, 348 K, ◆, 373 K. Solid curve, equation 8.1 with parameters describing the behavior of nanofiltered samples[35].

discounted in these contexts. The result remains a meaningful one though because it provides indirect support for preferential sorption of species from a liquid by chemically separated asphaltenes – a subject for further detailed study.

8.4.6. What can be inferred from the rheology data vis-à-vis asphaltene structure?

The rheology data for the pure hydrocarbon liquid + asphaltene mixtures, and reconstituted and cross-reconstituted mixtures concur that chemically separated asphaltenes have a greater impact on dispersion viscosity than physically separated asphaltenes and their structures irrespective of nature must therefore differ. Further, chemically separated Maya asphaltenes have a significantly greater impact on relative viscosity than the corresponding Athabasca asphaltenes at the same mass % - Figure 8.10. With reference to Figure 8.1, any of the phenomena shifting the impact of dispersed phase behavior to the left may be occurring, or the precipitated asphaltenes may simply be more porous than the physically separated ones. To account for the differential impact of Maya vs. Athabasca asphaltenes, the Maya asphaltenes merely need to be more porous, or be shifted further to the left by phenomena noted in Figure 8.1 than the Athabasca asphaltenes. While non-particulate interpretations of the behavior of asphaltenes in hydrocarbon liquids from pure diluents to maltenes remain tenable, the elimination of temperature dependent artifacts in the relative viscosity data for chemically separated asphaltene + diluent mixtures lends support for the particulate perspective, especially if diluent sorption varies with temperature, as one would expect if simple sorption isotherms are applicable. Known changes in the phase state of asphaltenes with temperature[36, 60] may also affect their hydrodynamic properties as temperature is varied. Thus interpretation of relative viscosity data remains ambiguous.

8.5. Conclusions

Rheological investigations of crude oils and of reconstituted crude oil samples in particular must account for the impacts of solid maltenes, impacts of residual solvent redistribution when maltenes and asphaltenes are remixed, as well as impacts of asphaltenes themselves in modeling and analysis of results to avoid misattribution of observed phenomena. The large temperature and composition dependence exhibited by reconstituted crudes comprising chemically separated maltenes and asphaltenes, normally attributed to asphaltene properties, would appear to be one such artifact. Indirect evidence reported here suggests that this commonly observed rheological behavior arises primarily from a redistribution of some of the residual pentane initially present in the chemically separated maltene to the asphaltenes, and only secondarily from chemically separated asphaltene properties themselves. However, asphaltene behavior in re-constituted samples does differ from that observed in nanofiltered samples and the properties of Maya and Athabasca asphaltenes in reconstituted samples differ from one another. These differences diminish as temperature increases. The physics and chemistry of these differences are not resolved in the present work and remain subjects for ongoing investigation.

216

References

(1) Mazza, A. G. *Modelling of the liquid-phase thermal cracking kinetics of Athabasca bitumen and its major chemical fractions*. Ph.D. Thesis, University of Toronto, Toronto, Canada, 1987.

(2) Asprino Brinez, O. J. *Fluid properties of asphaltenes at 310--530°C*. M.Sc. Thesis, University of Alberta, Edmonton, Canada, 2005.

(3) Rahmani, S. *Kinetics and phase behavior in asphaltene cracking*. Ph.D. Thesis, University of Alberta, Edmonton, Canada, 2002.

(4) Branco, V. A. M.; Mansoori, G. A.; De Almeida Xavier, L. C.; Park, S. J.; Manafi, H. *J. Pet. Sci. Eng.* **2001,** 32, (2-4), 217-230.

(5) Murgich, J.; Strausz, O. P. *Pet. Sci. Technol.* **2001,** 19, (1-2), 231-243.

(6) Yarranton, H. W. *J. Dispersion Sci. Technol.* **2005,** 26, (1), 5-8.

(7) Andreatta, G.; Bostrom, N.; Mullins, O. C. *Langmuir* **2005,** 21, (7), 2728-2736.

(8) Mostowfi, F.; Indo, K.; Mullins, O. C.; McFarlane, R. *Energy Fuels***2008,** 23, (3), 1194-1200.

(9) Priyanto, S.; Mansoori, G. A.; Suwono, A. *Chem. Eng. Sci.* **2001,** 56, (24), 6933-6939.

(10) Taylor, R. S.; Stemler, P. S.; Lemieux, A.; Fyten, G. C.; Cheng, A. In *Proceedings of the 7th Canadian International Petroleum Conference*, Calgary, Alberta, Canada, 2006; Paper 053.

(11) Licha, P. M.; Herrera, L. *Soc. pet. Eng. J.* **1975,** Paper 5304.

(12) Escobedo, J.; Mansoori, G. A. *SPE Prod. Facil.* **1997**, (May), 116-122.

(13) Holder, G. D.; Enick, R. M.; Mohamed, R. S. *Fluid Phase Equil.* **1996,** 117, 126-137.

(14) Sharma, M. M.; Yen, T. F.; Chilligarian, G. V.; Donaldson, E. C. In *Some Chemical and Physical Problems in Enhanced Oil Recovery Operations*, Development in Petroleum Science, New York, 1985; Chilligarian, G. V.; Yen, T. F., Eds. Elsevier: New York, 1985; pp 223-249.

(15) Licha, M. P. *Oil Sands* **1977**, 609-624.

(16) Jacobs, I. C.; Thorne, M. A. *SPE Paper No. 14823* **1986**.

(17) Sheu, E. Y. *Energy Fuels* **2002,** 16, (1), 74-82.

(18) Sheu, E. Y.; De Tar, M. M.; Storm, D. A. *Fuel* **1991,** 70, (10), 1151-1156.

(19) Takeshige, W. *J. Colloid Interface Sci.* **2001,** 234, (2), 261-268.

(20) Barre, L.; Simon, S.; Palermo, T. *Langmuir* **2008,** 24, (8), 3709-3717.

(21) Sirota, E. B. *Energy Fuels***2005,** 19, (4), 1290-1296.

(22) Zhao, B.; Becerra, M.; Shaw, J. M. *Energy Fuels***2009,** 23, (9), 4431-4437.

(23) Baltus, R. E. Characterization of Asphaltenes and Heavy Oils Using Hydrodynamic Property Measurements. In *Structures and Dynamics of Asphaltenes*, Mullins, O. C.; Sheu, E. Y., Eds. Plenum Press: New york and London, 1998; pp 303-335.

(24) Mack, C. *J. Phys. Chem.* **1932,** 36, 2901.

(25) Lorenz, P. B.; Bolen, R. J.; Dunning, H. J.; Eldib, I. A. *J. Colloid. Sci.* **1961,** 16, 493.

(26) Reerink, H. *Ind. Eng. Chem. Prod. Res. Develop.* **1973,** 12, 82

(27) Storm, D. A.; Baressi, R. J.; Sheu, E. Y. *Energy Fuels* **1995,** 9, (1), 168-176.

(28) Sheu, E. Y.; Shields, M. B.; Storm, D. A. *Fuel* **1994,** 73, (11), 1766-1771.

(29) Storm, D. A.; Sheu, E. Y. *Fuel* **1993,** 72, (2), 233-237.

(30) Storm, D. A.; Barresi, R. J.; DeCanio, S. J. *Fuel* **1991,** 70, (6), 779-782.

(31) Storm, D. A.; Sheu, E. Y.; DeTar, M. M.; Barresi, R. J. *Energy Fuels***1994,** 8, (3), 567-569.

(32) Mullins, O. C. *Spe J.* **2008,** 13, (1), 48-57.

(33) Marques, J. *Hydrocraquage Catalitique Des Asphaltenes Pour L'Hudrotraitement De Residus En Lit Fixe*. Ph.D. Thesis, Universite de Poitiers, Lyon, France, 2008.

(34) Bazyleva, A.; Hasan, M. A.; Fulem, M.; John, M. S. *Journal of Chemical Engineering Data* **2010,** 55, (1), 354–357.

(35) Hasan, M. A.; Fulem, M.; Bazyleva, A.; Shaw, J. M. *Energy Fuels***2009,** 23, 5012-5021.

(36) Fulem, M.; Becerra, M.; Hasan, M. A.; Zhao, B.; Shaw, J. M. *Fluid Phase Equilib.* **2008,** 272, (1-2), 32-41.

(37) Hiemenz, P. C.; Rajagopalan, R. *Principles of Colloid and Sufrace Chemistry*. Third Edition ed.; Marcel Dekker Inc.: New York, 1997.

(38) Cosgrove, T. *Colloid Science, Principles, Methods and Applications*. Blackwell Publishing LTD.: Oxford, UK, 2005.

(39) Batchelor, G. K. *J. Fluid Mech.* **1970,** 41, (3), 21.

(40) Batchelor, G. K. *J. Fluid Mech.* **1977,** 83, ((Nov)), 21.

(41) Batchelor, G. K.; Green, J. T. *J. Fluid Mech.* **1972,** 56, (3), 401-427.

(42) Vand, V. *Journal of Physical and Colloid Chemistry* **1948,** 52, (2), 277-299.

(43) Eilers, H. *Kolloid-Zeitschrift* **1941,** 97, (3), 313-321.

(44) Krieger, I. M. *Adv. Colloid Interface Sci.* **1972,** 3, (2), 111-136.

(45) Krieger, I. M.; Dougherty, T. *Trans. Soc. Rheol.* **1959,** 3, 137-152.

(46) Roscoe, R. *British Journal of Applied Physics* **1952,** 3, (AUG), 267-269.

(47) Roscoe, R. *J. Fluid Mech.* **1967,** 28, 273-&.

(48) Chong, J. S.; Christia.Eb; Baer, A. D. *J. Appl. Polym. Sci.* **1971,** 15, (8), 2007-&.

(49) Parkinson, C.; Matsumoto, S.; Sherman, P. *J. Colloid Interface Sci.* **1970,** 33, (1), 150-160.

(50) Wierenga, A. M.; Philipse, A. P. *J. Colloid Interface Sci.* **1996,** 180, (2), 360-370.

(51) Yamamoto, S.; Matsuoka, T. *Computational Materials Science* **1999,** 14, (1-4), 169-176.

(52) Sudduth, R. D. *J. Appl. Polym. Sci.* **1993,** 48, (1), 25-36.

(53) Pal, R.; Rhodes, E. *J. Rheol.* **1989,** 33, (7), 1021-1045.

(54) Storm, D. A.; Sheu, E. Y. Colloidal Nature of Petroleum Asphaltenes. In *Asphaltenes and Asphalts, 1*, Yen, T. F.; Chilligarian, G. V., Eds. Elsevier: Amsterdam, 1994; Vol. 1, pp 125-158.

(55) Wargadalam, V. J.; Norinaga, K.; Iino, M. *Energy Fuels***2001,** 15, (5), 1123-1128.

(56) Luo, P.; Gu, y. *Fuel* **2007,** 86, (7-8), 1069-1078.

(57) Sirota, E. B.; Lin, M. Y. *Energy Fuels***2007,** 21, (5), 2809-2815.

(58) Zhao, B.; Shaw, J. M. *Energy Fuels***2007,** 21, (5), 2795-2804.

(59) Marques, J.; Guillaume, D.; Merdrignac, I.; Espinat, D.; Barré, L.; Brunet, S. *Oil & Gas Science and Technology - Rev. IFP,* **2009,** 64, (6), 795-806.

(60) Bagheri, S. R.; Gray, M. R.; McCaffrey, W. C.; Shaw, J. M. In *11th International Conference on Petroleum Phase Behavior and Fouling,* Jersey City, USA, 2010, Paper 07

Chapter 9: Conclusions and Recommendations

This chapter presents a summary of conclusions based on the results and conclusions described in Chapters 4 to 8. Some general recommendations for further study in the two fields, bioaerosol formation and breakup, and asphaltene nanoaggregates in bitumen and heavy oil, are noted following each topic.

9.1. Conclusions: Bioaerosol droplets generation and control during coughing

Effect of viscoelastic and surface properties of artificial mucus simulant gels on the size distribution and volume concentration of bioaerosol droplets generated during coughing were investigated. The purpose was to identify, from an engineering point of view, if there is a range of viscoelastic and surface properties of human airway mucus, where the number or volume concentration of droplets generated during coughing is minimal. An additional goal was to find whether the size distribution of the droplets generated during coughing can be altered by modulating the viscoelastic and surface properties of mucus. The key conclusions from this work are:

1.   Variation of surface tension in the range 30 to 55 dyne/cm did not show any change in the droplet size distribution and/or volume concentration of droplets generated during coughing.

2.   Complete suppression of droplet formation and controlling the size of droplets generated during coughing are both practically achievable through careful modulation of the mucus viscoelastic properties.

3.   Results showed an increase in particle size as the samples changed from an   elastic solid type to a viscoelastic type to viscous fluid type sample.

4.   Volume concentration of droplets i.e. the number of droplets generated during coughing diminishes to zero in a certain range of complex viscosity and   phase angle values.

The results have, thus, shown a clear target for the properties of airway mucus to be modulated for reducing the airborne bioaerosol emission and for controlling their size distribution.

9.2. Recommendations for future studies on bioaerosol droplets

Future studies in the area of bioaerosol droplets generation during coughing should include the following considerations.

1.   Understanding the mechanisms and the fluid Mechanics of droplet formation and breakup in lungs and respiratory airways will be helpful for achieving the goal of mitigation of contagious bioaerosol droplet formation and emission during coughing. Experimental studies of the

instability of the perturbed mucus surface and the droplets formation using high speed imaging can, therefore, be a natural progression for the current project and a potential future project for investigation.

2. Given that the current *in vitro* study has shown a clear target for the properties of airway mucus to be modulated for reducing the airborne bioaerosol emission and for controlling their size distribution, the study now should focus on i*n vivo* investigation and analysis, at first, in animal models and then to human subjects.

3. In the current work the fluidity of the mucus sample (viscoelastic properties) and the characteristic time scale of the rheological experiments have been treated separately. As the fluidity of the mucus is dependent on the characteristic timescale of the rheological measurement, it would be helpful in future studies to combine the two parameters and express the viscoelastic properties in terms of a dimensionless number, Deborah number (defined as $De = t_c/t_p$, where t_c refers to the stress relaxation time and t_p refers to the time scale of observation). Proper understanding of the effect of Deborah number on the size distribution and amount of bioaerosol droplet generated during coughing will help in controlling the mucus properties of healthy and diseased persons more accurately.

9.3. Conclusions: Structure of Asphaltene nanoaggregates in Bitumen and heavy oils

Study of viscoelastic behavior of Athabasca bitumen (Alberta) and Maya crude (Mexico) oil samples, along with their Nano-filtered samples obtained using membranes of pore diameters 5, 10, 20, 50, 100 and 200 nm, and mixtures of chemically separated asphaltenes and maltene at different concentrations was conducted. The objective was to characterize some of the physical properties of asphaltene nanoaggregates in bitumen and heavy oil using their rheological behavior. The key conclusions from this work are:

1. Composition and/or phase behavior of maltenes play a crucial role in determining bitumen and heavy oil viscosity. The three orders of magnitude difference in the rheological data of bitumen and conventional crude oil are explained, which suggests new approaches for how viscosity can be reduced. It is shown that at high solids/dispersed phase loadings even small reductions in the dispersed phase volume fraction have significant impacts on viscosity.

2. Nanofiltered Maya crude and Athabasca bitumen exhibit rheological behaviors consistent with slurries comprising a Newtonian liquid + non-interacting hard spheres in the temperature range 298 K to 373 K, if all solids present are accounted for.

3. While the Sudduth equation fits very well with the nanofiltered samples' data, the same is not true for the reconstituted samples.

4.   Structure of asphaltenes in mixtures of chemically separated asphaltenes and maltenes is significantly different from those in natural hydrocarbon resources.

5.   Maya heavy oil and Athabasca bitumen are shear thinning fluids over temperature ranges of industrial interest for production, storage, and transport. Complex viscosity must be associated with a specified shear condition in order for reported viscosity values to have meaning. Up to three orders of magnitude variation in reported viscosity values for Athabasca bitumen can be attributed to the impact of shear as an uncontrolled variable in viscosity measurements. At elevated temperatures, bitumen and heavy oil approach Newtonian rheological behavior. Sample origin, production method and post-production treatments can also account for up to three orders of magnitude variation in measured viscosity values. By contrast, thermal and shearing history plays a secondary role. Variations, if present, fall within one order of magnitude, however, the effect of thixotropy for such complex fluids should be taken into consideration. A clear understanding of the variables affecting the rheological properties of bitumen and heavy oil is of crucial importance for selecting or optimizing flow regimes for their production and transport. Results reported here are expected to reduce the technical uncertainty related to the design and development of heavy oil and

bitumen production and transport processes and to allow practitioners to discriminate real from phantom variables present in their own measurements and in the literature.

6. Hydrocarbon resources such as Athabasca bitumen and Maya crude oil possess complex phase behaviors and present equally complex rheological properties. The impact of non-asphaltenic solids, on the complex viscosity of hydrocarbon resource samples at specific temperatures and on trends with temperature, is underscored in this contribution. Solid maltenes are shown to play a crucial role in determining the rheological properties of bitumen and heavy oil. Permeates, retentates and feeds associated with nanofiltered Maya crude oil and Athabasca bitumen exhibit rheological behaviors consistent with slurries comprising a Newtonian liquid + non-interacting hard spheres in the temperature range 298 K to 373 K, when the role of solid maltenes is included. Failure to account for solid maltenes in the interpretation of rheological data for these hydrocarbon resources leads to misattributions related to the nature and the importance of the role that asphaltenes play in the determination of hydrocarbon resource viscosity.

9.4. Recommendations for continuation of studies on Asphaltene aggregates

Based on the results and conclusions presented above, the future studies in the area may include the following considerations.

1. Thermal relaxation and creep behavior: study of the thermal relaxation and creep behavior of bitumen and heavy oils at different temperatures may provide further useful information about molecular conformation of asphaltene nanoaggregates in native and non-native solvents.

2. Asphaltenes precipitation and drop out from Bitumen-Heavy oils: The tendency of the asphaltenes to form aggregates is believed to be responsible for numerous problems during bitumen recovery, transportation, and processing, such as formation damage and well plugging, reactor and line coking, refinery tower plugging, and catalyst deactivation. Future study in this area should focus on (i) a complete characterization of the precipitation behavior of asphaltene particles in bitumen and crude oil and (ii) prevention of asphaltenes' precipitation and drop out during production, transportation and refining of petroleum fluids.

3. Fine particle separation through physical separation techniques: To study the fine particles removal through physical separation from bitumen and heavy oil.

9.5. Concluding Remarks

The objective of this thesis was to exploit the interrelations between the rheological behavior and nano-microstructure of complex fluids in understanding how the amount and characteristics of bioaerosol droplets generated during coughing can be controlled, and in characterizing the nano-microstructure of asphaltene particles in bitumen and heavy oils. The methodical approach taken here not only provided answers to the questions under investigation, but it also led to new discoveries, such as why some people produce more bioaerosol droplets than others during coughing, and how suppressing the emission of bioaerosol droplets during coughing by controlling viscoelastic properties of the mucus can be achieved. This dissertation thus presents the rheology as a promising tool that can be useful in determining the nano-micro scale structure and behaviors of various complex non-Newtonian fluids.
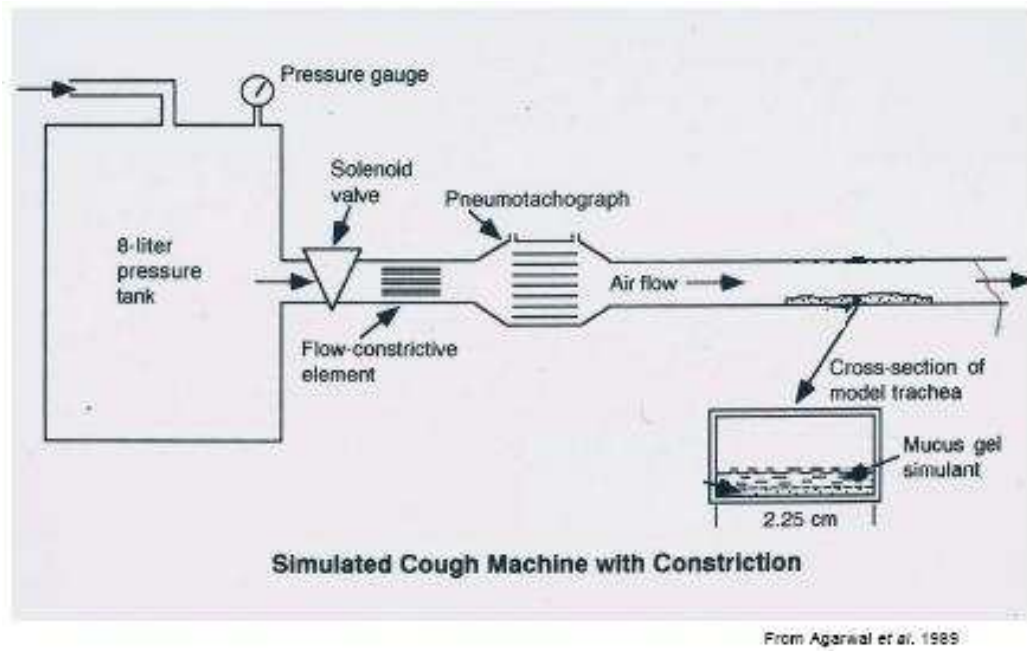
Appendix A

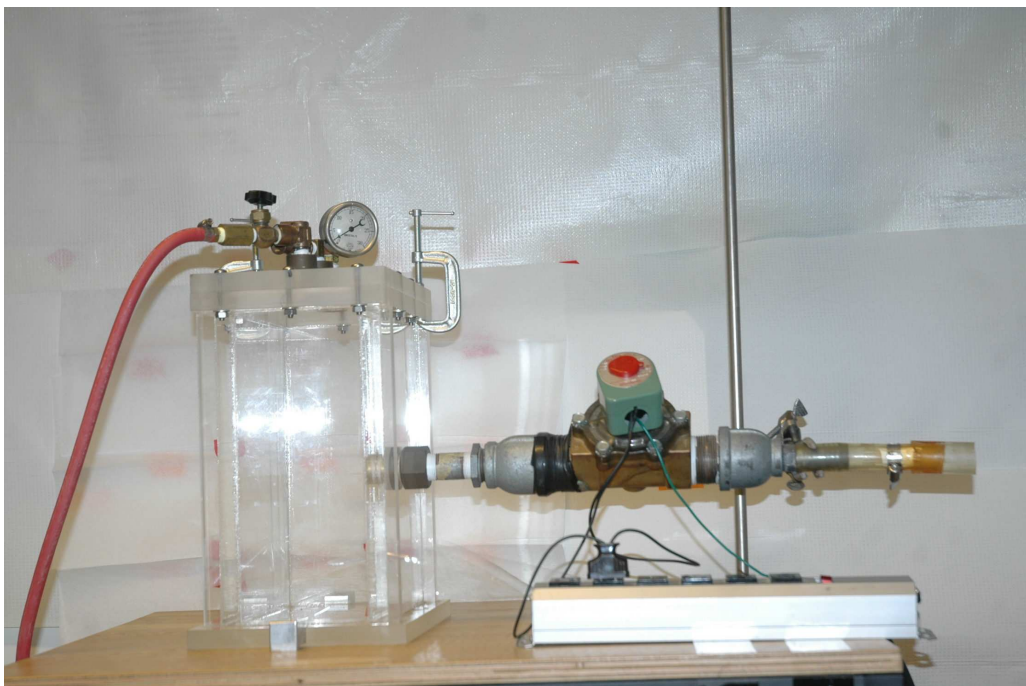Fig. A.1. Schematic diagram of the cough machine experimental set up.

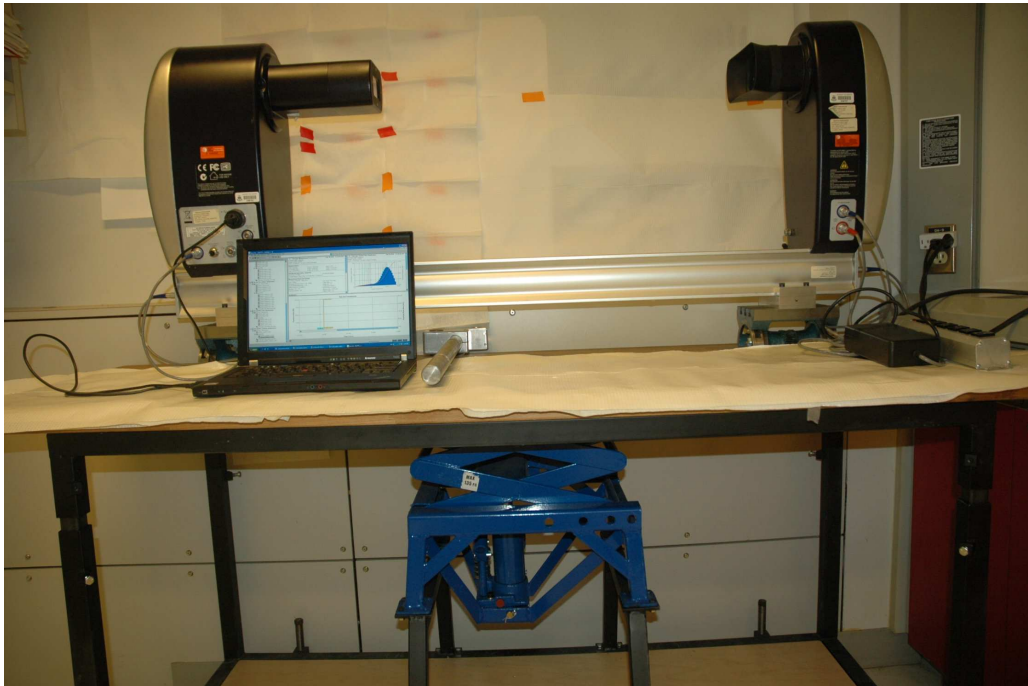Fig. A.2. Cough machine experimental set up.

Fig. A.3. Digital Photograph of the Spratec laser diffraction device used for

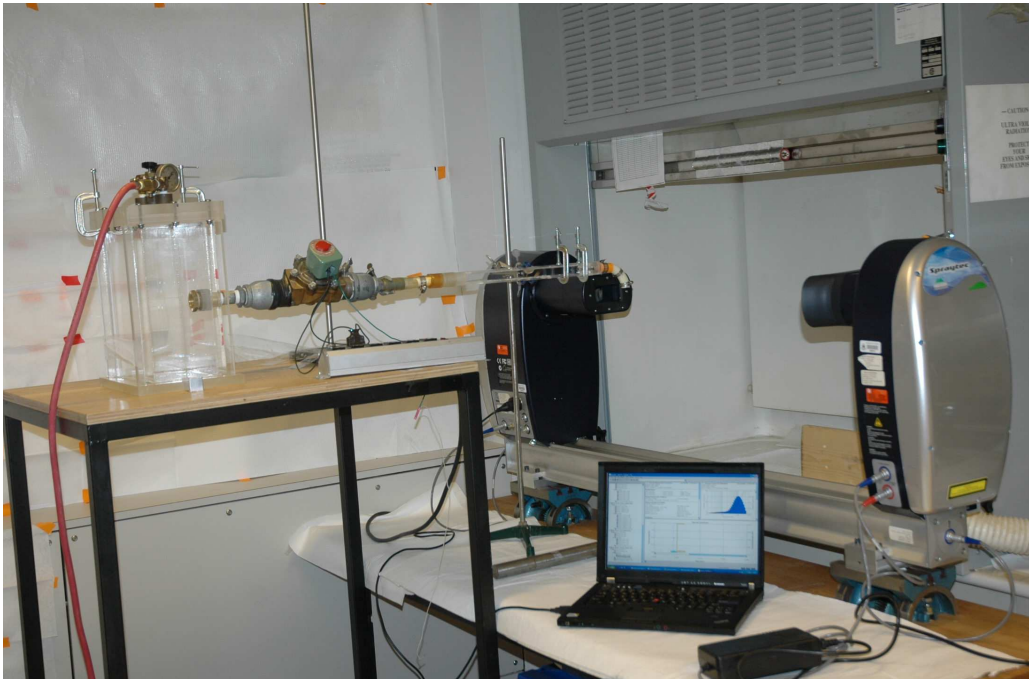measurement of droplet size distribution.

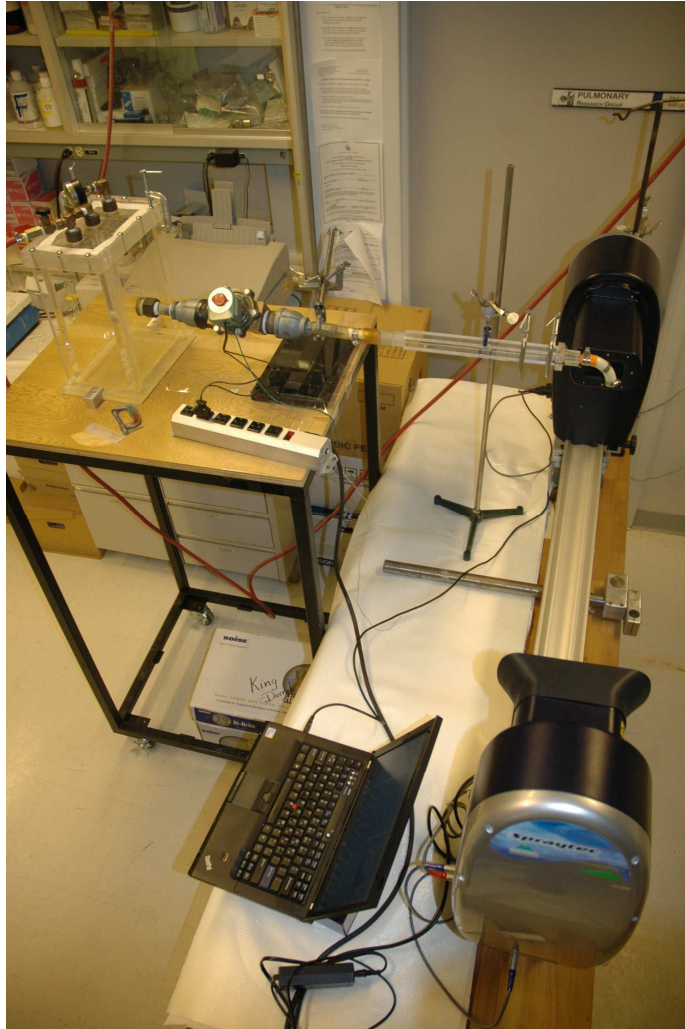Fig. A.4. Complete experimental set up: cough machine with Spraytec device.

Fig. A.5. Isometric view of the cough machine set up with Spraytec device.

Fig. A.6. Experimental set up for measurement of rheological properties.

Fig. A.7. Experimental set up with peltier plate assembly for rheological
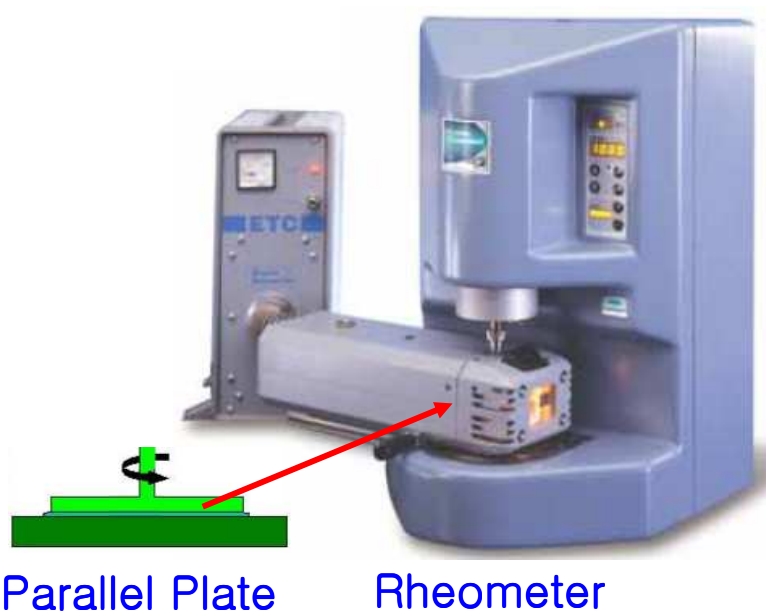
measurements.

Parallel Plate   Rheometer

Fig. A.8. Bohlin Gemini HR 200 nano rheometer with ETC (extended

temperature control) for rheological measurements (Source: www.malvern.com).

Appendix B. Artificial Mucus Simulant

The artificial mucus simulant samples in this thesis were prepared using Locust Bean Gum (LBG) solution cross linked with sodium tetraborate solution. The LBG powder is a yellowish powder obtained from the endosperm of the seeds of carob tree. Therefore sometimes it is also termed as carob gum. The structure of LBG is reported to consist of a galactomennan chain having a long backbone of mannos with galactose side branches. **Borax**, also known as **sodium borate**, **sodium tetraborate**, or **disodium tetraborate**, is usually a white powder consisting of soft colorless crystals that dissolve easily in water. When a borax-water solution is mixed with LBG solution, a viscoelastic material is formed which is the result of cross-linking in polymer.
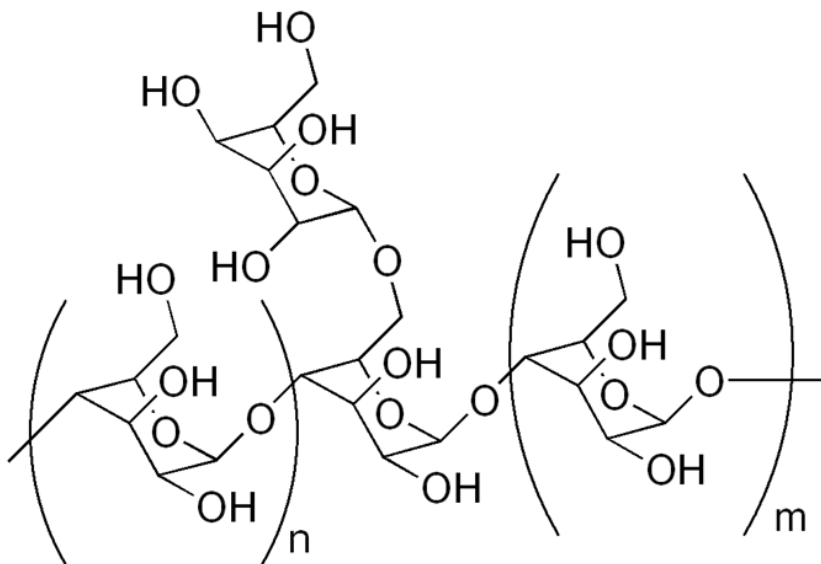

Fig. B.1 Molecular structure of galactomannan showing mannose backbone and a galactose side chain (source: wikipedia)